PASSIVE IMPACT DAMAGE DETECTION OF FIBER GLASS COMPOSITE PANELS.

By

BRUNO ZAMORANO-SENDEROS

A dissertation submitted to the Graduate Faculty in Mechanical Engineering in Partial fulfillment
of the requirements for the degree of Doctor of Philosophy.
The City College of New York
2013

Report Documentation Page

1. REPORT DATE **19 DEC 2014**	2. REPORT TYPE **Masters Thesis**	3. DATES COVERED **04-11-2012 to 10-12-2013**

4. TITLE AND SUBTITLE **PASSIVE IMPACT DAMAGE DETECTION OF FIBER GLASS COMPOSITE PANELS**	5a. CONTRACT NUMBER
	5b. GRANT NUMBER
	5c. PROGRAM ELEMENT NUMBER
6. AUTHOR(S) **BRUNO ZAMORANO-SENDEROS**	5d. PROJECT NUMBER
	5e. TASK NUMBER
	5f. WORK UNIT NUMBER

7. PERFORMING ORGANIZATION NAME(S) AND ADDRESS(ES) **The City College of New York,160 Convent Avenue,New York City,NY,10031**	8. PERFORMING ORGANIZATION REPORT NUMBER **; #24378**

9. SPONSORING/MONITORING AGENCY NAME(S) AND ADDRESS(ES) **U.S. Army TARDEC, 6501 East Eleven Mile Rd, Warren, Mi, 48397-5000**	10. SPONSOR/MONITOR'S ACRONYM(S) **TARDEC**
	11. SPONSOR/MONITOR'S REPORT NUMBER(S) **#24378**

12. DISTRIBUTION/AVAILABILITY STATEMENT
Approved for public release; distribution unlimited

13. SUPPLEMENTARY NOTES
A dissertation submitted to the Graduate Faculty in Mechanical Engineering in Partial fulfillment of the requirements for the degree of Doctor of Philosophy. The City College of New York

14. ABSTRACT
Several novel passive methods for detecting high speed impact damage in composite panels will be presented. These methods analyze the signal from the impact induced structural wave arriving at a network of piezoelectric sensors to estimate the position of the impact and to determine the extent of damage caused by the impact. We will first present the manufacturing technique used to embed an array of brittle piezoelectric ceramic sensors into custom built epoxy-fiberglass [0o/90o] composite panels. We will then compare both classical triangulation techniques and a newly developed technique using arrays of sensors to determine the position of high speed impacts within these panels. The last part of the thesis will focus on a novel technique for estimating the extent of damage within the composite under impacts at various speeds.

15. SUBJECT TERMS

16. SECURITY CLASSIFICATION OF:			17. LIMITATION OF ABSTRACT	18. NUMBER OF PAGES	19a. NAME OF RESPONSIBLE PERSON
a. REPORT **unclassified**	b. ABSTRACT **unclassified**	c. THIS PAGE **unclassified**	**Public Release**	**139**	

UNCLASSIFIED

This manuscript has been read and accepted for the graduate Faculty in Engineering in satisfaction of the dissertation requirement for the degree of Doctor of Philosophy.

12/19/13
Date.

Professor Niell Elvin
Chair of Examination Committee.

12/19/13
Date.

Dean Ardie Walser.
Executive Officer

Examination Committee:
Professor Yiannis Andreopoulos. The City College of New York, Dept. of Mechanical Engineering.
Professor Feridun Delale. The City College of New York, , Dept. of Mechanical Engineering.
Professor Nikhil Gupta. Polytechnic Institute of new York University
Professor Benjamin Liaw. The City College of New York, Dept. of Mechanical Engineering.

THE CITY COLLEGE OF NEW YORK

Abstract

By

Bruno Zamorano-Senderos

Advisor: Professor Niell Elvin

Co-Advisor: Professor Benjamin Liaw

Several novel passive methods for detecting high speed impact damage in composite panels will be presented. These methods analyze the signal from the impact induced structural wave arriving at a network of piezoelectric sensors to estimate the position of the impact and to determine the extent of damage caused by the impact. We will first present the manufacturing technique used to embed an array of brittle piezoelectric ceramic sensors into custom built epoxy-fiberglass [$0^o/90^o$] composite panels. We will then compare both classical triangulation techniques and a newly developed technique using arrays of sensors to determine the position of high speed impacts within these panels. The last part of the thesis will focus on a novel technique for estimating the extent of damage within the composite under impacts at various speeds.

Dedication

I dedicate this work to my family.

Acknowledgements

I would like to extend my appreciation to my advisor Niell Elvin, Ph.D. His dedicated guidance and intelligence kept me moving in the right direction and has made this work possible. I would also like to thank my co-advisor Ben Liaw Ph.D., without him I would still be struggling to understand waves. A special thanks to members of the committee, Feridun Delale Ph.D. and Yiannis Andreopoulos Ph.D. Their ever present guidance and support has been very useful and appreciated. Finally, I would like to thank Dr Gupta for accepting to be part of the committee and revising this work. I would like to acknowledge the US Army-TARDEC group for providing the funding for the work; Jerry Chung Ph.D., who supported my work at Frontier Performance Polymers. Finally, my heartiest appreciation for Dr. Delale in supporting my working in a difficult economic environment.

Table of contents

List of tables

List of Figures

List of Equations

List of abbreviations

1D – one dimension

2D – two dimensions

A0 – anti symmetric lamb wave of order 0

CT – conventional triangulation algorithm

DAQ – data acquisition card

DP – damage parameter

FEM – finite elements methods

GAD – group angle detection method

NDE – non-destructive evaluation

P – principale (or pressure) wave

POP – peel of ply

PVDF – polyvinylidene fluoride

PZT – Lead zirconate titanate

RTM – resin transfer molding

S – secondary (or shear) wave

S0 – symmetric lamb wave of order zero

SHM – structural health monitoring

SP – signal parameter

TOA – time of arrival

V50 – 50% chances of penetration projectile velocity

VARTM – vacuum assisted resin transfer molding

VI – vacuum infusion

List of variables

α simplified exponential part of absorption

$\alpha(\theta, \omega)$ complete exponential absorption coefficient.

$a_v(t)$ analytic function of $V(t)$

$C(\theta)$ speed of the sound on direction θ

C_p speed of the principal wave

C_s speed of the secondary wave

c speed of sound in wave equation

ΔTOA difference of time of arrival

δ_{ik} Dirac's delta.

D stiffness tensor

D_{ijkl} stiffness tensor component.

$\widetilde{D}_{ijkl}$ complex stiffness tensor for hysteresis absorption model

D'_{ijkl} imaginary part of complex stiffness tensor

D_{ij} stiffness tensor in two index notation on directions i j

d_i distance from impact to sensor i

E Young modulus

E_A absorbed energy

E_i Young modulus on direction i

E_{nv} envelope of function $V(t)$

$f(\theta)$ arbitrary angular absorption function

G_{23} shear modulus on directing 2,3

$\mathcal{H}$ Hilbert transform

$h_v(t)$ V function's Hilbert transform

$J_n(r)$ Bessel function on r

k data number k of $V(t)$

UNCLASSIFIED

k_0 data corresponting a t_0 on *V(t)*

k_1 data correspondint to t_1 on *V(t)*

m projectile mass

$\hat{n}$ unitary vector on the wave propagation direction

n_l component of unitary vector on direction l

$\Phi(\phi)$ arbitrary function of the angle ϕ for separation of variables

ϕ_k arbitrary wave function on direction k

ϕ angle from z axis to the position direction

ζ absortion

ν Poisson ratio

ν_{ij} Poisson ratio on direction i with a strain on direction j

ρ density

θ angle from fibers direction

θ_{12} angle of the line between sensor 1 and 2 to the fiber direction.

θ_f angle between the front of the wave and direction of propagation

$R(r)$ function that depends only on r for separation of variables

r radial distance

rate adquisitoni sampling rate of signal *V(t)*

σ_{ij} component of stress direction i,j

S_{ij} compliance tensor in two index notation on direction i j

T tension

$T(t)$ arbitrary function of time *t*

t time

t_0 initial time for the SP calculation

t_1 final time for the SP calculation

T_0 time of impact

TOA_i, time of arrival to sensor i

u generic displacement

u_k displacement on direction k

$V(t)$ measured voltage signal

v_0 inital projectile speed

v_R residual speed after impact of projectile

$\vec{x}$ position vector

x, y impact position

$x_i \; y_i$ position of sensor i

$Z(z)$ arbitrary function of z.

z coordinate in z direction.

1 Objectives and accomplishments

The objective of this work was the development of high speed impact resistance intelligent panels and the measurement techniques to:

- Provide good impact resistance

- incorporate integrated sensors

- Provide means to locate the impact location

  o With simplified cable routing

  o With less computational cost

- Calculate the extent of the damage

  o With simplified cable routing

  o With less computational cost

In the course of this research it will be proved that all these objectives have been successfully accomplished. Furthermore, the following secondary accomplishments are also noted:

- The development of a technique to measure the speed of the sound in composite material

- An approximate formulation for the damping/dispersion of the wave on composite panels

- An experimental technique to measure the damping /dispersion in composite panels

- An optical method to measure the extent of damage in translucent composite materials

2   Introduction

The industrial and commercial use of composite materials has been steadily growing over the past decades; some industries that have experienced significant growth include the defense, civil, aerospace and sport-equipment sectors.   Using the aerospace sector as an example of the acceptance of composite materials, the ratio of composite materials to total weight has risen from 25% for the A380 and AV8 (introduced in 1985), to approximately 33% in the F22 (introduced in 2005); the A350 (planned for 2014) is expected to consist of more than 50% composite materials.   In the automotive sector, the desire of developing greener cars has led to the need for weight reduction and therefore the increased use of composite materials. The U.S. government has stated that the cost of fuel in the battlefield is a substantial burden; energy absorbing composite materials can potentially be lighter than steel or aluminum for the same threat level and therefore can reduce fuel requirements.

Composite materials have a number of potential advantages over conventional materials since they can be designed to increase performance in a number of applications including: specific stiffness, specific strength, and immunity to corrosion. The use of composite material becomes especially attractive to sectors where weight reduction has a significant impact on the overall performance of the structure.

The use of composite material however presents some disadvantages. Loads during service as well as environmental effects can introduce damage in the composite component. Tensile or compressive failure (overload), impact, fatigue, creep, and chemical material degradation, are some of the mechanisms that can produce damage in the material (Zhao, Gao and Zhang, 2007). Composite materials have complex failure modes at multiple scales including: fiber breakage or matrix cracking, delamination, interface debonding, fatigue failure, and fiber kinking (Saponara,

Horsley and Lestari, 2011). One of the major disadvantages of composite materials remains that they tend to have reinforcement within the plane of the lamina and thus are weak in their thickness direction. This coupled with the inherent anisotropy of each layer means that damage in these materials tends to occur between the layers (so called delamination). By definition, delamination damage occurs below the surface of the material and in general cannot be detected using traditional visual inspection techniques. These delaminations can then grow due to fatigue under service loads causing early component failure.

One of the more common causes of delamination in composite structures is due to impact. These impacts can create very high localized stresses (especially shear and transverse stresses) in the material and can be caused by a number of different sources with a wide range of velocities. For example, dropping a tool onto a composite structure can be considered to be a low velocity impact with low associated energy. Speeds for low velocity impacts are typically between 5 and 15m/s (with 1 to 10J of energy). Intermediate speed impacts can be produced during hail damage or collision with birds in flight. Higher speed impact examples include high speed impacts where speed is in the range of 300-900 m/s and energies in the 100-5000J range depending on the projectile's initial speed and mass. Hyper-speed impacts typically occur in space structures such as when space debris collides with an orbiting satellite; these velocities can be as high as 10,000m/s.

As previously mentioned, subsurface delamination damage often remains hidden to visual inspection requiring non-destructive evaluation (NDE) methods to assess the location and severity of the damage. These NDE methods range from X-ray techniques to ultrasonic inspection. All NDE methods have a major drawback in that the composite components require periodic inspection which not only include placing the parts out of service but also require highly

qualified personnel to perform the inspection. The inspection process adds significant operating expenses that make the use of composite materials less attractive. One major challenge in NDE is to reliably assess the structural health of a component without taking it out of service. Real time structural health monitoring (SHM) can answer this challenge by reducing the number of inspections and providing useful in-service information on the remaining life of the component. Ideally the SHM system will be able to provide the following information: (1) location of the damage, (2) extent of the damage, (3) type of damage, and (4) the remaining life of the structure.

In the list above, each step significantly increases the complexity of the SHM system. For example, locating the position of damage alone is significantly simpler than assessing the extent of damage, while estimating remaining life of a component remains a research challenge even for the simplest types of damage. Increasing complexity in the SHM system typically increases both the number of required sensors, and the overall electrical energy expenditure and computation requirements for the sensor network. Thus it is not always technically viable in all applications to assess all SHM parameters for a given structure. For real-time monitoring it is thus important to identify the in-service critical parameters that need to be measured by the system which might only include basic damage assessment.

In any SHM method, the first step is to determine the position of the damage. This step alone might alert the user for the need of more detailed inspection and the associated possible component substitution, and in some cases might enhance critical in-service operational awareness such as the fact that a high velocity impact has occurred. Furthermore it is generally impossible to determine the remaining structural life of a component without knowledge of the damage location. Thus knowing this basic information (i.e. that a possibly damaging event has occurred), and the location of the damage, can reduce the number of periodic inspections (i.e.

only to times when they are actually needed), and as a direct consequence also increase the overall safety of the structure.

Once the location of the damage is known, the next step of the SHM system is to evaluate the extent of the damage. It is clear that a small delamination in a particular location in a structure will have a smaller effect on the safety of the structure than a larger delamination. The evaluation of the extent of damage will typically require more sophisticated analysis than the previous location detection step, and will typically require information about the damage position. It may also require more sensors increasing the overall complexity of the system. Provided the extent of the damage is known, the SHM system can then move onto estimating the safety of the structure/component and to further facilitate in-service decision making.

It is well known that manufacturing using multilayer composite materials is significantly more expensive than using traditional materials such as steel. Thus one of the key challenges faced in the manufacturing of multifunctional panels that are able to provide SHM, is to control the overall manufacturing cost. At the same time, electrical cable routing through a structure (needed to transmit data or power) is a challenging issue due to the high associated cost, which is mainly due to the fact that these cables are manually routed (Van der Velden 2007). The use of multifunctional self-sensing panels with their associated sensors will further exacerbate this problem. Typically any damage detection technique will require a distributed network of sensors throughout the entire structure. More sensors generally improves the accuracy of any damage detection technique while at the same time making the routing and integration of the sensors into the structure, more difficult and expensive.

One last consideration when manufacturing multifunctional materials is the energy consumptions associated with the calculations required to obtain useable data (such as damage location and position) from the measurements. Overall energy consumption of the system should be maintained to a minimum and the algorithms developed for damage detection should be simple enough to be implemented; ideally in small low-power integrated circuits. For example, military personnel might carry up to 20% of their total load in battery power[1]. Is clear that in this application, reduction of computational energy cost, is a requirement for any new system that is introduced in an already energetically burdened environment.

This dissertation will covers the following topics in the development of a novel multifunctional system for high speed impact damage detection:

- A novel sensor embedding technique which

    o improves the survivability of sensors

    o provides sensor integration

    o minimizing cable routing and integration cost

- A novel damage location calculation offering

    o simpler cable routing

    o reduced computational cost

- Presents an algorithm to calculate the extent of the damage from high speed, impacts,using a newly developed damage parameter. This system:

    o uses the same sensor network as for the impact location measurement

    o is relatively easy implementation on an integrated circuit

---

[1] http://www.army.mil/article/53283/

3 State of the art

This chapter covers some of the previous research done in multifunctional composite materials with a specific focus on manufacturing of panels with embedded sensors, impact damage location and SHM in composite materials. Though the present research focuses on passive damage detection, most of the advances in damage detection in composite materials have been in the field of active (i.e. ultrasonic) methods. Some of these active methods are directly applicable to the present research and thus have been covered in this overview chapter.

3.1 Multifunctional panel manufacturing

Almost by definition any multifunctional SHM structure needs and integrated sensing and associated electronics to process the associated data.

Integrated sensing for composite materials has been studied by a number of authors and the techniques range from piezoelectric "reinforcement" (Tressler, 1999) to fiber reinforced composite with integrated discrete piezoelectric sensors (Coleman, 1998). The selection of appropriate materials and associated sensing techniques is closely coupled with manufacturing methods for these multifunctional structures. A more detailed literature overview relevant to the manufacturing of these panels will be more fully described in the introduction of the next chapter.

3.2 Damage location detection

Location detection using wave propagation (either electromagnetic or acoustic) is a well-established technique. The techniques can be either active (as used by RADAR) or passive (as used in SONAR). This thesis focuses on passive impact location detection. In the context of this work, passive detection means that the structural waves generated by the impact themselves are

used to find its location. A key challenge that arises in passive wave propagation in composite materials is that these materials tend to be anisotropic and highly attenuating. This in turn means that the wave front is complex (i.e. not circular as in isotropic materials), wave speeds are different in different orientations within the material, waves are dispersive (i.e. waves with different frequencies travel at different speeds) and that waves can travel different distances before being fully attenuated again dependent on the direction of propagation.

The most commonly used method for impact location is triangulation based on the impact generated wave (Coverley and Staszewski, 2003; Schäfer and Janovsky, 2007; Dehghan Niri and Salomone, 2012; De Marchi et al., 2011; Saponara, Horsley and Lestari, 2011). Advances on this known calculation has been made, like the technique developed by Staszewski (2002) and Coverley and Staszewski (2003), consisting of conventional triangulation together with a genetic algorithm to locate the damage position. In their paper, a network of sensors covering the surface of the structure was used; a signal envelope was employed to determine the time of arrival of the impact wave. Genetic algorithms have been proposed as well for impact force detection (Yan and Zhou, 2009). A network of sensors and triangulation was also used by LeClerc et al. (2007) and successfully applied to predict the impact location in a complex composite structure (i.e. an aircraft component). Acoustic emission sensors with a triangulation technique applied to aluminum honeycomb panels were used to detect impact locations for impacts in the hypervelocity range (Schäfer and Janovsky, 2007). Dehghan Niri and Salamone (2012) used a triangulation technique with a probabilistic method for impact discrimination together with a wavelet time of flight measurement, this is an interesting advance since uses particular frequencies through the wavelets arrival time. De Marchi et al. (2011) used a triangulation detection technique to detect Lamb waves with surface mounted piezoelectric sensors; the waves

were generated by the impact of a pencil with a thin aluminum panel. This research took into account the distortion of the Lamb-waves propagating through the panel. Lamb waves are always dispersive due to the difference between wave and phase speed (or in other words different speed with frequency). Note that this wave distortion is more important in anisotropic composite materials. Piezoelectric sensors combined with a triangulation technique were also used by Saponara, Horsley and Lestari (2011) in a composite material similar to the one employed on this work. Other techniques have also been explored like time reversal techniques using a single sensor and the wave reflection history to reconstruct the impact position (Ciampa and Meo, 2011). Though of great interest, Ciampa and Meo's (2011) work required a large number of tests to train the neural network; such training could be impractical to perform for impacts in the high speed range.

All previously mentioned triangulation techniques used a network of sensors that are placed so that the impact location is within the area circumscribed by the sensors (except for Ciampa and Meo, (2011) where a single sensor and a time reversal technique was utilized). Another technique for impact detection used the angle between two known sensor positions and the impact locations to calculate the position of the impact. This technique was used by Betz et al. (2007) where fiber optical Bragg grating sensors where employed, and by Lanza si Scalea et al. (2011) and Salomone et al. (2010) where piezoelectric fiber composite sensors were employed. The impact angle technique developed in those papers used an array of three sensors (i.e. a rosette) to measure the relative amplitudes of the impact wave at the same location from which angle to the impact could then be determined. The inherent directionality of the response of the sensors is used, since the sensors measurement depends of the angle of the strain to the sensors, the angle can be calculated by comparison between sensors in different directions, but close by.

Since they are close the response can only depend on the angle so comparison is possible. Two rosette groups were then used to calculate the intersection of the lines formed by the impact direction and thus the impact position could be calculated. Since the relative amplitude and shape of the impact signal is used for this calculation, this technique does not rely on measuring the time of arrival of the impact and are thus fundamentally different to the triangulation techniques. These orientation based techniques are the foundation for the new technique proposed in this work, which uses a time of arrival calculation similar to the classical triangulation technique to obtain the impact location.

Another method proposed by Ciampa, Meo and Barbieri (2012) used pairs of acoustic emission sensors to locate impacts that are close to perpendicular to the line between the sensor pairs. A number of the sensor pairs can then be used to estimate the impact location, with the advantage that no speed of sound knowledge is required. Kundu, Nakatani and Takeda (2012) employed a group of three acoustic emission sensors to calculate the angle of the impact location in a similar way to the present research, for each 3 sensors they are able to obtain angle information. Since the distance from the impact to the sensors was large compared with the distance between sensors, Kundu, Nakatani and Takeda (2012), used a constant speed of sound approximation. The more general case in which the speed of sound is assumed to be angle dependent (as would be the case in anisotropic materials when the distance between the sensors cannot be assumed to be small compared to the distance to the impact location) is investigated in the present research. Another difference is that one single angle is created for each pair of sensors this allow to obtain more redundant information, or reduce number of sensors and therefore with less cable routing.

3.3 Damage extents

After the position of damage has been detected, generally any SHM method will then be concerned in determining the extent of this damage. The most common approach in determining the extent of damage is to use active detection. A number of different ultrasonic active techniques have been studies in the past. Most of these techniques use so called guided Lamb waves which can propagate long distances within thin structures such as plates and thus are ideal for interrogating large areas of structures. The passive method proposed in this research also relies on Lamb waves that are generated during the impact. Other waves will generally be absorbed quickly and thus will be assumed not to reach the location of the sensors. The underlying assumption in the present research is that the impact location is far away to ensure that only guided Lamb waves are measured at the position of the sensors.

Lamb waves have been some characteristics that make them attractive for damage detection. They have two modes (symmetric and anti-symmetric) as shown in Figure 3.1. These two modes can allow for the detection of both surface defects and sub-surface defects Su (2006) . Changes of thickness of the plate (as caused by surface damage) change the propagation speed for a given frequency and can be considered to act as a boundary/discontinuity in the material. Both a reflected and refracted wave will be generated at this damage zone, therefore allowing detection. Lamb waves typically travel long distances in the material with little loss of energy, a range between 3000mm to 85mm in composite panels from the source has been previously reported (Su, Ye, & Lu, 2006). Propagation distances estimates in composite materials vary depending on the particular study and material but a conservative estimate of 100mm (Zhao, Gao, & Zhang, (2007)) can be used for sensor design purposes. Birt, (2000) also studied the propagation of Lamb waves showing attenuation over a distance of 150 to 600mm for the S0

propagation mode. This work also compared the performance of three piezoelectric types: PVDF, PZT and a 0-3 composite PZT transducers. The conclusion of this comparison was that PVDF is approximately and order of magnitude less sensitive than of PZT, and that the 0-3 composite PZT transducer is about twice as sensitive as the PVDF transducer but with an angle dependence on the measurement. For the present work, due to the impact geometry, the generated waves are expected to be anti-symmetric dominant. These waves are typically absorbed at a faster rate and thus the use of the more sensitive piezoceramic material appears to be justified. Measured attenuation in previous research are generally measured using relatively low power ultrasonic sources; high speed impact energies tend to be significantly greater so even longer propagation distances are expected for this case.
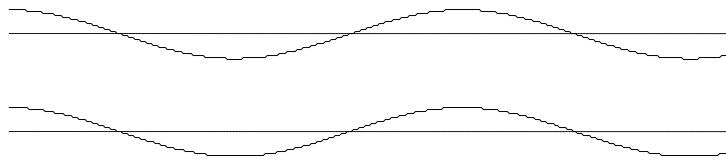
Anti symmetric wave.
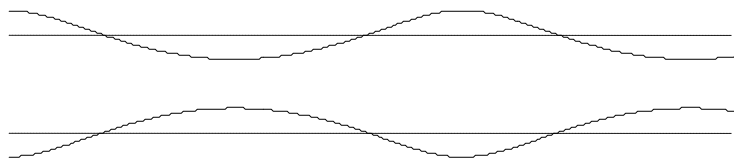
Symmetric wave.

Figure 3.1 Representation of Ansti symmetric and symmetric waves.

UNCLASSIFIED

Many methods have been used in the past to generate Lamb waves including: ultrasonic probes, lasers, piezoelectric elements, or interdigitated transducers (Su, Ye, & Lu, 2006). Piezoceramic materials are sensitive, have adequate frequency response and generally require no external power source so are well suited for Lamb-wave damage detection and have been used in a number of previous studies ((Birt, Badcock, & A, 2000) (Moulin, Assaad, Delebarre, Kaczmarek, & Balageas, 1997) (Moulin, Assaad, Delebarre, Kaczmarek, & Balageas, 1997)).

Work related to the absorption of Lamb waves is of importance in SHM and a number of studies have addressed this issue. One example is the research of Torres-Arredondo (2011) where different models of absorptions were proposed and wave absorptions curves were then calculated.

Maznev (2003) worked on a theoretical solution to the problem of surface wave propagation form a point source. The main result of from that work that is pertinent to the present research is that in the far field approximation, the integrals that are associated with the calculation of the wave are weighted with a factor of $1/\sqrt{r}$. This $1/\sqrt{r}$ approximation will be used in the present work to correct the signal arriving from the impact source.

As previously mentioned, high speed impacts have velocities comparable to the speed of sound in the material and the waves propagating from the impact carry high stresses away from the impact point to the rest of the structure. During the last decades a significant effort has been made in the scientific community to developed analytical models to understand the mechanics underlying high speed impact. Taylor (1942) develops a model for a single fiber subjected to high speed impact in a direction perpendicular to its length. Roylance (1973) generalizes this model to transverse impact using the Finite Element Method (FEM) and Morrinson (1984) and

Prevorsek (1991) studied different types of yarns and their behavior under high speed impacts. Roylance (1980) showed that a lightweight material with a high elastic modulus, (i.e. high wave speeds), distributes tension better thereby reducing the dynamic stresses and allowing more energy absorption.

The extension of modeling efforts from 1D to 2D was first done by Vinson and Zukas (1975), and a multilayer soft armor model was developed by Parga-Landa and Hernandez-Olivares (1995). Energetic models that consider wave propagation and multiple failure mechanisms have been developed by Morye et al. (2000); in this work the development of an impact cone model is proposed and measured using high speed photography as shown schematically in Figure 3.2. Naik (2004) generalized this model to a multilayer material and shear plugging energy was also introduced to the impact model. Later a similar model was proposed by Mamivand (2010) where the formation of the damage cone was again proposed; this model introduced parameters that took into account the inertial changes in the speed of the projectile due to the deformation of the layers of material.

The importance of those papers for the present work is that they show the initial impact profile is likely to generate waves that are mostly anti-symmetric in nature and also they provide an approximate method of calculating contact forces during impact. In general a good overview of prior work was done by Cheeseman (2003). In general the impact cone is formed by the propagation of the transverse waves. The steeper the slope of the impact cone, the higher the strain levels in the fibers. The results from Morrinson (1984) and Prevorsek (1991) show the effect of stress rate on the properties of the fiber. Stress on the fiber is related to the strain rate at high speeds. On some of the fibers under high speed impacts, it appears that the faster the shot the higher the stress on the fiber for a same cone height. Though those papers focus on

determining V50 of the projectile, an interesting result for this research is that if the projectile is stopped, the cone base continues propagating and therefore the maximum stress on the fibers will be before the projectile has completely stopped. This result will be used to estimate the upper limit of the contact force that is needed to develop the novel damage parameter developed in this thesis.
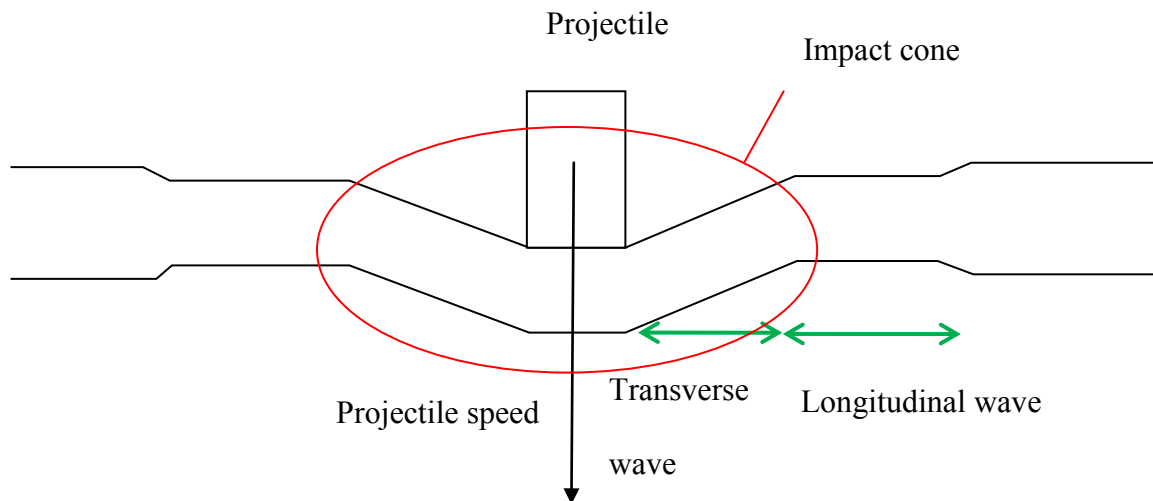
Figure 3.2 Cone formation on a composite material due to the high speed impact. Note that the poison contraction due to the longitudinal wave as been exaggerated.

The contact force during impact is closely related to the generated waves; thus knowledge of the contact force history can provide a very useful insight into the nature of the waves that can be expected to arrive at the sensor location. Though beyond the scope of this thesis, using the methods of Maznev (2003) it would be possible to calculate an approximate wave propagation profile; (the propagation profile is approximate since the damage in the material caused by the impacts will change the nature of the wave itself). It should be noted that there are a number of

research articles published for the case of low speed impact. However low speed impacts are different from high speed impacts in the sense that the later are wave dominated while the former can be considered quasi-static or boundary dominated. Even considering that high and low speed impacts are different, some of the work carried out in this field on low velocity impacts are relevant to the present work since they show that contact force pattern can change with material damage. Chang and Sun (1989) used a Green function approach and signal deconvolution to predict the impact force using remotely located sensors. Chandrashekhara (1997) uses a FEM trained neural network to calculate the contact force for low speed impacts, the contact forces were presumed to be Hertzian in nature. Yang and Sun (1981) have shown that due to permanent deformations during indentation, the Hertzian contact law is not adequate for carbon fiber reinforced composites and as a consequence of this permanent indentation, the unloading path is different that the loading path. Props et al. (2010) used fiber Bragg grating sensors to detect low impact damage characteristics. That work used a full spectral interrogation method to show important details that would be hidden using single frequency interrogation and thus showing the importance of the contributions the different frequency on the impact event. In the case of low speed impact, knowing the impact force history is equivalent to knowing the impact energy, and therefore all information about the damage, assuming a complete characterization of the material has been carried out. Unfortunately direct measurements of contact forces in high speed events are not possible at this moment. Future advances on micro-instrumented projectiles could change this in the near future (Sandia labs self guided bullet)[2].

Some attempts have been made to measure the contact force in composite materials under high speed impacts. Starratt et al. (2000) measured the force displacement curves for high speed tests

---

[2] https://share.sandia.gov/news/resources/news_releases/bullet/#.Uo6Z98Ssh8F

on Kevlar 129 fabric and found that when penetration of the projectile occurs, the maximum force occurs before the maximum displacement of the fabric is reached. However when the projectile does not penetrate the fabric, the maximum force occurs at the same time as the maximum displacement. For both cases however, the total contact duration is reached at approximately at the same displacement. Contact forces in that research was measured in an indirect way by measuring the acceleration of the projectile (and assuming no deformation). The results of this paper are in fair agreement with the prediction made using energetic impact models.

To the best of our knowledge no published research exists on the use of passive techniques to detect the amplitude of the damage for high speed impact.

4   Multifunctional Panel manufacturing

4.1   Introduction

As the name indicates, multifunctional materials are materials that are able to perform more than one function at the same time; for example, materials with sensing capabilities while maintaining their structural properties.   In this study a multifunctional material has been developed that provides high speed protection while measuring both damage position and extent. To provide this functionality, the sensors have to be seamlessly integrated within the structure in order to be able to measure the required damage parameters.

Embedding sensors within a host composite panel has its own set of unique challenges. The performance of the sensing device, including sensitivity and longevity, will depend on how well the sensor is attached to the host material. As previously stated, a high speed impact is an event where the projectile speed is on the order of the speed of the sound and therefore being able to measure the structural wave propagation through the material is of critical importance. Accordingly, the acoustic impedance coupling will be a key factor in determining the sensitivity of the system to the impact process.   As a consequence, both the manufacture of the structural host and sensors, and damage detection techniques are strongly coupled.   Manufacturing of the host panel with embedded sensors is thus a critical part of the proposed work for this thesis.

Manufacturing and sensor integration have the following challenges (Lin & Chang, 2002):

(1) Providing adequate electrical insulation to the sensors.

(2) Reduced structural integrity of the host structure; integrated sensors can introduce stress concentrations or defects.

(3) Consistency and repeatability between different sensors.

(4) Modification of structural properties (e.g. stiffness) of the host structure due to the presence of the sensors.

(5) Added cost of sensor integration.

Previously these challenges have been addressed in a number of different ways, however two main solutions are possible: (a) embedded sensors or (b) surface mounted sensors.

4.2   Advantages and disadvantages of surface mounted and embedded sensors

Surface mounted sensors have three key advantages: (a) since sensors are attached after the manufacturing of the host structure, the sensors can be precisely placed on the structure, (b) the application of the sensor array does not introduce defects in the panel, and (c) sensor integration is less time consuming for prototype manufacturing. Disadvantages of surface mounting include the dependence of the mounting technique and sensor response on the adhesion method, and the survivability of the sensors due to external environmental elements such as impact.

Embedded sensors typically offer a better mechanical coupling with the host material, thereby improving the inherent measurement sensitivity. Embedding the sensors also significantly improves the survivability of the sensors due to the inherent protection provided by the host material. During testing associated with this research, surface mounted sensors have in many cases shattered or delaminated from the structure during the impact of the projectile even when located relatively far from the impact site. This is in stark contrast to the performance of embedded sensors. During similar testing, embedded sensors have been shown to maintain partial to full functionality even when in they are located within the delamination area caused by a high speed impact. Some disadvantages of sensor embedding include: (a) the challenge of

accurate sensor placement (i.e. sensors might move during the manufacturing process), and (b) the man-hours required for manufacturing these panels. The main disadvantage of embedded sensors is that they act as an inclusion within the host materials and can be a source of damage either during manufacturing or under subsequent loading.

Another consideration is the sensitivity of embedded sensor when compared with surface mounted sensors. This relationship between the host and sensor has been previously studied in the case of piezoelectric materials (Soh, Annamdas, & Kiong, 2007); the main conclusion that emerged from these studies is that surface mounting the piezoelectric material performs better if the elastic modulus of the piezoelectric is higher than that of the host structure, the opposite is true for embedded sensors where a stiffer host is preferred (Soh, Annamdas, & Kiong, 2007). The piezoelectric sensor chosen for this research (PZT-5A) has an elastic modulus of 60GPa[3] which has an important influence on the minimum fiber density for the specific composite that is being used. High fiber densities are needed to achieve this relatively high modulus (i.e. 66GPa); for example carbon epoxy pre-peg has a modulus of approximately 66 GPa, while fiber glass pre-peg has an approximate modulus of 22 GPa. Another important reason to chose sensor embedding is that the composite layers prevent the electromechanical fatigue degradation of the PZT (Sung-ChoongWoo & Goo, 2009) .

PZT-5A material was chosen for this study because the piezoelectric and dielectric properties of this material have a good balance between sensing and actuating as compared to other piezoelectric materials with high electromechanical coupling. PZT-5A is a "hard" piezoelectric material with both high piezoelectric and high dielectric constants. This PZT material has a Curie temperature (350ºC), which is above the curing temperature of most thermoset polymers. This

---

[3] http://www.piezo.com/prodmaterialprop.html

allows for the sensor embedded panels to be thermally cured while maintaining the piezoelectric properties of the sensors. The use of PVDF is not recommended because of both its relatively low piezoelectric coupling coefficient and its low Curie temperature (i.e. the thermal curing of the composite materials will depolarize the PVDF and thus essentially eliminating its piezoelectric coupling. Re-poling the PVDF after curing is possible but adds a significant manufacturing overhead to the process) . Note however that PZT-5A is more rigid than the host structure and therefore is not the best selection for embedding within a lower modulus host material (Soh, Annamdas, & Kiong, 2007). The high capacitance of these PZT sensors allows for the use of a less complicated signal conditioner in the sensing stage than if a PVDF material were to be used.

The embedding of sensors has been studied by many authors. The integration of PZT sensors on a fiberglass structure is at the end to integrate a hard ceramic composite host. This was studied by Hansen and Vizzini (1997). They used glass slides on graphite epoxy composite material to simulate the sensors, and studied the effect on the life of the component on tensile and fatigue testing. This study presents a limitation, which is that even though the effect on the host can be addressed, the effect in the sensor cannot. The glass insert on those test though were quite big, covering the entire wide of the specimen (50mm) and with a thickness of 8 plies. On this study a cut off method where the sensor position was free of fiber though cutting was shown to give better tensile properties, but sustained more delamination damage. This case non comparable to our, and showed a significant drop on the properties. Coleman (1998) paper introduced a PZT insert on a composite panel (AS4/3501-6 graphite/epoxy) dimension of the PZT insert were in this case 50.8 X25.4 X0.254 mm. The wide of the specimen in this case in this case was 50.8mm. Sensors where inserted using a cut off method. In this case no significant variation of the

mechanical properties due to the embedding of the sensors was detected, though bigger extent of the damage on fatigue testing was detected. The kapton protected sensors was well integrated into the structure. No effect of fatigue was detected on the PZT output on this paper when strains under the strain limit of the PZT where applied. On high strain rates a sudden drop of voltage was detected..Lin & Chang, (2002). propose another solution, the smart layer, where sensors are integrated in a kapton flexible circuit that can be introduced attached of embedded on the structure The flexible circuit approach allows for an accurate placement of the sensors, a consistent response between sensors and alleviates the difficulty of routing the wiring through the host material by insuring that the wiring is integrated within the sensing layer. These advantages are achieved at the price of introducing an extented defect within the host material. In both cases, initial results showed that these smart composite panels did not suffer a significant change in their failure behavior due to the presence of the PZT, or smart layer. However, later studies showed a reduction in the strength of these composite panels of up to 15%. Thus, there is a significant dependence between the embedding method and the material property behavior (Ghezzo, Huangz, & Nemat-Nasser, 2009). Fabrizia Ghezzo et al. (Ghezzo, Huangz, & Nemat-Nasser, 2009) tested different embedding methods to embed the sensors. They proposed a multi stage process where the fibers are cut, displaced or interlaced (i.e. surround) the sensor. Of these three embedding methods, it was found that cutting the fibers had the most significant effect on the strength of the panel. On the other hand, the fiber interlacing method offered the least strength reduction. Another interesting conclusion of this work is that thin piezoelectric layers do not have a big impact in the mechanical behavior of the host. As a conclusion, for the present research, a thin PZT of small dimension was chosen to be inserted between the fiber glass fabric

in an interlacing pattern, minimizing the impact of the embedded sensors on the strength of the structure.

4.3   Panel manufacturing

Fiber reinforced composite materials are usually built using layers of high strength fibers that are joined together by a matrix material; in the present case a polymeric matrix was used. This matrix serves a number of structural purposes including filling the space between layers of the composite and also provides these materials with interlayer mechanical strength and stiffness. Interaction between fiber and polymer also has a important effect on the general properties of the material. The most general composite manufacturing techniques are:

- Pultrusion
- Resin transfer molding (RTM)
- Vacuum assisted resin transfer molding (VARTM)
- Hand Lay-up
- Autoclaving
- Compression molding
- Vacuum infusion
- Filament winding

Of these methods, both RTM and vacuum infusion have been successfully used for sensor embedding. Vacuum infusion has been used extensively in the fabrication of samples for sensor embedding research (see for example (Ghezzo, Huangz, & Nemat-Nasser, 2009)). This technique is well established and has the advantage of using small pressures and temperatures

compared with autoclaving or RTM, and thus considerably reducing the chances of damaging the sensor in the process.

4.4   Vacuum infusion (VI)

Due to the above mentioned advantages for the ease of use, the VI technique has been selected for the present work. VI has been used for many years to manufacture various composite materials which are widly used for sports equipment, various components of ships and is now being used in the aerospace market. This techniques been applied for small aircrafts and is now been applied to some large aircraft components where RTM has been traditionally used. Vacuum infusion has been successfully used for components with volumes exceeding 10 m^3, which include rotor blades and yacht hulls (20-30m in length). One of the main advantages of VI over RTM is that only one side of the mould is needed for VI since the vacuum bag acts as the opposite side of the mould.

From the point of view of cost, VI is the second cheapest manufacturing method after hand lay-up. As compared to the hand lay-up technique, the resin is contained in the vacuum bag and the process is thus significantly environmentally cleaner and healthier. VI is also generally more reliable than the hand lay-up method and shows good consistency from batch to batch with respect to mechanical properties.

Vacuum infusion does not generate the high pressures that appear in compression molding or in the autoclave technique and thus improve the survivability of the PZT sensors. To obtain a better impact resistant panel, it is known that a high fiber to resin ratio is desirable. Therefore it would be convenient to use a technique that increases this ratio. Vacuum infusion provides in general

low fiber ratios compared with compression molding or autoclaving, but for this research survival of the sensors during the manufacturing process was considered to out-weigh this factor.

Thus VI appears to be a promising, simple method to develop a reliable embedded sensor system and was thus used throughout this research project.

4.5   Vacuum infusion composite panels manufacture with embedded sensors

4.5.1   Panel manufacture

The development of a reliable technique of embedding sensors within its host composite material has been a critical step in the present work and is thus detailed in this chapter of the dissertation. The vacuum infusion process is well known in the composite community but is included in this section for completeness. A list of the materials used in the panel manufacture can be seen on Appendix A.

In order to developed the manufacturing technique some trial and error was carried out with the process. In the course of those attempts, the following issues were detected: Sensors placed on the top surface of the panel tended to break during manufacturing while those placed one fiber layer or more below the surface survived. Thus it was decided to place all the sensors under the first layer of materials. As a consequence, cable routing though the fiber was of critical importance and a robust method of preventing these cables from being damaged while maintaining electrical accesses had to be developed.. Furthermore, the initial position of the PZT sensors could change during manufacturing, either due to the applied vacuum or due to the resin flow. To solve this problem a number of solutions where proposed: (1) stitching the PZT to the composite fiber, (2) gluing the PZT in place and (3) securing the PZT by tying the attached electric cables to the fiber. Stitching was both very labor intensive and failed to provide adequate

restraint to the movement of the sensors during matrix infusion. Tying the electric cables to the fiber provided adequate restraint against sensor movement but lead to failure of some sensors. Of the three methods, gluing the PZT sensors in the desired position was the least labor intensive and appeared to provide adequate constrain against movement; this method was thus adopted for the remainder of the work in this thesis.

The manufacturing of the sensors can be divided in the following steps:

1) Wire preparation. Cable ends are exposed from the insulation
2) Sensor cutting. Sensors are laser cut (or purchased with the desired shape)
3) Sensor wiring
4) Attaching the PZT sensors to the composite fiber
5) Cable routing through the fiber
6) Fiber stack building
7) Vacuum bag assembling
8) Vacuum infusion process
   a. Debagging
9) Test specimens preparation
10) Thermal treatment i.e. curing

Steps 1 and 2 are straight forward and do not require any extra explanation. Circular piezoelectric lead-zirconate-titanate (PZT) sensors are used in this work; the size of the sensors was 6.4mm diameter by 0.191mm thickness (1/4" diameter by 0.0075" thickness). A picture of the sensor can be seen on Figure 3-1.

Sensor wiring. The PZT sensors are coated with sputtered nickel alloy which form the electrodes on both the top and bottom faces of the disk (i.e. the poling direction is through the thickness). . In order to attach the wires to the electrodes, the nickel oxide layer has to be treated

using solder flux (#67 Liquid flux). One of the lead wires is then held next to the cleaned area of the sensor and a small amount of solder is used to connect the wires to the face of the PZT (as shown in Figure 3-4). It was found that directly copying this process to connect the second wire to the other side of the PZT did not work because the heat of the soldering iron would cause the solder of the first wire to re-melt and release the initial lead wire. This problem was solved by holding the first lead wire in place using a pair of self-locking tweezers of which the tips were covered in electrical tape to prevent them from damaging the sensors.   As shown in Figure 4-3 and Figure 4-4. Once the wire leads have been fixed to both sides, the cables are then braided in order to improve survivability in the debagging process and making cable routing easier; the braided cables are shown in Figure 4-5. It is important for the survival of the sensors during the embedding process to control the solder thickness used to attach the wire leads. This is because the fiberglass will be forced to follow the contour of the solder and could perturb the flat interface of the vacuum bag. This can create high stresses in the PZT when pressure is applied from the vacuum bag causing damage in the PZT during the vacuum infusion. In order to ensure that the sign of the voltage output from each sensor is consistent, it is also important to keep track of the piezoelectric polarity of the sensor during the manufacturing process
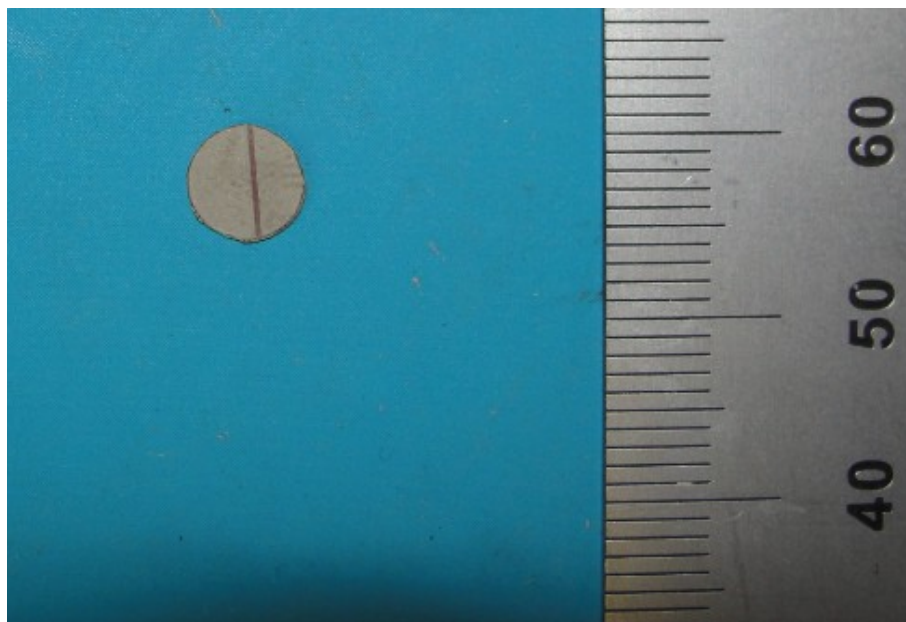
Figure 4-1 PZT sensor used on this work.
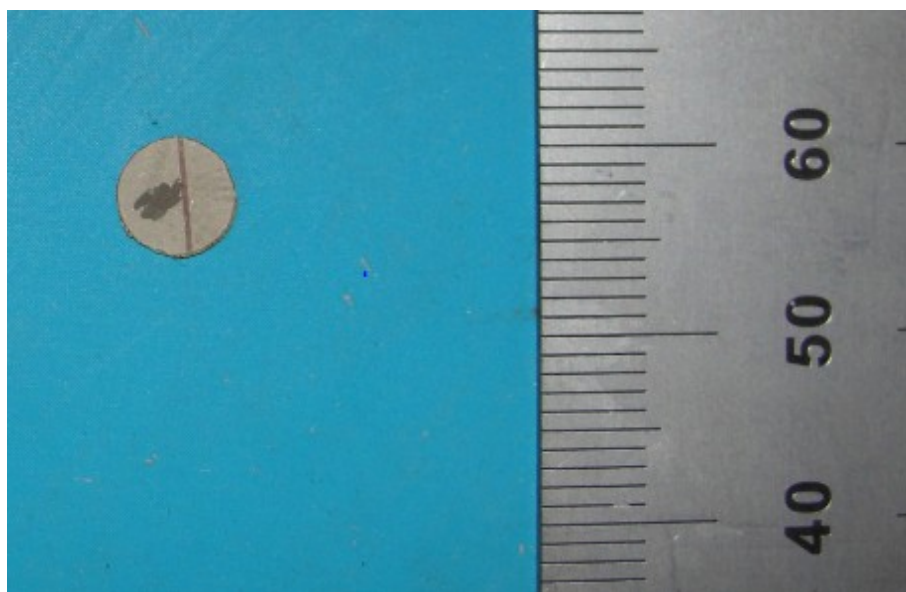
Figure 4-2 PZT sensor with part of the nickel plating removed.

Figure 4-3 Pliers protected with electrical tape are used to hold the PZT sensor.
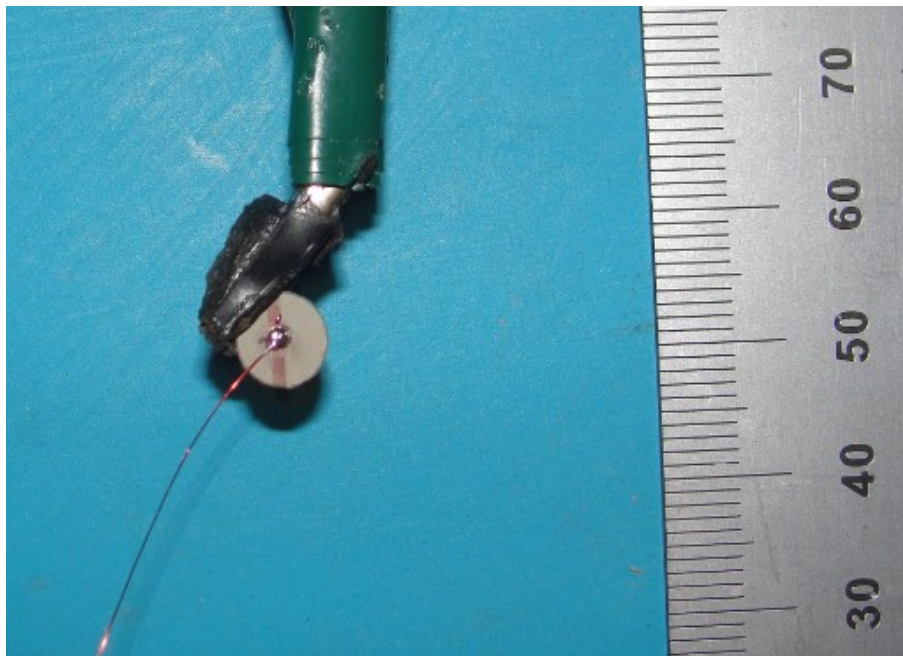
Figure 4-4 A small amount of solder is applied to the sensor to connect the wire leads.

UNCLASSIFIED
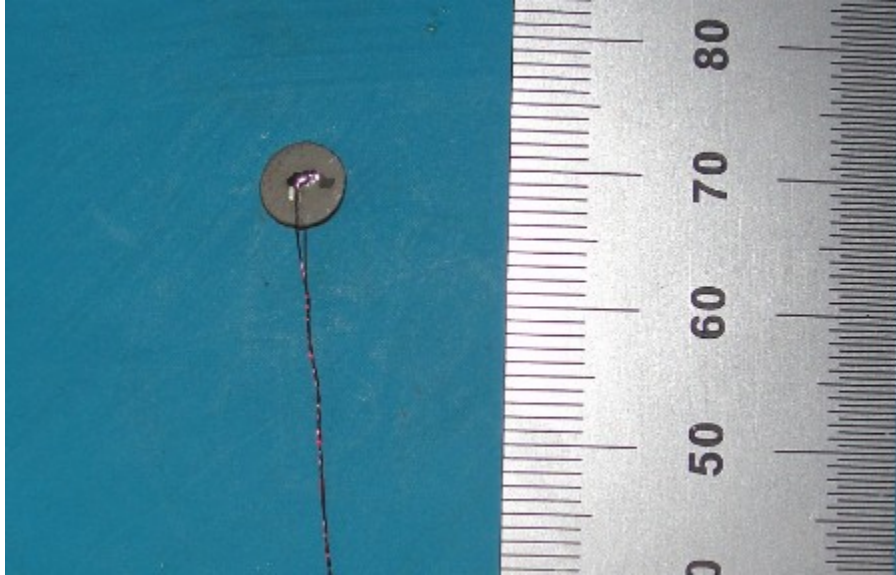
Figure 4-5 A completed PZT sensor with braided wire leads.

Attaching the PZT sensor to the fiber glass mesh. A fast drying epoxy is mixed and placed on the fiber-glass fabric in the desired position. It is recommended to wait until the epoxy has started to cure and is thus more viscous before placing the PZT onto the fiber glass (Figure 4-6). This will ensure that the PZT has minimal movement during the mounting process. Note that cyanoacrylate adhesives are not a good option since they are not compatible with the heat treatment of the panel after manufacture. Figure 4-7 shows the PZT sensor after the epoxy is cured.

Figure 4-6 Placement of the fast-drying epoxy in the desired position for the PZT. It is important to note that the fiberglass will absorb some of the epoxy in this process.
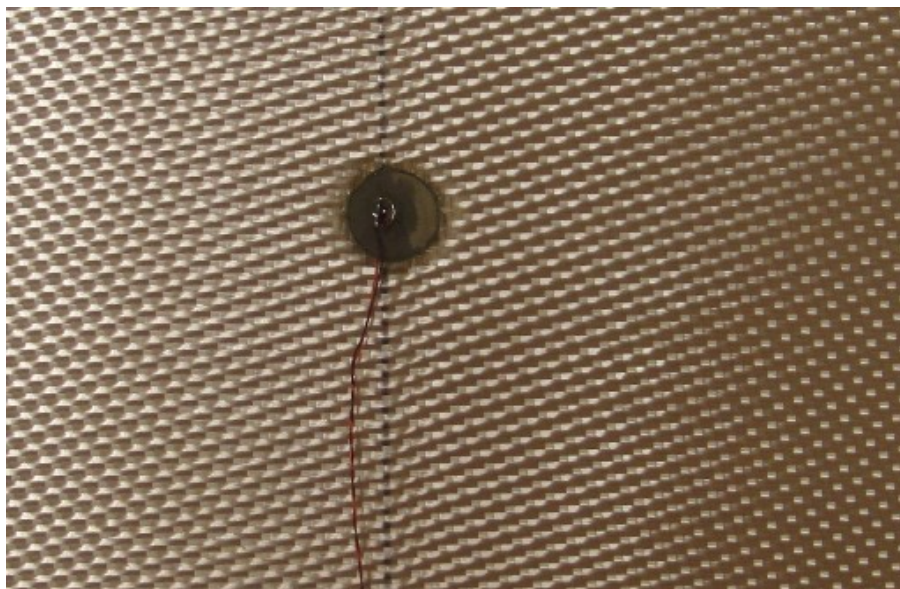
Figure 4-7 Sensor attached to the fiber glass fabric.

Cable routing. As has been mention above, in order to improve the sensors survivability, sensors are placed under the first layer of material. Therefore, to ensure that the sensor leads are

not fully encased in the panel, the electrical leads must be threaded through the fiberglass. This process can be seen in Figure 4-8 and Figure 4-9. To allow for the leads to be threaded, a small hole must first be made in the covering glass fiber layer. The leads are then guided through this hole and oriented in the desired direction. Figure 4-10 shows the sensor and fabric after this process is complete. Note that the distance between sensor and the routing hole is important since it will reduce the tension (so called stress relief) in the cable during the vacuum infusion process
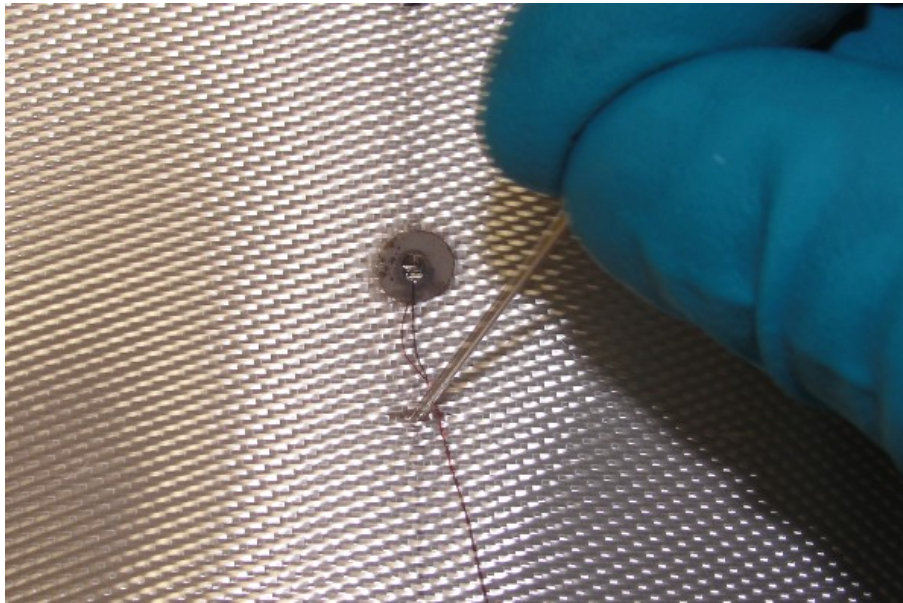
Figure 4-8 Preparation of the hole for the wire leads to be threaded through.

Figure 4-9 Sensor after wire leads are threaded through the glass-fiber layer.
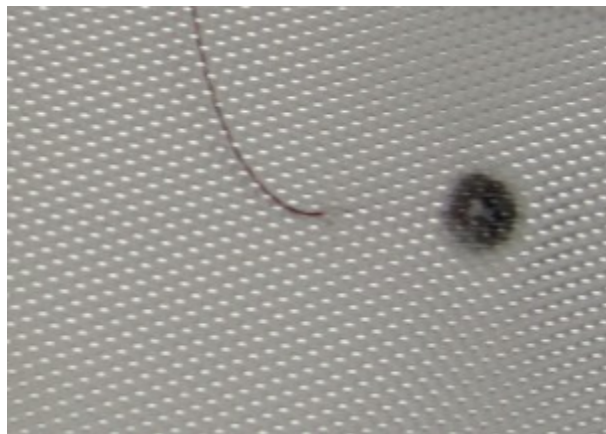
Figure 4-10 View of the sensor leads on the opposing side fiber mesh to which the PZT sensor is attached.

Fiber Stack Assembly. A stack of fiber is then built according to the desired geometric specifications (i.e. fiber orientation, thickness, width and length). In the present study 20 plies of fiber glass (S2-6187 - HEXCEL) with a $[0/90]_{10s}$ stacking was used for all panels.

UNCLASSIFIED

Vacuum bag assembly. Figure 4-11 shows the vacuum infusion setup used for the manufacture of the panel. Two layers of vacuum bag are used, the bottom bag being at a higher vacuum than the top. This bottom bag is used to allow for the base aluminum plate to be easily reused without having to clean off residue epoxy. The fiber-glass layers are then stacked on this bottom bag. The overall stacking of materials is as follows: lower bag, fiber glass, peel of ply, flow media and top bag. When sensors are present, the loose part of the electrical cables should not be in contact with the fiber glass (or they will inadvertently embedded) nor in contact to the flow media (or they will get broken in the debagging process). In those cases, the cable is therefore routed from the fiber through the peel ply; to avoid contact with the flow media, a second layer of peel ply is locally applied to cover the cables. Masking tape has been found to be of great help to hold everything in place during the vacuum infusion process, but direct contact of the tape with the fiber should be avoided.
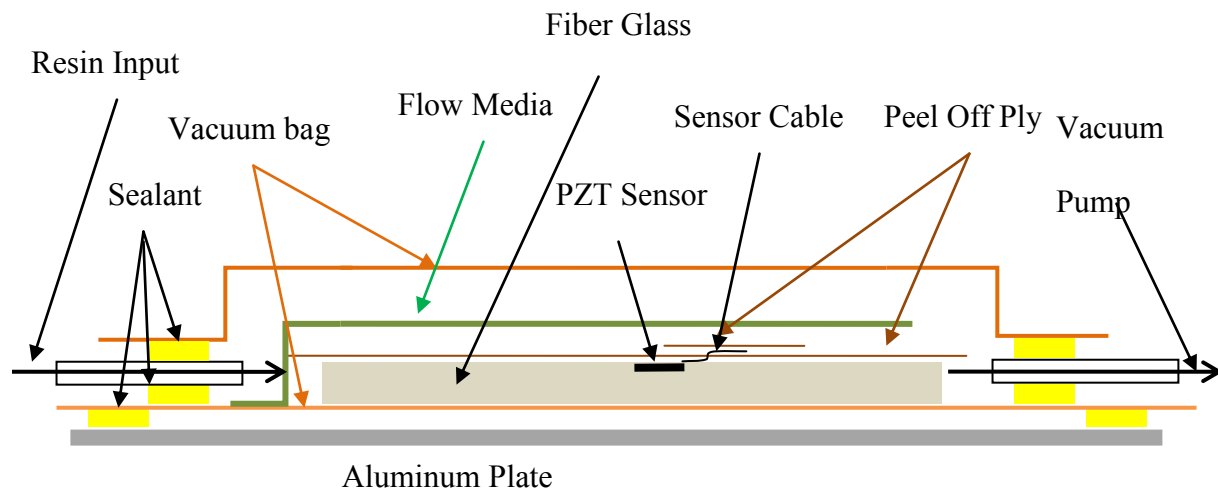
Figure 4-11 Vacuum bagging schematic.

Vacuum Infusion. Once the vacuum level as been checked, the resin/hardener is then placed in a vacuum chamber to remove a majority of the air in the mixture, The tubing on the left of Figure 4-11 is connected to the resin/hardener which will start flowing into the panel when exposed to the vacuum. When the resin/hardener starts to flow into the outlet tube, the process should be stopped and all inlet and outlet tubes should be clamped closed.

Debagging. After the manufacture recommended curing period is complete, the bag can be cut and the composite panel can be extracted. In our case the curing time is one week. Debagging needs to be done carefully to avoid damage to the sensors cables. The sensors first have to be released from the peel of ply (POP) covering the wire leads. Subsequently, the main layer of POP is then removed to expose the main glass-fiber epoxy.

Test specimen preparation and thermal treatment. After the panel has been removed from the bags and the cables safely separated from the panel, the panel can be cut into the desired shape. The test specimens can then be additionally cured in an oven to improve the performance. For the resin/hardener used in this thesis, it is recommended that the panel is cured at 120 C for 2 hours. Thermal curing is critical since it greatly improves high speed impact strength as can be seen in Figure 3-12. Here the panel was subjected to two high speed impacts before thermal treatment as can be seen by the two large delamination areas and then to four high speed impacts after thermal treatment. It can be clearly seen that the thermal treatment significantly reduces the extent of delamination from a high speed impact event. (The thermal treatment used in this thesis as not been optimized and could further improve the impact resistance of the panel).
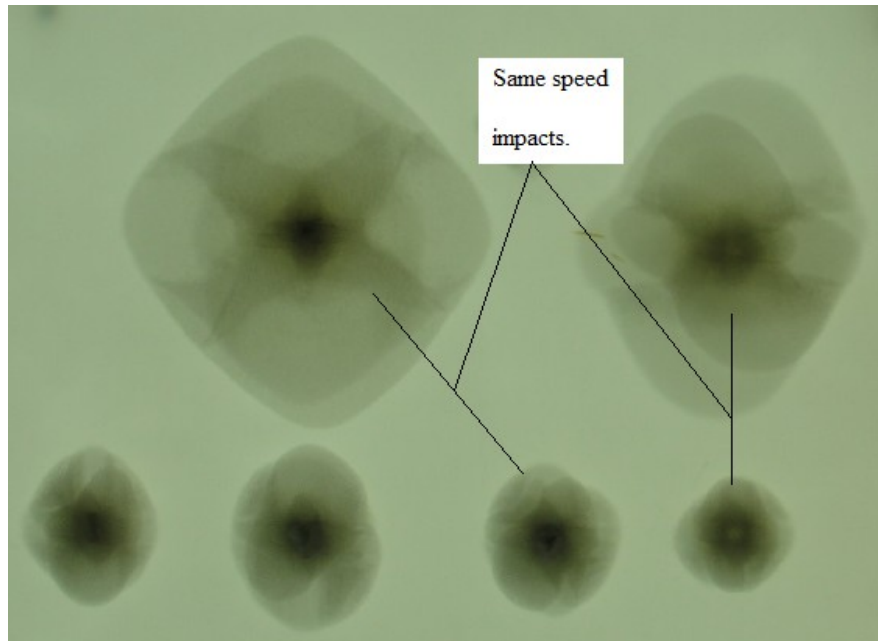
Figure 4-12 Panel SP19 subjected to high speed impacts; the thermal treatment improves the resistance to the delamination damage as can be seen by the two pairs of impacts with the same projectile speed. Impacts were performed with a .22 caliber FSP projectile at speeds around 300 m/s.

5   Damage location detection

It has been mention in the state of the art chapter that the first step for structural heal monitoring is to locate the position of the damage. On this work a novel detection technique has been developed. The novel technique focus on solving some of the problems related to the implementation of the techniques. Power consumption and cable routing are two real problems in the industry. Simplifying the calculations algorithms and place the sensors in such a way that simplifies the routing can have a real impact on the industrial applications of the techniques.

5.1   Conventional triangulation algorithm (CT)

The theory behind this classical technique is well known (Saponara, Horsley and Lestari, 2011; De Marchi et al., 2011) and is based on finding the distance (d_i) of the damage from sensor i based on the time of arrival (*TOA*) of the impact induced wave to the sensor, given by:

$$d_i = \sqrt{(x-x_i)^2 + (y-y_i)^2} = (TOA_i - T_0) \cdot C(\theta) \qquad (5\text{-}1)$$

Where, TOA_i, x_i and y_i are known (i.e. measured) and T_0, x, y are unknown variables that need to be calculated. TOA_i, x_i, y_i, T_0, x, y, and C are the time of arrival of the impact wave to sensor i, the x_i and y_i coordinates of sensor i, time of impact, x and y coordinates of the impact, and speed of the sound respectively. Since the time of impact (T_0) is not known a-priori, it can be eliminated from the system of equations by subtracting the distance equation from two sensors i and j to give

$$\frac{\sqrt{(x-x_i)^2 + (y-y_i)^2}}{C(\theta_i)} - \frac{\sqrt{(x-x_j)^2 + (y-y_j)^2}}{C(\theta_j)} = (TOA_i - TOA_j) \qquad (5\text{-}2)$$

This equation defines an isotemporal curve (or a group of curves) in the plane of the composite with identical difference of time of arrival ($\Delta TOA = TOA_i - TOA_j$). The intersection of those curves from various pairs of sensors then defines the impact position. A schematic of this method is shown on Figure 5-1with four sensors (S_1 to S_4). After impact the waves propagates from the impact position until it reaches the first and subsequent sensors (i.e. the wave first arrives at sensor 2 and then sensor 1 in Figure 5-1). These arrival times will define the time of arrival TOA_1 and TOA_2 etc. The isotemporal curves from each pair of sensors are shown for sensors 1-2, 1-3 and 2-3. In this case, the intersection of one pair of curves can be used to define the impact position. In general the intersection of the curves with experimentally measured TOAs will have some error and will give a collection of intersection points with more than one possible point of impact. Thus for real TOAs, redundant measurements are required to improve the reliability of locating the actual point of impact.
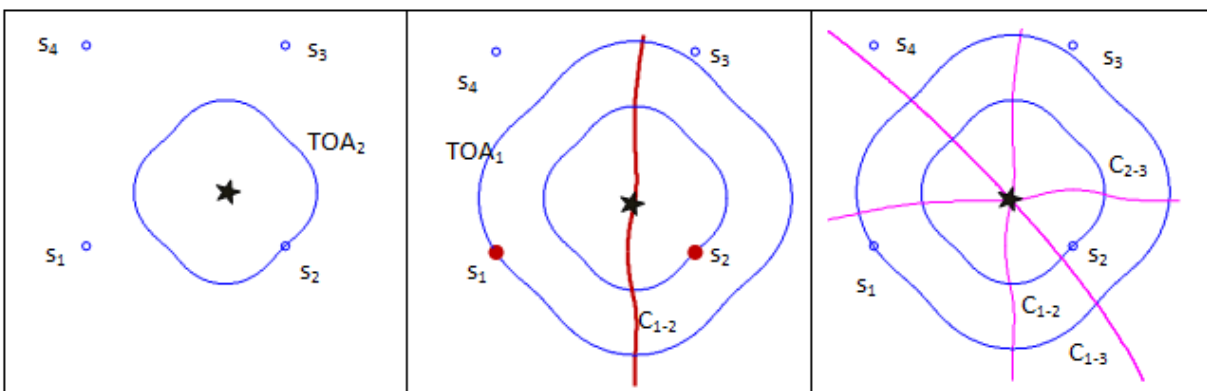
Figure 5-1 A series of figures showing the calculation process for the CT technique; on the left figure first the wave (shown in blue) from the impact (shown as a star) arrives at the closest sensors (s2) thus defining TOA2; then in the middle figure the impact wave arrives at sensor s1 defining TOA1. Using TOA1 and TOA2, the possible positions for the impact are defined along the isotemporal line C1-2 (in red) from Equation (5.1). This process is then repeated for all possible pairs of sensors leading to 6 isotemporal curves. The intersection of these curves are used to calculate the impact position; (only 3 curves have been represented in the right figure for clarity).

Critical to finding the isothermal lines defined in Equation (5.2) is the understanding of how waves propagate in anisotropic material and the associated wave speed dependence on propagation angle to the fiber direction - i.e. $C(\theta)$. For the isotropic case, the speed of sound for the P wave is constant and is given by Equation (5.3):

$$C_P = \sqrt{\frac{E\,(1+v)}{\rho\,(1+v)(1-2\,v)}} \qquad (5\text{-}3)$$

Where C_p is the speed of the sound for the pressure wave, E is the Young modulus of the material, ρ is the density of the material and v is the Poisson ratio.

There are another two solutions that give shear waves (particle displacement perpendicular to the direction of propagation). The two solutions are the same and are given by Equation (5.4):

$$C_S = \sqrt{\frac{E}{2\,\rho\,(1+v)}} \qquad (5\text{-}4)$$

Note that the pressure wave is always faster that the shear wave.

For a non-dispersive anisotropic material, and using a plane wave approximation, we can represent a plane wave by Graff (1975):

$$u_k = \phi_k \left(\frac{2\pi}{\lambda} (\hat{n}\vec{x} - Ct) \right) \qquad (5\text{-}5)$$

Where u_k is the displacement in direction k, ϕ_k is an arbitrary wave function and defines the initial shape of the wave, $\hat{n}$ is a vector normal to the direction of the plane wave, $\vec{x}$ is the position vector where the displacements are to be calculated, t is time and C is the speed of sound. Note that the direction of the plane wave given by $\hat{n}$ does not have to be parallel to the

displacement of the particles given by $\vec{u}$.   This can be substituted into the material wave equation obtaining the following 3 equations:

$$\left(D_{ijkl}n_j n_l - \rho\, C^2 \delta_{ik}\right)\phi''_k = 0 \qquad\qquad (5\text{-}6)$$

Where D_{ijkl} is the correspondent component of the anisotropic stiffness tensor and δ_{ik} is the Dirac delta function. For this problem to have a solution the following condition must be imposed:

$$det\left(D_{ijkl}n_j n_l - \rho\, C^2 \delta_{ik}\right) = 0 \qquad\qquad (5\text{-}7)$$

This eigenvalue problem gives 3 solutions for C^2 corresponding to the dilatational and distortional waves. The C^2 solutions incorporate wave that move in the $\hat{n}$ direction and in the opposite direction i.e. $-\hat{n}$. It can be proven that the dilatational wave is faster than the distortional waves An example of the wave speed dependence on angle in a composite laminate (with details given in Table 1 and the Experimental Section) are shown in Figure 5-2.   The associated wave fronts are also shown in Figure 5-2. For an isotropic material, the wave speed would be constant and the wave fronts would be circular.

The free boundary conditions of the plate only allow certain linear combinations of the solutions of equation 4.7, which generate guided waves (so called Lamb waves). For thick plates and/or high wave frequencies, the Lamb wave speed converges to the Rayleigh wave speed (Lamb 1915, Graff 1975). As can be seen in Figure 5-2, there is an increase in wave speed with increasing wave frequency which is typical for the A0 Lamb wave mode. The relatively small increase in wave speed with frequency shows that the guided wave is propagating close to the Rayleigh wave speed. Throughout this chapter the A0 Lamb wave velocity are assumed to be equal to the Rayleigh wave speed which greatly simplifies the calculations of the impact location

and also decreases the associated computational cost. This approximation is not valid for thin plates or for waves with low frequencies. Furthermore, experimental and modeling results from Morye et al. (2000) also imply that the A0 mode is likely to be dominant during high speed impact.
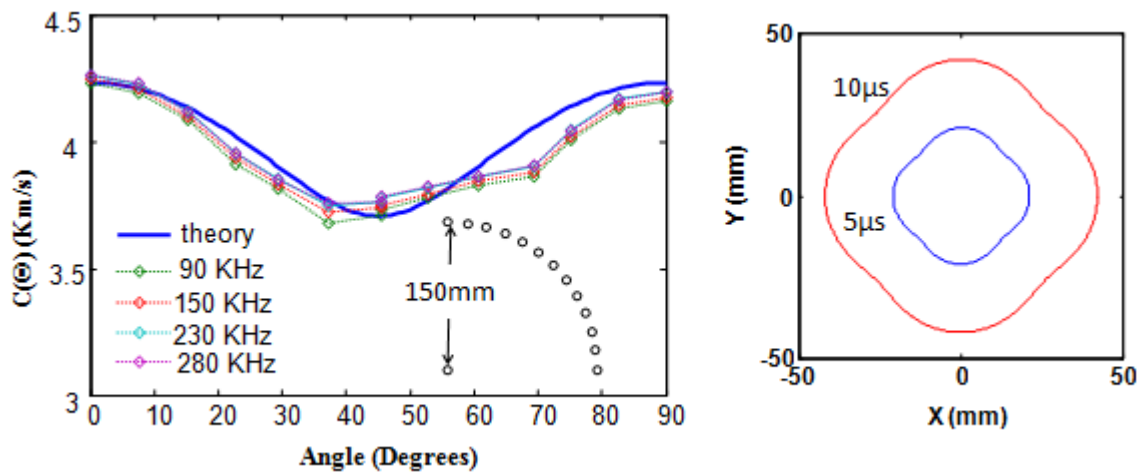
Figure 5-2 The speed of sound dependence on angle for wave propagation in an anisotropic material. The experimental results are shown as circles. The right figure shows the associated wavefront. The material parameters for these cases are given in Table1.

Once the speed of sound is known, the isotemporal curves given by Equation (5.2) can then be calculated. Figure 5-2 shows the isotemporal curves for the composite material with parameters given in Table 1. more detain in the measurement technique used can be seen in the experimental methods section.

 Note that Equation (5.2) is non-linear which means as shown in Figure 5-3, that the isotemporal curves form a complex pattern and that any two curves from different pairs of sensors can

intersect at 2 or more locations. Thus at least 4 pairs of ΔTOAs (and thus a minimum of 4 sensors in total) are needed to obtain a unique impact location. For the isotropic case, Equation (5.2) is simplified but also produces a set of non-linear impact location curves that can intersect at two points. A third independent ΔTOA is needed to find a unique impact location. (The third ΔTOA calculated in a 3 sensor case does not provide a unique intersection point and thus at least 4 sensors are needed to unambiguously find the impact location).
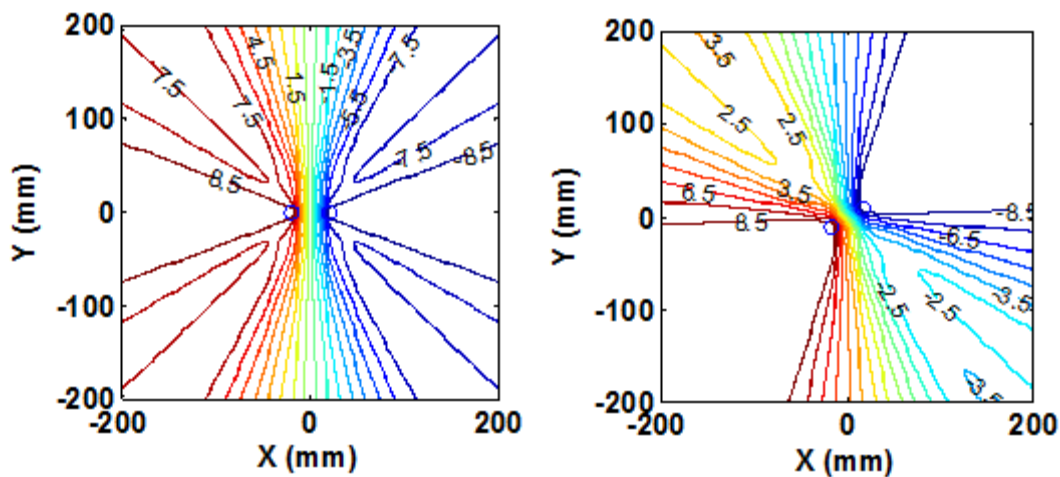
 Figure 5-3 Isotemporal curves for identical difference of time of arrival (ΔTOA) for two sensors (shown in blue) mounted on a composite plate; the sensors are 40mm apart. For the figure of the left, the sensors are at 0 degrees to the fiber direction. For the right figure, the sensors are at 30 degrees to the fiber direction. Note that for some ΔTOAs (such as 3.5us on the right figure) there are multiple isotemporal curves with the same ΔTOA. Times in the figures above are in us.

5.2   Some Issues with the CT Method

The nature of the conventional triangulation (CT) method requires finding the isotemporal curves for at least four sensor pairs and to calculate the intersection of these curves to determine the unique impact location point. This requires a two dimensional search and identification of the intersection of these

curves. When dealing with real-time i.e. continuous monitoring of the structure, this two dimensional search can be both time consuming and require substantial electrical energy. Furthermore, the inherent anisotropy of composite material means that the shape and characteristics of the wave front changes with impact location (Zhao, Gao and Zhang, 2007), i.e. the speed of sound is a function of angle. This makes the development of a generic CT detection algorithm complicated. Dispersion and absorption of the propagating wave in composite materials (and thin plates) also means that some frequencies will arrive before others effectively changing the shape of the wave front; therefore the TOA algorithm results are dependent on the distance of the sensor from the impact location. There have been some recent attempts to take into account wave dispersion for certain cases; for example De Marchi et al. (2007) analyzed the dispersion of propagating wave in thin aluminum plates and showed that different frequencies arrive at different times and thus demonstrated the problem caused by wave dispersion for calculating time of arrival. Since multiple Lamb modes are generated during high speed impact, the effect of wave dispersion is likely to be greater for the cases studied in this work.

For accurate measurement of impact location, the CT method requires the sensors to be located relatively far apart. Figure 5-4 shows the theoretical sensitivity of the CT method to a small (0.25μs) assumed error in TOA. It can be clearly seen from this figure that the error increases significantly when the location of impact is outside the area circumscribed by the sensor perimeter. However, when the impact is within this area, the error in position of impact is relatively small unless the impact position is very close to one of the sensors; this case however would be relatively easy to detect since the sensor will likely be damaged during the impact event. Thus as limited by practical concerns (such as wave attenuation), the sensors in the CT method should be spaced as far apart as possible to provide the greatest accuracy and coverage

area. This in turn means that the sensors have to be individually placed within the composite panels and electrical data/power wiring has to be carefully laid to each sensor location.
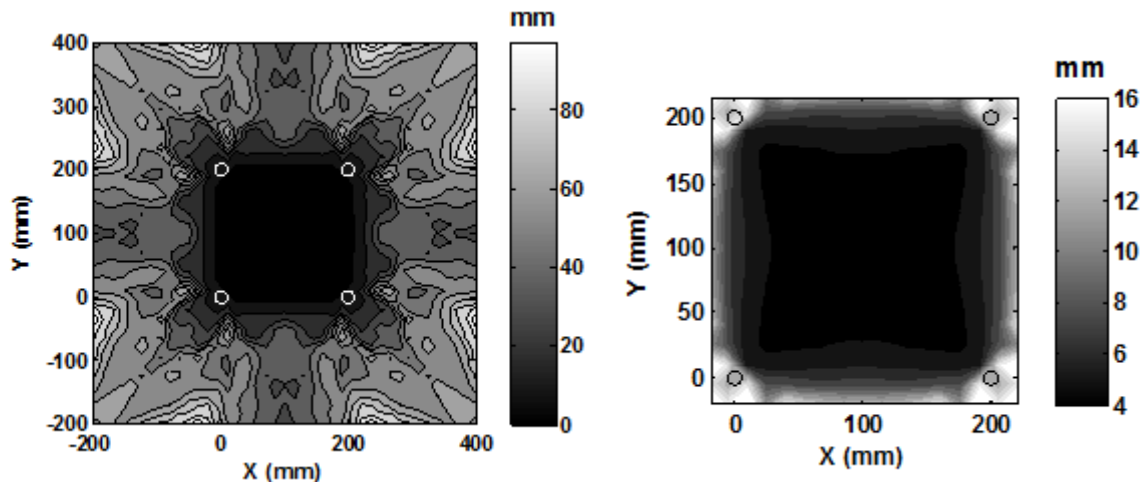
Figure 5-4 Error in position location (in mm) for an assumed 0.25µs error in TOA. The right figure is detailed view of the sensor area. It can be seen that the error grows rapidly from approximately 4.5mm at the center of the 4 sensor area to 16mm close to the sensors and to 100mm at a distance comparable to the sensor spacing.

5.3 Group Angle Detection (GAD) method

In order to overcome the above mentioned issues with the CT method, a novel location detection method similar to the one studied by Kundu, Nakatani and Takeda (2012) is proposed. The main idea behind this method is to group the sensors together and to locate the direction of the impact from the ΔTOA_{1-2} within each pair of sensors of a group as shown in Figure 5-5. Since the sensors are closely grouped together it is assumed that wave dispersion due to the wave propagation distance is the same for all sensors within a group. Furthermore, it is hoped that since the sensors are grouped together, placement of the sensors and the routing of data/power wires will be easier and cheaper. The GAD method is supported by previous work carried out using angle dependent impact measurement techniques i.e. fiber optic Bragg grating sensors (Betz et al., 2007) and lead

zirconate titanate (PZT) or macrofiber piezocomposite rosettes (Salomone et al., 2010, Lanza di Scalea et al., 2011). These previous techniques used inherently directional sensors (i.e. sensitive only in one direction) to calculate the angle of the impact by comparing the magnitude of the measurement of 3 sensors. Our proposed technique differs to these techniques since it uses plane isotropic sensors and time of arrival to calculate the angle. Therefore the previous techniques provide one measurement for every 3 sensors while the GAD technique presented in this thesis provides 3 impact location angles from 3 sensors, potentially averaging out any errors. Furthermore the proposed technique does not depend on magnitude measurement which could be dependent on the attenuation and dispersion within the material. The work outlined in this thesis builds on prior research by Ciampa and Meo (2010), Ciampa, Meo and Barbieri (2012) and Kundu, Nakatani and Takeda (2012) that used sensors that are closely spaced compared with the distance to the impact. Thus in previous work the angle to the sensors is calculated assuming that the speed of the sound is constant for all sensors within a group. Furthermore, three closely spaced sensors are needed to obtain the impact angle; however wave speed is not required for these methods. The technique proposed in this work takes into account the second order correction that comes from the different speed of sound arriving at each sensor due to the inherent anisotropy within composite materials. This correction considers the effect of angle between the wave front and the direction of wave propagation. Furthermore, a novel computationally efficient algorithm that can be more readily performed on mobile electronic systems is introduced for finding the impact location. Since the speed of sound and positions of sensors are known a-priori in the current technique, each pair of sensors can be used for the calculation of the impact angle; this in turn increases the flexibility in the possible sensor placement within a panel.
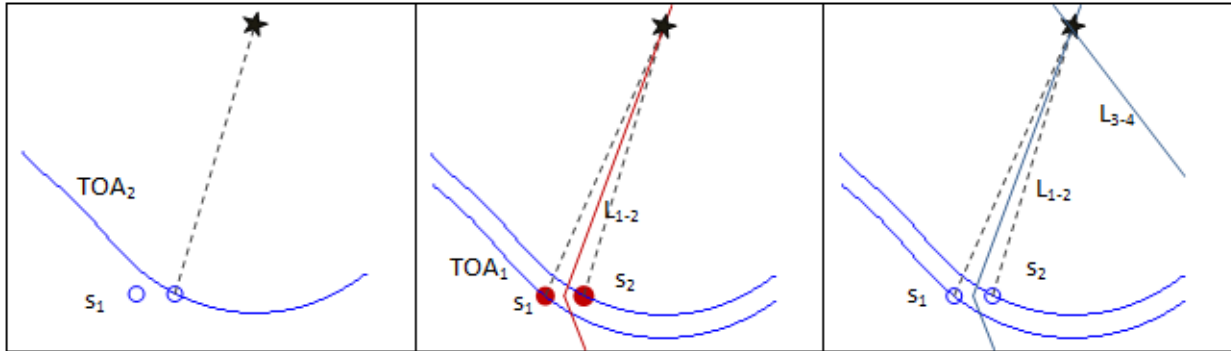
Figure 5-5 A schematic depiction of the sensor group (GAD) technique. The wave first arrives at sensors 2 with TOA2. The wave then arrives at sensor 1 (middle figure) with TOA1. Using ΔTOA1-2 the lines L1-2 are calculated corresponding to the direction of the impact. Note that from just one ΔTOA1-2 measurement, two directions are possible as seen by the bottom line. In the right figure, another pair of sensors (3 and 4) (located outside the figure) are used to calculate the line L3-4. The intersection of these lines gives the impact location.

In this case the calculation of the position of impact can be greatly simplified as shown in Figure 5-6. The relationship that governs the angle of the impact location from the sensors (θ) is given by relatively straightforward trigonometric considerations (as shown in Figure 5-6) as:

$$d_{12} \cos(\theta - \theta_{12}) + d_{12} \sin(\theta - \theta_{12}) \tan(\theta_f) = (TOA_1 C(\theta_1) - TOA_2 C(\theta_2)) \cong$$

$$\cong (TOA_1 - TOA_2) \, C(\theta) \qquad\qquad (5\text{-}8)$$

Where d_{12} is the distance between the sensors, θ_{12} is the angle between the line joining the sensors and the composite fiber direction, θ_f is the angle between the normal direction to the wave front and the line joining the sensors and the impact position and is function of θ, $C(\theta)$ is the speed of the sound in the direction theta, and TOA$_i$ is the time of arrival of the signal to sensor i. The second term in the left side is in effect a second order correction on the wave speed

and is equivalent to having a different speed for each sensor within a pair. In an isotropic material θ_f is zero, but is non-zero in anisotropic composite materials and can be calculated from composite material theory using simple trigonometry.

Note that in the GAD formulation, only the angle θ between the sensors and the impact point is unknown, therefore the computational cost when compared to the CT method (where the x and y location of the impact are unknowns) should be reduced.
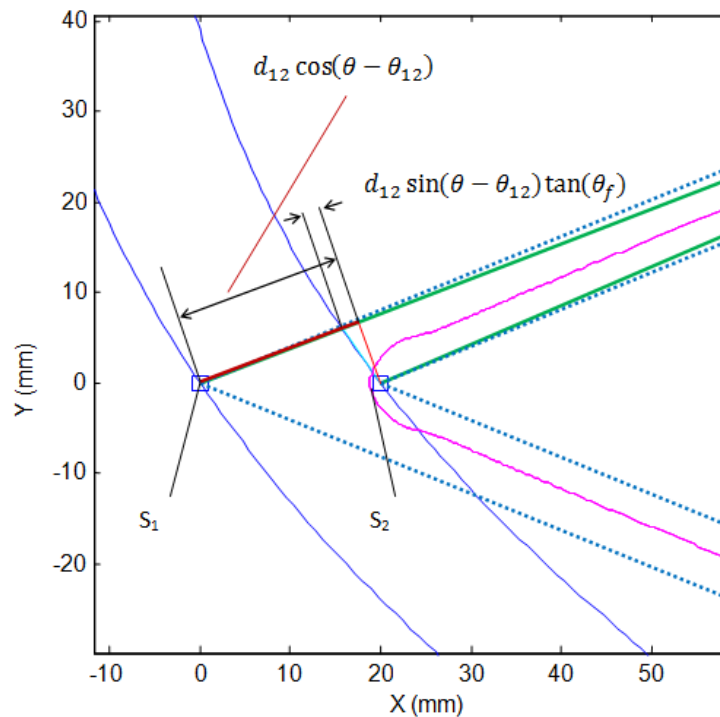
Figure 5-6 Schematic of the GAD technique. The impact location is at 200mm from the sensors (not shown). The solid (green) straight lines are the direction between the impact position and the sensors, the dotted (blue) lines are the approximate angle, the purple line is the isotemporal ΔTOA curve for the two sensors. The (dark blue) curved lines are the wave fronts when they reach the sensors.

Figure 5-7 shows the effect of impact angle (θ) on the predicted difference in time of arrival

(ΔTOA) for a wave propagating in a composite material (parameters taken from Table 1). The

distance between the sensors is 40mm and the sensors lie along the fiber direction. As expected,

ΔTOA is maximum when $\theta = 0$ degrees (i.e. sensors are perpendicular to the wave front) and

zero when the impact is at $\theta = 90$ degrees (i.e. sensors are parallel to the wave front). Note that

when the impact angle is 0 or 180 degrees, small errors in measuring ΔTOA can lead to large

errors in calculated impact angle, while at 50 to 120 degrees the same error in ΔTOA leads to

relatively small errors in calculated impact angle. The dependence of impact angle on ΔTOA is

material dependent and is also dependent on the orientation of the sensors to the fiber angle as

can be seen in Figure 5-8 where the sensors are located at 30 degrees to the fiber direction.

(Hereafter these large error regions in ΔTOA impact orientation are referred to as '*the large

error regions*'). Furthermore, for some ΔTOA values, there can be two, four or six impact

directions; for example given $\Delta TOA = 8us$ (in Figure 5-7) there are 6 possible impact directions.

(Hereafter these multiple solutions in ΔTOA impact orientation are referred to as '*the multiple

solution regions*').
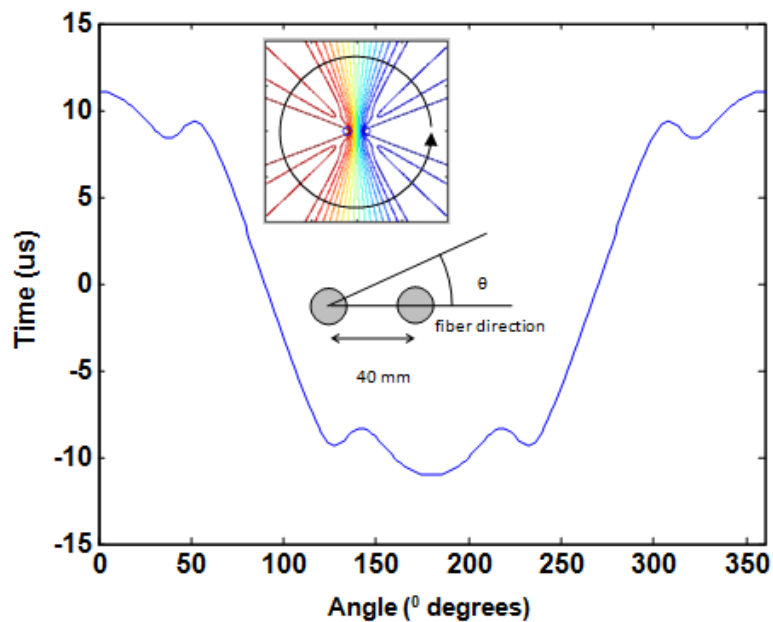
Figure 5-7 Dependence of ΔTOA on impact direction for two sensors spaced 40mm apart and aligned at 00 to the fiber direction. Material parameters are taken from Table 1.
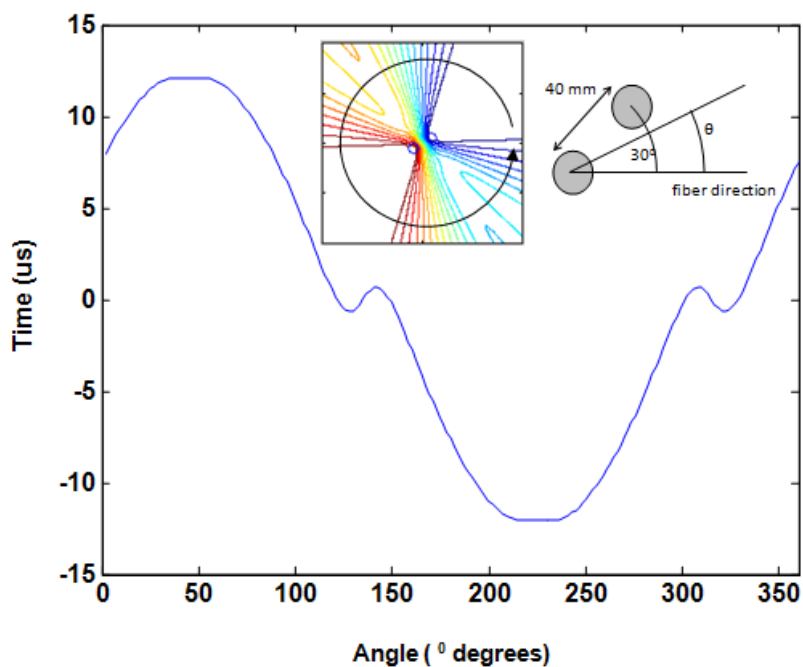
Figure 5-8 Dependence of ΔTOA on impact direction for two sensors spaced 40mm apart and aligned at 300 to the fiber direction.

5.4   Comparison of CT and GAD Algorithms

The CT algorithm consists of the following Steps:

1. TOA calculation.

2. 2 dimensional isotemporal curves calculation. Note that due to the anisotropy of the composite panel a maximum of 3 individual curves can be generated by a pair of sensors as can be seen in Figure 5-8, where the highlighted curves are for $\Delta TOA = 7.5us$.

3. Repeat Steps 2 for a minimum of four sensor pairs.

4. Calculation of intersection of isotemporal curves which is dependent on the number of sensor pairs. For example: 28 pairs of sensors can be constructed with 8 sensors (n!/(n-2)!/2!), which in turn means that no less than 28 isotemporal ΔTOA curves are generated and therefore the number of intersection is no less than 756 (i.e. n·(n-1)=28·27=756)

5. Due to experimental error, the location of the impact calculated from two different pairs of sensors may not coincide. A method is then needed to find the best estimate of the impact position, for example by taking the mean of the impact calculations for each sensor pair.

In general Steps 2 and 3 require a two dimensional search to find all x, y positions of the isotemporal curves and their intersections. Due to the multiple curves and intersections that can be generated in the CT method, a reliable search method (for example a grid search) needs to be performed in order not to miss any of the possible solutions. Figure 5-9 shows an example of multiple curves for a pair of sensors.

The GAD algorithm consists of the following steps:

1. TOA calculation

2. The angles that satisfy Equation (5.8) are calculated; in general there can be 2 to 6 possible solutions

3. The intersection of the straight lines defined by the angles in Step 2 are then calculated, this is a simple algebraic calculation

4. Due to experimental error, the location of the impact calculated from two different pairs of sensors may not coincide. A method is then needed to find the best estimate of the impact position, for example by taking the mean of the impact calculations for each sensor pair

For the GAD method, Step 2 is a one dimensional search for the impact angle. Since there can be multiple impact angles that satisfy Equation (5.8) a reliable search algorithm (such as a one dimensional grid search) is needed to find all possible solutions.

Since the GAD algorithm requires a one dimensional search and a straightforward intersection calculation for the lines calculated for each sensor pair, it is expected that the GAD method will have substantial computational savings over the CT technique which requires a two dimensional search for the isotemporal curves as well as for the points of intersection of these curves.
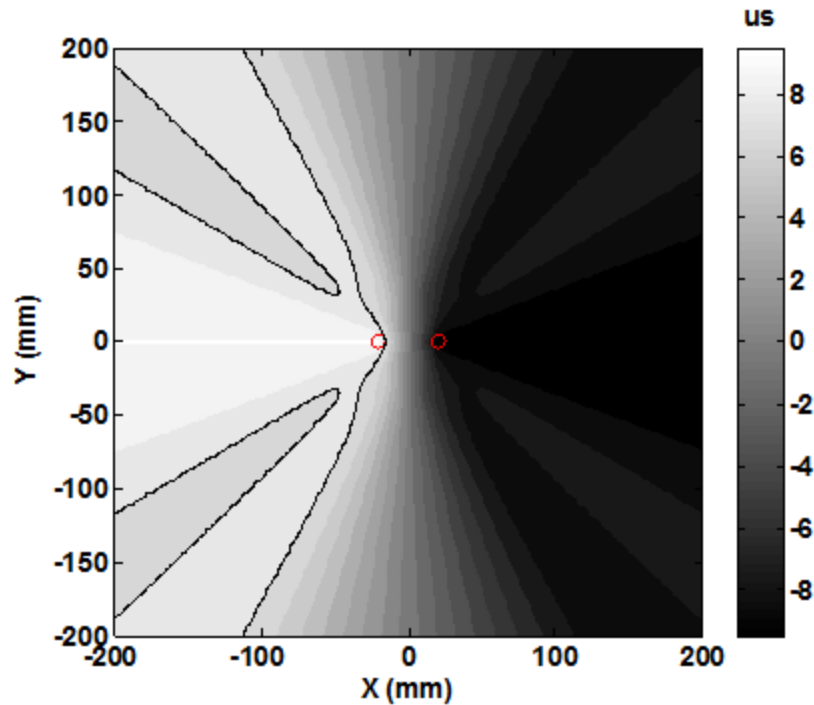
Figure 5-9 Plot of the ΔTOA isotemporal curves for a composite plate with parameters given in Table 1. In some special cases there is more than one possible curve for the same ΔTOA as shown by the multiple curves for ΔTOA=7.5us

5.5   Experimental Methods

Glass fiber (S2-6187 - HEXCEL) and an epoxy matrix (EPON 828 - MOMENTIVE) with a $[0/90]_{10s}$ layup and with overall dimensions 12x12x1/4" (305x305x6.4mm) were manufactured using a vacuum infusion technique. Circular lead-zirconate-titanate (PZT) piezoelectric sensors where embedded under the first ply. The size of the sensors was 6.4mm diameter by 0.191mm thick (1/4" diameter by 0.0075" thick). To be able to use the CT technique all panels had sensors in each corner of the panel. For the GAD technique, four different sensor distributions where tested. One more panel was also build where the sensors where placed with a smaller perimeter to be able to measure the increased error of the CT technique outside the sensors array. Figure

5-10 shows the configurations of panels used on these experiments. Note that not all panels were exactly the planned 308mm size since allowance had to be made for the presence of the embedded sensor wires during panel cutting. However a minimum distance of 25.4 mm from the sensors to the side of the panels was maintain in all cases to avoid any reflected wave interference.

Both location techniques used on this chapter require knowledge of the speed of the sound in the composite material. The speed of the sound was measured using both a commercially available ultrasound machine (Epoch 1000i - OLYMPUS) and using a PZT sensor array. A composite panel had one centrally mounted PZT acting as an emitter and 13 PZT sensors in an angular distribution surrounding the central PZT (see the inset in Figure 5-2). The commercially available ultrasound machine (Epoch 1000i) showed the same results as the PZT array for the 0 and 90 degree angles.

Since the laminate used in the experiment has tetragonal symmetry, the D tensor has a reduced number of independent parameters. Using the conventional two index notation for the D tensor, the tensor can be represented by a 6x6 matrix:

$$D = \begin{bmatrix} D_{11} & D_{12} & D_{13} & 0 & 0 & 0 \\ D_{12} & D_{11} & D_{13} & 0 & 0 & 0 \\ D_{13} & D_{13} & D_{33} & 0 & 0 & 0 \\ 0 & 0 & 0 & D_{44} & 0 & 0 \\ 0 & 0 & 0 & 0 & D_{44} & 0 \\ 0 & 0 & 0 & 0 & 0 & D_{66} \end{bmatrix} \; where \; S = D^{-1} = \begin{bmatrix} S_{11} & S_{12} & S_{13} & 0 & 0 & 0 \\ S_{12} & S_{11} & S_{13} & 0 & 0 & 0 \\ S_{13} & S_{13} & S_{33} & 0 & 0 & 0 \\ 0 & 0 & 0 & S_{44} & 0 & 0 \\ 0 & 0 & 0 & 0 & S_{44} & 0 \\ 0 & 0 & 0 & 0 & 0 & S_{66} \end{bmatrix}$$

$$S_{11} = \frac{1}{E_1} \; , \; S_{12} = \frac{v_{12}}{E_1} \; , \; S_{13} = \frac{v_{13}}{E_3} \; , \; S_{33} = \frac{1}{E_3} \; , \; S_{44} = \frac{1}{G_{23}} \; , \; S_{66} = \frac{1}{G_{33}} \qquad (5\text{-}9)$$

Because of the symmetry of the panel, only 6 parameters are unknown: E_1, E_3, ν_{12}, ν_{13}, G_{23}, and G_{12}. Since we are interested only in waves that propagate in the x direction of the panel, the normal vector $\hat{n}$ has the values:

$$\hat{n} = [\cos\theta\ ,\ \sin\theta\ ,0] \qquad\qquad (5\text{-}10)$$

Examining Equation (5.7), it is clear that D_{66} has no contribution to the calculation and can be omitted. Thus there are 5 parameters of interest: E_1, ν_{12}, and G_{23} which were measured from 0^0 and 45^0 static tensile tests. Finally, ν_{13} and E_3 were calculated to minimize the least square difference from the calculated speed of sound and the experimentally measured speed of sound. These values are listed Table 4.1 below.

Table 5-1Compliance matrix parameters measured by tensile tests or calculated from a least square fit of the speed of the sound measurements.

Parameter	Value	Technique
E_1	25.8 GPa	Tensile test
ν_{12}	0.11	Tensile test
G_{23}	4.22 GPa	Tensile test
E_3	9.6 GPa	Least square fit of speed of sound
ν_{13}	0.21	Least square fit of speed of sound

The composite plates were then subjected to high speed impacts (~310m/s) from a .300 caliber single stage gas gun; steel projectiles of .22 caliber (5.56mm) and weighing 22 grains (1.42g) were used. The projectiles (shown in Figure 5-11) were armor piercing (AP), and were designed by Frontier Performance Polymers Inc. (Dover, NJ).

The speed of projectiles was kept at approximately 310m/s as measured by a high speed camera (IMACON 200) which is the V50 speed for the particular panel and projectile.

Every panel was shot 11 to 14 times starting at the top left corner and moving to the right midpoint as can be seen for one of the panels in Figure 5-12. The distance between shots was kept greater than 2 inches (50.8mm) to avoid interference of the delamination damage of previous shots with the subsequent ones. This sequence of shots does not interfere with the measurements for the GAD technique, since a clear line of sight is maintained between the sensors and the impact but could lead to some degradation of the measurements for the CT method.

A NI-PXI data acquisition system (National Instruments) with two simultaneous sampling DAQ cards (8 channels total) at a 4Msps rate was used to acquire the signal from the PZT sensors. Due to the high voltage output of the PZT sensors during high speed impacts, a voltage splitter was used to lower the input voltage to the allowable ±10V of the NI-PXI acquisition cards with one of the sensor channels being used to trigger the acquisition. The capacitances of the sensors between shots were measured to check that both sensors and cables remained undamaged. Cracking on the PZT can be easily detected in this manner since the capacitance typically drops if damage of the sensor occurs. However no damage of any of the PZT sensors was detected during the tests.

Since the shots were carried out at subsonic speeds, in some cases a premature triggering of the signal prevented data acquisition due to the shock wave arriving at the sensor before the impact wave. As a consequence, data from some of the shots was unusable. Changes in material properties due to damage was not taken into account in this work.
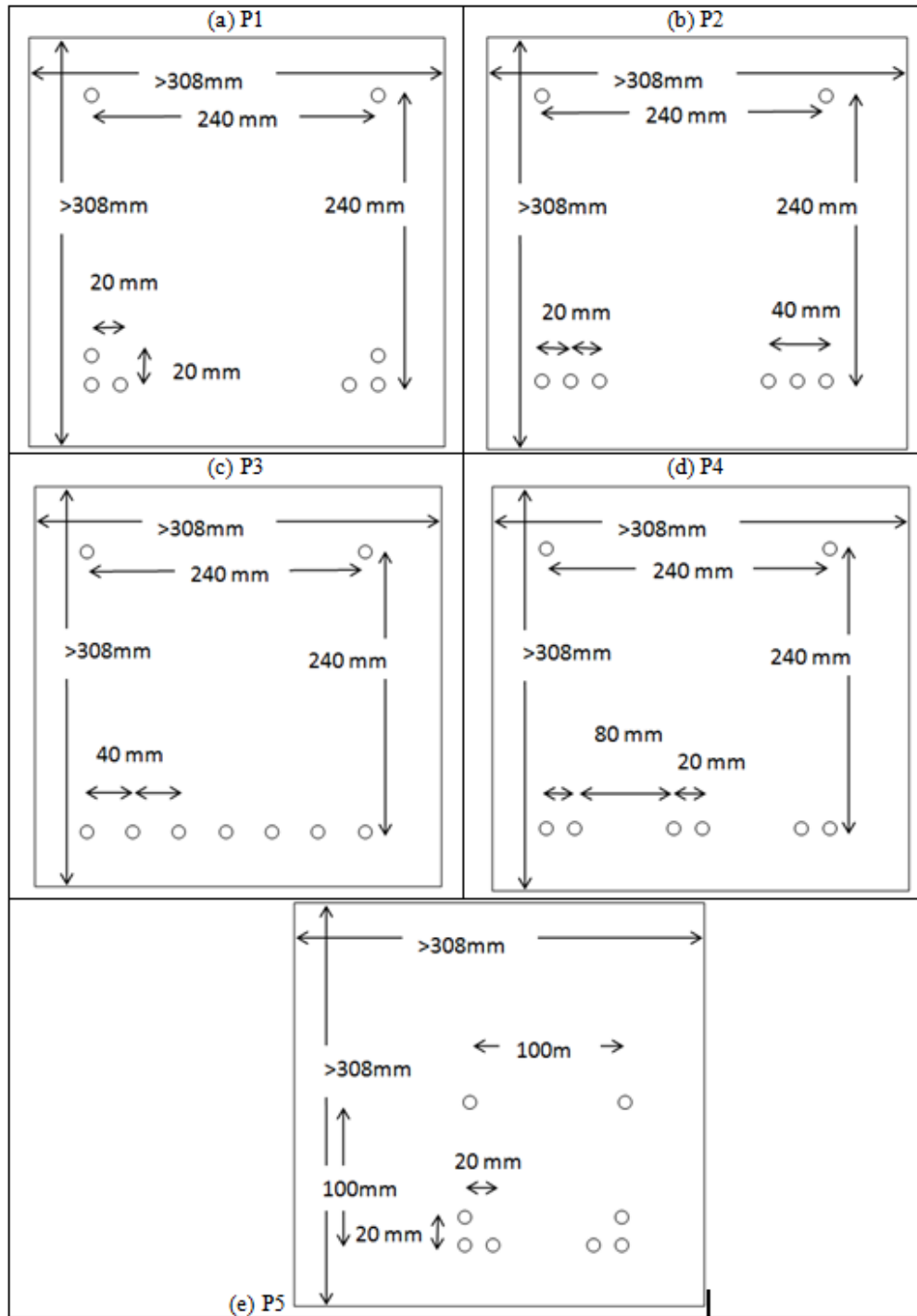
Figure 5-10 Composite panel configurations: (a) P1 test panel - L shaped sensor groups (b) P2 test panel - two groups of three linear sensors, (c) P3 panel - linear distribution of sensors, (d) P4 - panel, three pairs of sensors in a line and (e) P5 panel -L shaped sensor groups with a smaller perimeter.
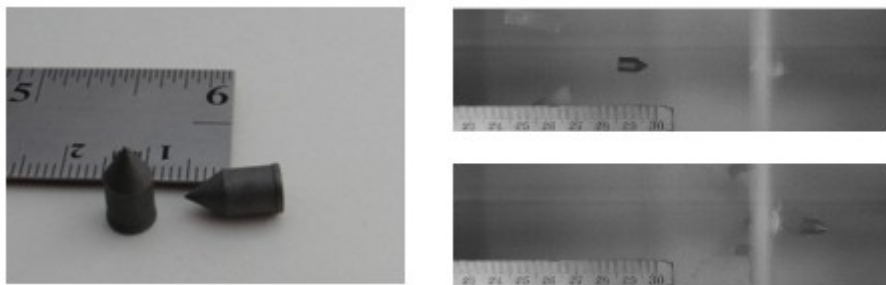
Figure 5-11 AP projectiles on the left and high speed images of the same projectile as it pierces a composite panel.
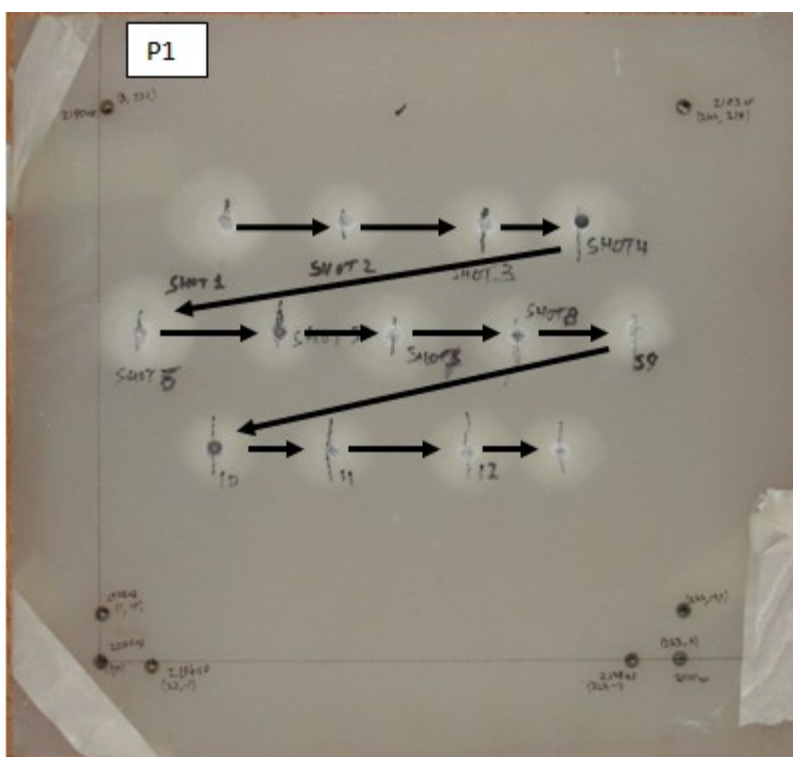
Figure 5-12 Order of impacts carried out on panel P1.

5.6   Results and Performance of CT and GAD Techniques

Table 2 shows the error in predicted impact position of the CT and GAD techniques for the five composite panels (P1 to P5) subjected to a total of 52 impacts. As expected the GAD technique shows a larger location error than the CT technique. There is a relatively small effect of sensor topology (i.e. layout of the sensors) for the CT technique as shown by the average errors (15.3, 14.9, 22.0 and 14.9 mm) for the first four panels. As expected the CT error in the fifth panel was higher since the impacts were located outside the perimeter of the sensors (53mm average error). In general the GAD technique shows slightly less accurate results than the CT technique as shown by the average error (19.9, 40.2, 34.0, 13.0 and 40.5mm). For the GAD technique the sensor topology seems to play a more important role with the P1 topology being somewhat better than the others. Note that the sensor spacing in the P1 panel is smaller than for the other panels and since ΔTOA error is dependent on the spacing between sensor pairs, the P1 sensor topology has a better overall relative error. For the GAD technique there is a less significant effect on location error (as opposed to the CT technique) when the impacts are outside the sensor perimeter (i.e. panel P5); again the error in panel P5 is double that of panel P1 since the distance between the sensor groups in P5 is half of distance between the sensors in P1 (see Figure 5-10).

For both the CT and GAD techniques a simple cross-correlation technique was used in order to determine the TOA, the cross correlation signal was taken using a portion of one of the signals; the segment was chosen to including some of the pre-arrival signal and part of the signal after arrival. In most cases this simple cross correlation technique was adequate for accurate determination of TOA but in certain cases as previously mentioned, the shock wave of the projectile arrived at a sensor/s before the impact wave (these cases have been eliminated from Table 2) and in some cases the shock wave arrived approximately at the same time in which case

UNCLASSIFIED

an error in TOA can be expected. This for example is believed to be the reason for the relatively

large location errors in the CT algorithm for shot 4 in panels P2 and P4. (Digital filtering of the

signal was applied but did not improve the results; an analog band-pass filter could possibly be

used to eliminate this effect but was not performed in these experiments).

Table 5-2 The error in impact location for the CT and GAD Techniques.

Location Error (mm)										
Impact Number	P1		P2		P3		P4		P5	
	CT	GAD	CT	GAD	CT	GAD	CT	GAD	CT	GAD
1	9.3	16.6	7.0	15.2	78.0	26.4	6.2	17.0	-	-
2	7.8	19.8	-	-	-	-	6.5	9.8	116.2	34
3	36.7	3.2	19.6	32.3	12.9	7.7	4.2	6.7	43.9	-
4	5.9	25.4	69.5	23.9	15.6	32.2	89.6	24.8	86.6	85.0
5	-	-	15.3	74.4	20.6	35.2	13.2	11.2	68.0	19.0
6	-	-	7.1	52.9	-	-	8.6	15.9	57.3	77.3
7	5.8	59.2	6.2	44.6	4.9	99.1	2.7	7.0	21.0	76.8
8	-	-	2.1	17.7	1.7	44.1	12.7	5.1	53.2	14.8
9	-	-	10.2	86.2	4.6	30.0	9.7	9.9	15.4	46.4
10	-	-	7.7	36.3	-	-	15.3	9.2	66.1	9.8
11	-	-	13.6	26.6	12.9	63.3	4.8	24.5	2.35	2.6
12	15.7	7.1	-	-	10.7	28.7	8.7	18.5	-	-
13	26.0	7.8	5.7	31.7	18.3	4.3	4.1	9.5	-	-
14	-	-	-	-	6.0	3.5	22.0	36.13	-	-
Average	15.3	19.9	14.9	40.2	22.0	34.0	14.9	13.0	53.0	40.5

For both the CT and GAD techniques a simple cross-correlation technique was used in order to

determine the TOA, the cross correlation signal was taken using a portion of one of the signals;

the segment was chosen to including some of the pre-arrival signal and part of the signal after

arrival. In most cases this simple cross correlation technique was adequate for accurate

determination of TOA but in certain cases as previously mentioned, the shock wave of the

projectile arrived at a sensor/s before the impact wave (these cases have been eliminated from

Table 2) and in some cases the shock wave arrived approximately at the same time in which case

an error in TOA can be expected. This for example is believed to be the reason for the relatively

large location errors in the CT algorithm for shot 4 in panels P2 and P4. (Digital filtering of the signal was applied but did not improve the results; an analog band-pass filter could possibly be used to eliminate this effect but was not performed in these experiments).

For the GAD technique, Figure 5-13 shows four typical results. Figure 5-13(a) shows a relatively accurate determination of the location of the impact (P1 – shot 1 with location error of 16.6mm). Figure 5-13(b) shows a relatively large error in impact location using the GAD technique (P1- shot 7 with location error of 59.2mm); this error is likely due to measurement error in TOA in some of the sensor pairs. Note that the CT technique does not suffer from the same problem since it also uses information from the sensors above the impact location. Figure 5-13(c) shows that there is a loss of accuracy for the GAD technique as the angle of the impact to the sensors increase (P3- shot 11 with an error of 63.3mm). This phenomena was explained in Figure 5-7, where it was shown that at impact angles greater than 120 degrees to the sensors, the GAD method becomes error prone (i.e. small changes in ΔTOA lead to large changes in angle). However as can be seen in Figure 5-13(d), this effect can be mitigated provided that there are sufficient intersections of the location angles which average out the ΔTOA error.
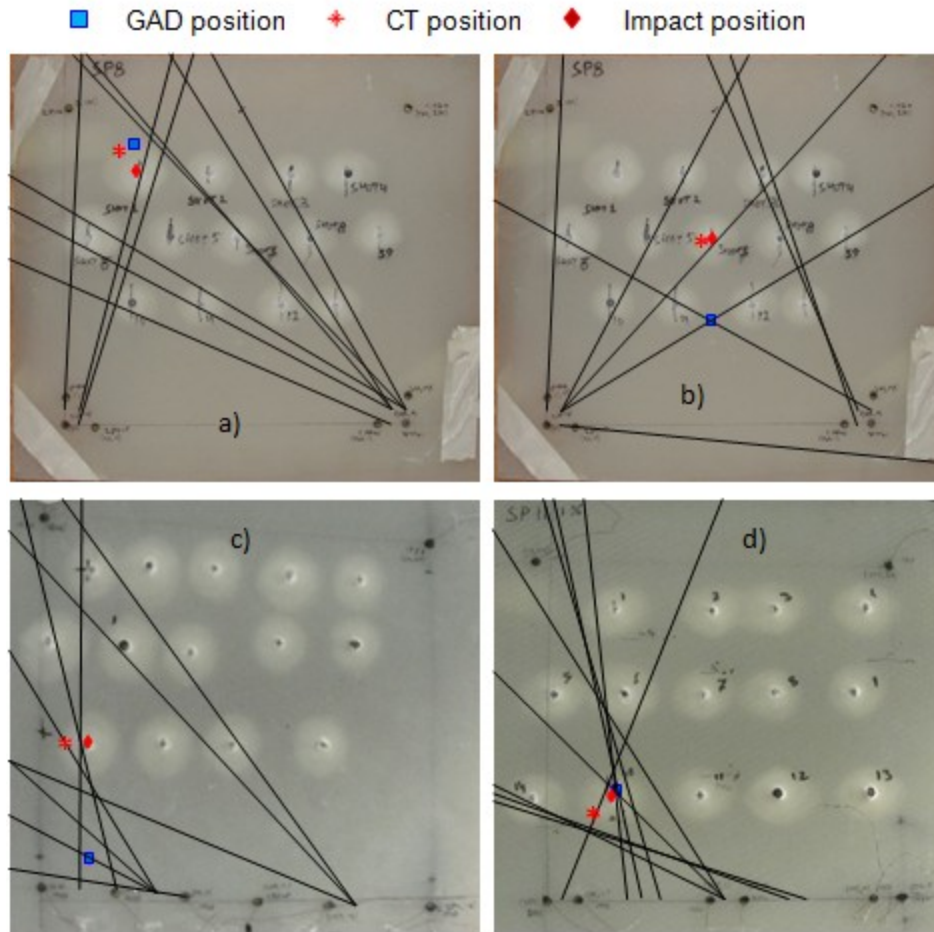
Figure 5-13 The results of the CT and GAD techniques for calculating the position of 4 different impacts. The black lines show the orientation lines calculated by the GAD technique (a) P1 (shot 1) shows an accurate calculation, (b) P1 (shot 7) shows an error in locating the impact due to TOA measurement error and multiple solutions error, (c) P3 (shot 11) shows an error in locating the impact due to measurements in the large error regions from the sensors on the right, and (d) P4 (shot 10) showing a relatively accurate impact location even though angles to some sensors are in the large error regions. Some lines that do participate in the calculation but whose intersections are discarded (like complementary angles with intersections on the negative y-axis) are not shown for clarity.

The large error regions in the GAD technique can be further understood by considering the location error distribution and the L-shaped sensor geometry and impact position shown in Figure 5-13b). For this time of arrival, three possible solutions are generated by one of the

sensor pairs in the group on the left (For the other two sensor pairs in the left hand group, the TOAs lie in the large error regions and are thus inaccurate**)**. However, the average of the solutions of the right sensor group approximately crosses the impact damage location; thus a better solution (i.e. without multiple solutions or using more sensor pairs) could compensate for the error on this case. Figure 5-14 shows the sensitivity to a 1/4μs error for the GAD technique and a panel of approximate shape as the panel in Figure 5-13(b). The areas of higher error that are seen in this figure corresponds to multiple impact orientations for the same ΔTOA as can be seen from Figure 9; thus a small error on ΔTOA can cause the calculated orientation to jump from one isotemporal part of the curve to another and therefore introduce a large error in the orientation calculation. Note that the error is greater at the center of the panel as opposed to the CT technique where the error is less in the center of the panel. Figure 5-14can thus be used to explain the high error detected on some of the GAD results in Table 2. For example, shot 7 in panels P1-4 is approximately in the center of the panel and those impacts have locations error that are above average for panels P1-P4. Shot 7 for P4 has a smaller than average location error but this could be because the average ΔTOA error was smaller for that particular case. This source of error could be reduced by using more populated groups, whereby the isotemporal lines with multiple angle solutions could be discarded. Due to limitations on the number of sensors this was not possible in the present work. Note that this error introduced by multiple solutions of the isotemporal curves does not affect the error of the CT technique when the impact location is within the sensors array. However multiple solutions are responsible of the higher error outside the sensor area as can be seen in Figure 5-4. This result can also be explained by the fact that when the impact is outside the sensor area, the sensors for the CT technique can be considered to act as a single sensor group.
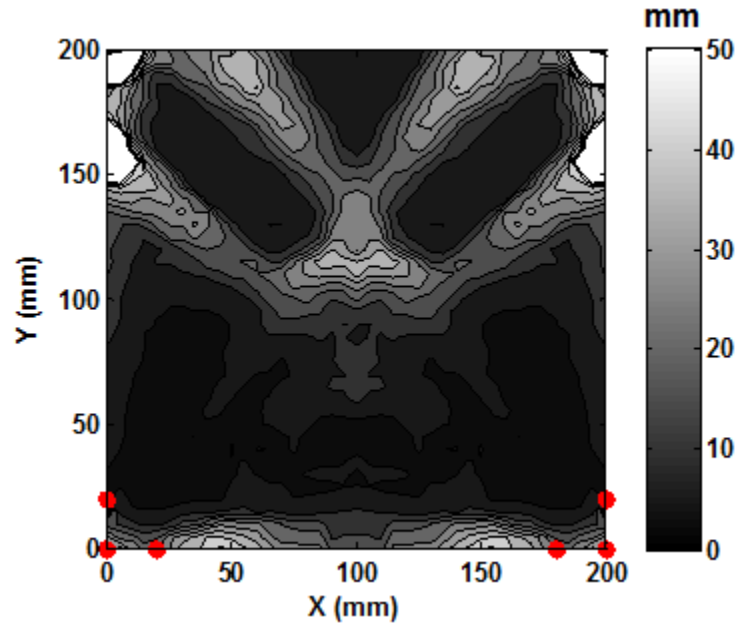
Figure 5-14 Error in the GAD technique associated to 1/4μs error in TOA. Sensor positions are shown as red circles.

5.7 Comparison of Speed of Algorithms

Both algorithms where implemented in Matlab® 2012 on a PC (Dell Inspiron 580, RAM 8Gb, Intel® Core™ i5 CPU, 650@3.20GHz, 64 bits) computer. Internal Matlab timing commands were used to measure the time of execution of each program (i.e. CT and GAD techniques). In each algorithm the TOA calculation is common. In order to assess the effects of the number of sensors used in each case, the total time for calculating impact position as a function of the number of sensor pairs was determined for both algorithms. Note that there a maximum of 12 pairs can be constructed for the GAD technique, while 22 pairs were used as a maximum for the CT algorithm. Panel P4 was used for this algorithm speed measurements; all 14 valid shots of the panel where used in the calculation that was run 2 times (to obtain a statistical sample size);

giving a total of 28 calculations for each sensor pair. Table 3 shows the average results of 28 executions of the software; algorithm run times were almost identical for each case.

From Table 3 it can be seen that the GAD technique's algorithm scales linearly with the number of sensor pairs since the time to calculate the orientation angle for each pair of sensors is fixed, and this is the most computationally expensive step in the algorithm. Note that the line intersection calculation is not linear since it involves the calculation of $n(n-1)/2$ crossings (where n is the number of lines); this operation however is very fast - typically 3 orders of magnitude faster than calculating the orientation angle and thus has a negligible effect on overall algorithm run time. A similar effect was detected for the CT algorithm, where there is also little effect on the algorithm speed with an increasing number of sensor pairs due to the efficiency of the implemented 2D search. In the CT algorithm efficiency is greatly improved by using a multigrid search method which combines the isotemporal line generation (step 2), the intersection calculation (step 3) and selection of intersection (step 4) in a single step. Initially a coarse grid of the probable impact area is selected covering the entire panel. A pair of sensors is then selected and a theoretical ΔTOA_{th} is calculated at each grid pair for the specific sensor pair. The experimental ΔTOA_{ij} is then calculated for the sensor pair. The required curve will cross though points with $\Delta TOA_{ij} - \Delta TOA_{th} = 0$. All these differences for all the pairs are then summed. A perfect intersection of curves will have a total difference equal to zero. Since there is typically an error in the TOA calculation and since the grid is coarse, this will not be the case in practice. Points on the grid with a sum smaller than a selected threshold are then chosen and a new refined grid can be build containing only those points. The search is refined until the grid is deemed fine enough (0.5mm in our case), at which point the local minimum positions give the required intersection points. Note that a gradient search for the minimum positions was not used because

there are many possible solutions for each intersection of curves (i.e. local minimums). Hence for a gradient search more than one starting point would be necessary; this greatly reduced this method's efficiency.

Table 5-3 Measurements of algorithm time for the CT and GAD techniques as a function of the number of sensor pairs.

	22 pairs	18 pairs	12 pairs	6 pairs	3pairs
CTT	2.43s	2.19s	1.89s	1.55s	-
GAD	-	-	0.17s	0.082s	0.042s
CTT/GAD speed ratio	-	-	11	19	-

5.8   Conclusion

In this work we have demonstrated a novel technique to determine the location of multiple high velocity impacts (~300m/s) on fiber glass composite panels with embedded piezoelectric sensors. Two techniques were compared, a classical triangulation (CT) technique and a novel technique based on angle detection with groups of sensors (the so called the group angle detection method or GAD technique).   The GAD technique calculates the direction to the impact using the difference of time of arrival of the impact waves between pairs of sensors within the group. For the GAD technique, four sensor configurations where used including (1) two L shaped groups, (2) two sensor groups with each group consisting of three sensors closely spaced in a line, (3) a line of uniformly spaced sensors, and (4) three sensor groups with a pair in each. Since the spacing between pairs of sensors determined the resolution in wave time of arrival, for the same average distance between sensors inside a group, the L configuration gives the best relative impact location accuracy.

One issue with a linear distribution of sensors (i.e. panels P2 to P4) is that GAD technique always gives a pair of solutions – one on the positive side of the line and one on the negative

side. Since these solutions are equally weighted, this naturally introduces an error into the calculation.   However in the L shaped sensor group, the asymmetry in the sensor topology breaks this solution symmetry. In the specific case of the panels used in our research, this does not present a major issue since the solutions on the negative side of the line can be discarded; this might not be the case in a more general sensor/panel configuration.

Manufacturing of a panel with embedded sensors using the GAD technique presents some advantages as compared to the CT technique. Electrical cable routing is easier in the GAD technique since the cables are naturally grouped as opposed to being spread throughout the panel for the CT technique. Embedded cabling should be minimized in general since it increases the difficultly of mounting of the components, complicates panel manufacture and could have an impact on the overall structural integrity of the panel. On the other hand, the GAD technique allows a more concentrated distribution of sensors thereby simplifying cable routing and could even allow the use of prebuilt sensor arrays as proposed by Lin and Chang (2002) to greatly simplify the manufacture process.

A major source of error in locating the position of impact arises from the error in estimating the time of arrival (TOA) of the impact wave at the sensor location. For the CT technique, an error analysis shows that a relatively small error in impact location can be expected from a TOA error if the impact is confined to lie within an area circumscribed by the sensors. For the GAD technique however, there is as an intrinsic location error that comes from the multiple possible orientation that give the same difference of TOA in Equation (5.2). This error source could be reduced or eliminated by adding more sensors to the sensors groups, thereby allowing the time of arrivals that produce multiple solutions to be discarded. A similar error associated with multiple

isotemporal curves appears in the CT technique when the position of impact is outside the sensors array.

Increasing the number of sensors in each group will statistically improve the accuracy of the GAD technique at the expense of computational (and manufacturing) cost. A further study is needed to determine the trade-off between the number of sensors and the required impact location accuracy. Furthermore, a method of discriminating the high-error angles in the GAD technique could improve the position location but would generally require more sensor pairs.

Computational cost of the GAD technique was shown to be approximately an order of magnitude faster than the CT technique. This is due largely to the expense of conducting a two dimensional search for the CT technique. Both the CT and GAD technique speeds scale linearly with the number of sensor pairs and thus increasing the number of sensor pairs is a viable computational option if increased accuracy is required.

Classical triangulation was proven to be a robust technique that suffered no significant loss of accuracy by the effect of previous shots in the panel. The average experimentally measured error in the impact position was 16.8mm for the CT technique for all panels (panel P5 is not taken into account in this calculation since the impacts were outside the optimal sensor area for the CT technique). For the GAD technique the L-shape distribution gave the best relative error of 19.9mm. It should be noted that for the speeds used in these high speed impacts, the overall diameter of the delamination damage was visually measured to be approximately 25mm. An error of 20mm is thus most probably accurate enough for real-time assessment of impact location since further (and more detailed) inspection of the impact zone would be performed during repair of the component part.

Note that since these techniques use the arrival of the first wave reflections from the side of the panel have no effect; in a similar way, reflections and the changes in material properties from the previous impacts have little effect on this technique. Since the boundaries are free, the reflected wave will have an opposite sign to the wave travelling directly to the sensors.

6   Passive detection of high speed impact damage - extent

6.1   About Impact wave propagation

Complete understanding of high speed impact wave generation and propagation in solids does not exist at the moment. This work explores an experimental technique that can be used for structural health monitoring after high speed impact events but does not necessarily address the underlying physics of wave propagation from these complex events.

A single yarn/fiber subjected to an impulse will allow for the propagation of two waves: a longitudinal wave which is faster and a transverse wave which is slower (Taylor, 1942). These waves have been experimentally measured using high speed photography. This early observation was generalized to panels by Morye et al. (2000). The model presented in that paper assumed the propagation of the same two waves and predicted the shape and general dimensions of the impact cone which was then experimentally shown using high speed photography. Morye et al. (2000), Naik (2004) and Mamivand (2010) used a multilayer approach to solve the same problem, and proposed an energetic model for calculating V50, based on the formation of a cone due to the transverse wave generated by the penetration of the projectile. Of interest in these models for the present work is that they show the importance of wave propagation on the penetration process. The presence of that cone generated from those waves can be corroborated as experimentally shown in Figure 6.1.

The exact nature and shape of the generated wave is influenced by many factors, will be projectile and target material dependent, and will be influenced by the speed and angle of the impact. During and after the impact, a wave is generated at the impact position, which then propagates through the panel to the sensors. As an example, Parga-Landa (1999) calculated the

response of a panel subjected to a triangular stress pulse and showed that different waves would be generated simultaneously including: primary P waves, secondary (or shear S) waves, as well as Rayleigh and Lamb waves. The P and S wave that do not contribute to the Lamb waves will be absorbed in short distance (since they do not satisfy the plate boundary conditions) and only guided Lamb waves will survive far from the impact position. Lamb waves are dispersive in nature, so waves received at different distances from the impact position will have dissimilar shapes in the time domain. The impact will generate a series of complex waves within the plate though the shape of the damage cone will mean that the anti-symmetric modes are likely to be dominant, with some smaller contribution from the faster symmetric modes. After the impact cone has been fully developed, a lower frequency shear plate wave (which is one special type of anti-symmetric Lamb wave of long wave length compared with the thickness) is then generated. We propose to use the characteristics of the first (high frequency) wave to estimate the extent of damage within the composite material. Some assumptions about the wave have been made in this work:

- The wave generated will have amplitude proportional to the projectile speed
- The impact location is sufficiently far away that only Lamb waves are present at the sensor location
- The Lamb wave with the highest amplitude corresponds to the A0 Lamb wave
- The Lamb waves attenuate with distance from the impact location.
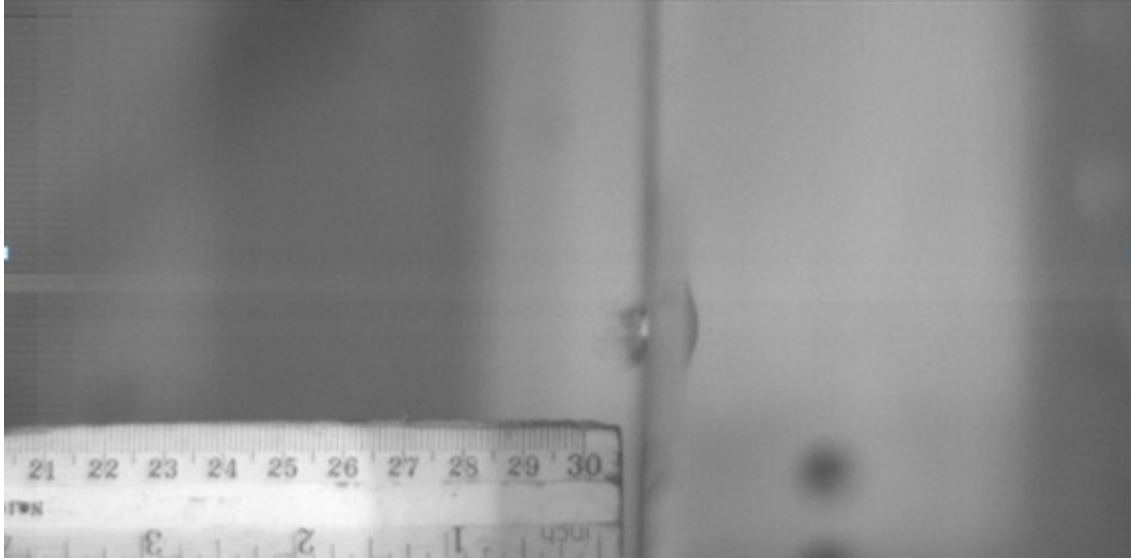
Figure 6.1 Impact of a FSP projectile, the cone formation at the back of the panel can be clearly seen. Camera acquisition rate was 44K frames per second.

6.1.1   Wave propagation

The wave generated by the initial impact is in general very complex and will potentially consist of a large number of different modes. The technique proposed in this research will use the arrival of the first (high frequency) wave to estimate the extent of damage within the composite material.

6.1.2   Wave absorption due to distance and angle

Since the waves are generated from the epicenter of the impact and then move in a radial direction, in order to assure the conservation of the energy, the signal will be attenuated with distance. At the same time, the material will dampen the propagated wave. This effect as been documented in detail by Maznev (2003), Torres-Arrondo (2010) and other sources as mention in the state on of the art chapter (Chapter 1). In this work a damage parameter that correlates sensor measurements with damage will be developed. In order to compare measurements from sensors

at different angles and distances, a correction factor has to be establish to take into account wave dispersion and attenuation. The main thrust of this research effort is to develop an approximate absorption function and to experimentally validate this function.

The following equation will be proposed as the attenuation function; (a rigorous justification to this equation is beyond the scope of this work)

$$A_2(\theta, r) = \frac{a_2}{\sqrt{r}} f(\theta) e^{-\alpha r} \qquad (6\text{-}1)$$

According to Maznev (2003), the calculation for far field and superficial waves in anisotropic media yields that same $1/\sqrt{r}$ dependence but also includes a rather complicated angular dependence term. An exponential decay typical in damping problems has been added to this part. Note that in general the exponent and angular function will also be dependent on the wave frequency. In order to reduce the complexity of the wave attenuation function, it is possible to filter the signal at a single frequency.

Note that in equation 6-1 it is assumed that the sensor are far from the impact position, in practice this requirement does not pose a significant problem since in a real application, three groups of sensors is typically required; thus if an impact occurs near one of the sensor groups, those values would be discarded.

6.2 Experimental methods

The panels where manufacture by vacuum infusion using fiber glass fabric and an epoxy matrix (S2-6187 - HEXCEL, EPON 828 - MOMENTIVE) with a $[0/90]_{10s}$ layout. The dimensions of the panels are 12×12×1/4". The panels had 1/4×0.0075" circular lead-zirconate-titanate (PZT) piezoelectric sensors embedded under the first ply following the same procedure as outlined in Chapter 3. Sensors where placed in the four corners of the panels and another 4 sensors where

placed in the two lower corners to form an L shape. (The L shape sensor grouping provided the best result in the group angle location detection method as described in Chapter 4 and were thus used for the tests in this chapter). A sensor was place for each corner to be able to make comparative measurements using the CT location technique, but due to time constrains these calculations were not performed. A scheme of this panel's configuration is shown on Figure 4.10 (a).

A .223 (5.56mm) FSP projectile was used for this study. The weight of the projectile was 1.1g as indicated by the associated standard (STANAG 2920). A picture of the projectile can be seen on Figure 6.2. A gas gun was used to achieve the desired speed of the projectiles as shown in Figure 6.3. The gun uses either compressed air of helium as the propellant and is triggered using an electro-valve; the initial position of the projectile within the barrel and the pressure of the compressed gas then allows for control of impact speed.

A pair of photoelectric sensors and laser diodes are used to measure the speed of the projectile at the muzzle. The Photoelectric sensors and the sensors embedded within the panel are connected to a data acquisition system running Labview® (National Instruments PXI-e 1062Q with 2 simultaneous sampling DAQ and an acquisition rate of 4Ms/s).The acquisition system also sends the triggering signal to the computer that controls the digital camera (PCC station on the figure) to acquire the high speed video of the impact. With helium and using a FSP projectile, a maximum speed of approximately 600m/s was achieved by this system.

Figure 6.2 FSP projectile
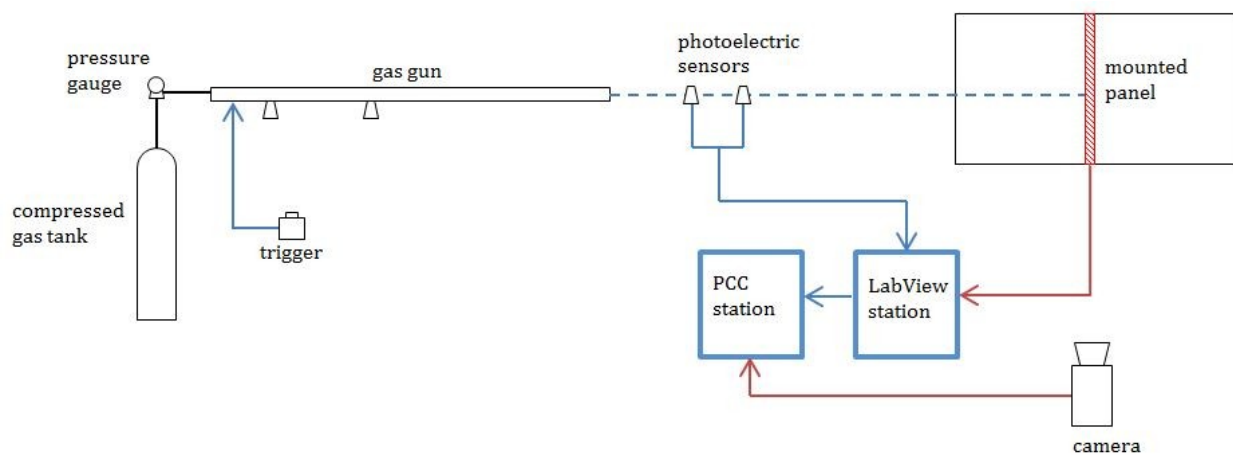
Figure 6.3 Setup schematic for high speed impact testing.

Incident projectile speed was measured using two laser diodes at a known distance along the trajectory of the projectile near the exit of the barrel. The speed of the projectile was also measured as it impacted the panel using a high speed camera (IMACON 200). Acquisition rate was set at 49k images/second. A ruler in the incident plane of the projectile was used to calibrate

the digital images. Projectile speed was calculated using the calculated change in position of the projectiles between successive images. An example of the speed measurement procedure can be seen on Figure 6.4 where two successive digital images are shown. The left images are the actual high speed camera photographs while in the right images are the digitally filtered improved contrast grey. Projectile orientation was also measured to verify the normal alignment of the incident projectile with the plate. Once the images were converted to black and white, both alignment and position of the projectile centroid was measured for each camera frame, using standard image processing techniques.
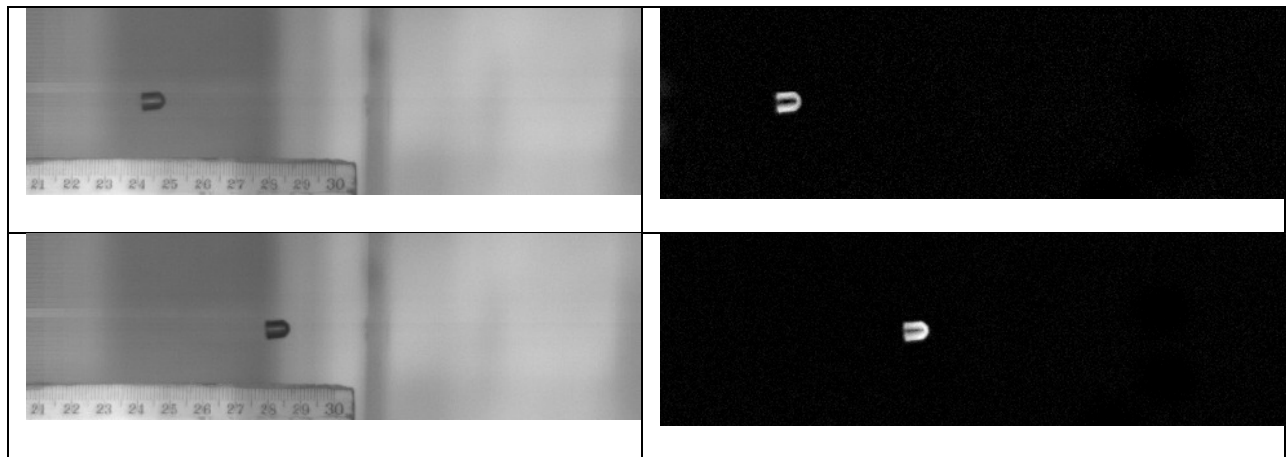
Figure 6.4 High speed video measurement images of two successive frames are shown on the left and the same digitally filtered high contrast grey images used to calculate the speed of the projectile are shown on the right.

Comparing the projectile speeds from the photoelectric sensors and the camera (Figure 6.5), it can be seen that the photoelectric sensors measure slightly lower speed when the projectile speed is under the speed of the sound and slightly higher speeds in the opposite case. In the case of projectiles traveling above the speed of sound, the small reduction of speed measured by the two methods could be explained by the effect of air friction.

The incident speeds of the projectiles compared with residual speed can be seen on Figure 6.6, for non-penetrating impacts (labeled np) most of these impacts bounce back after hitting the panel and therefore the residual speed is negative.
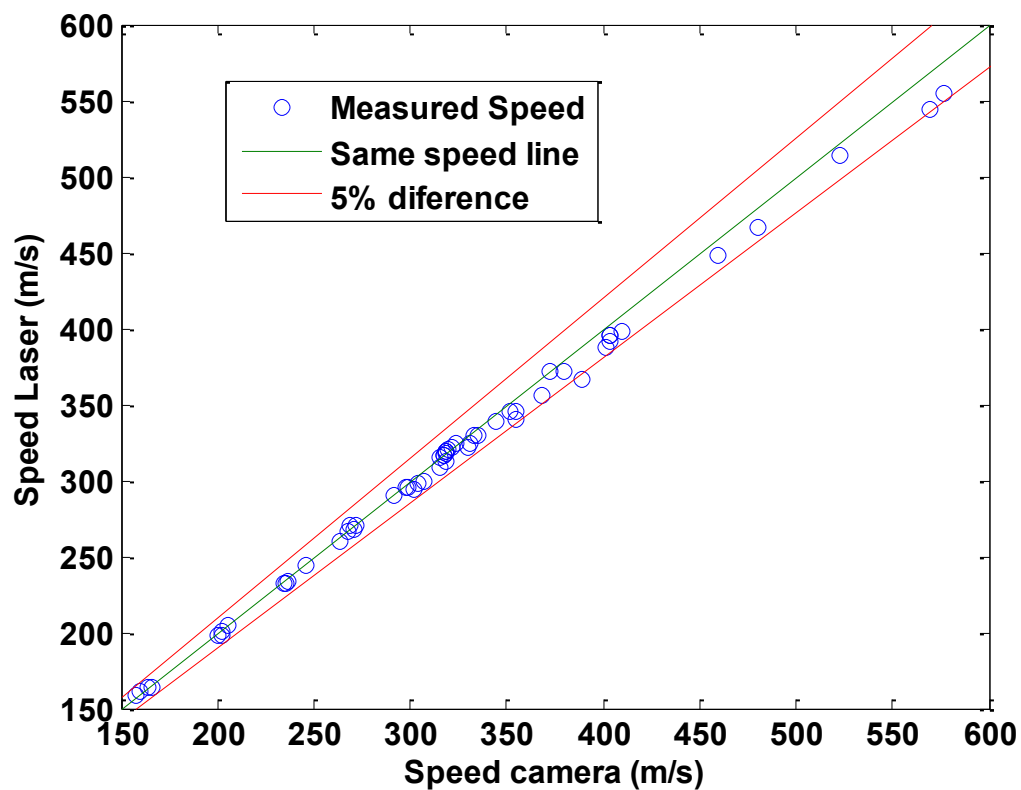
Figure 6.5 Comparison between measured projectile speeds using the high speed camera method and using two closely spaced lasers at the bore end.
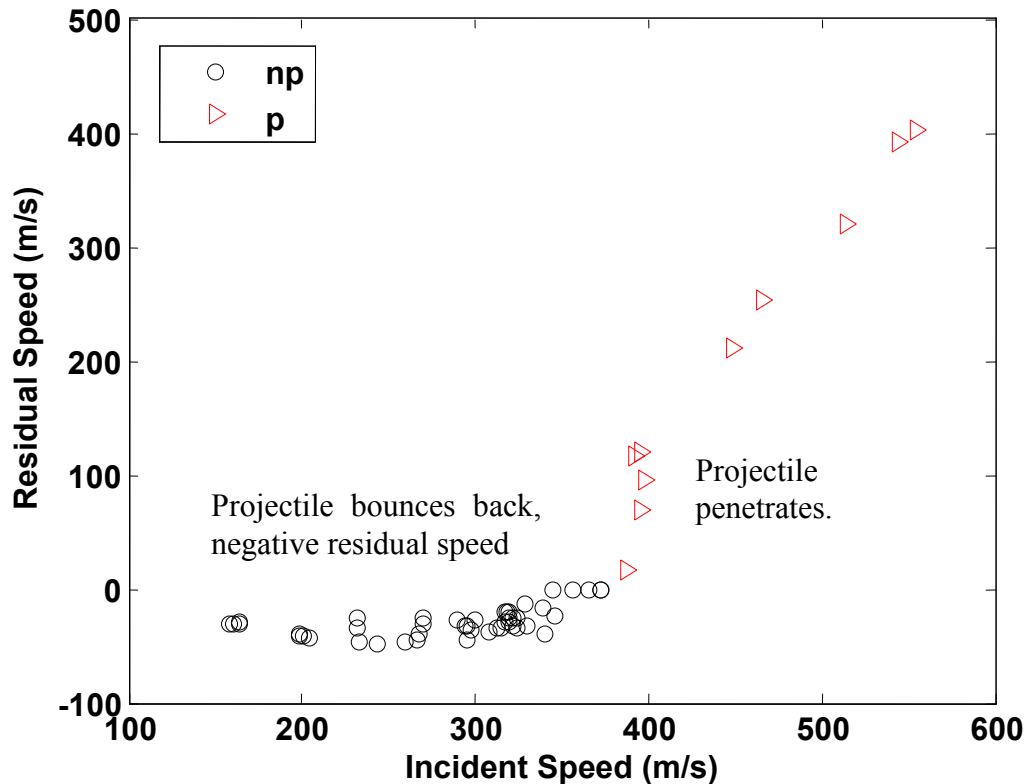
Figure 6.6 Experimentally measured relationship between the incident speed and residual speed of the projectile after impact with the panel.

6.3   Delamination Area Measurement

When a projectile with a certain critical energy impacts a panel, permanent damage primarily in the form of delamination damage will appear in the material. The size of the damage will in general be greater as impact energy increases, while the damage mode does not change. From the point of view of the SHM, it is important to be able to measure the extent of this damage and assess to what degree this damage reduces the component's properties such as strength and stiffness. In the particular case of damage caused by a high speed impact, the size of the delamination area could be one of the critical parameters that will define if the panel has to be

repaired or replaced. In a laboratory setting there are a number of techniques that can be used to measure delamination area, two of these methods include: (1) cutting through the impact site to measure the crack length and (2) performing an ultrasonic C-Scan of the impact location. The first technique is more accurate, provided that the cut has been carefully made in the correct location and has not introduced any further damage. The second ultrasonic technique however can measure the damage area as opposed to only the damage diameter in the cutting method. Both techniques are extremely time consuming and in the case of the first technique destructive. Another approach was used in the course of this work. Since the composite material used throughout this work is translucent, an alternative technique based on digital photography was developed. In this technique, a diffusive light source located behind the panel is used to illuminate the damaged areas. A mechanical rig is used to position the digital camera perpendicular to the panel with its focal plane parallel to the component. Figure 6.9 shows the photographs taken for each of the panels used in this study; the damage areas from multiple impacts are clearly visible in all of these panels. A custom written MATLAB® code was implemented to automatically measure the area of the impacts; (note that this is a similar code to any other scanning technique used to measure damage area such as ultrasonic for ultrasonic C-Scanning). Figure 6.7 show the calculation procedures: (1) the image is first cropped to include only the damage area and then transformed to grey scale (Figure 6.7 frame1), (2) using a simple grey-scale threshold, the image is filtered so that the undamaged areas are rendered white while the damaged areas are unmodified (Figure 6.7 frame 2), (3) the image is then inverted (Figure 6.7 frame 3), and (4) transformed to black and white (Figure 6.7 frame 4). Using standard MATLAB® image processing routines, white areas smaller that a preset image noise size are then deleted. The areas of the remaining white regions are then measured in square pixels and the

UNCLASSIFIED

location of their centroid is calculated. A second image processing iteration is then done refining the results for individual impacts, greatly improving the precision of the method (Figure 6.8). In order to compare photography taken from different panels the light intensity was selected to have the same light on the non delaminated surface. Diffused white light was used for this measurement.
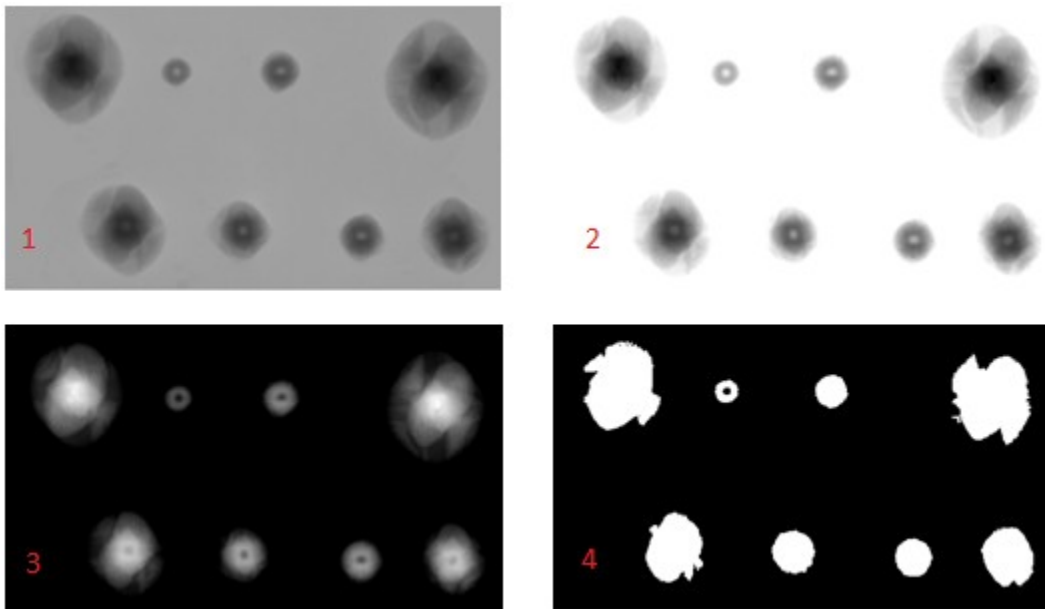
Figure 6.7 The digital image processing used to calculate damage area.

Figure 6.8 Second iteration on the area calculation for shot 4 panel SP14.

To validate the optical technique, some ultrasonic C-Scan measurements of the panels were also performed (UltraPAC UPK-11/b, from Mistras group, UT Ultrasonic-Solutions). The C-Scan of the damage area in panel SP14 can be seen on Figure 6.10. In order to be able to obtain a C-Scan image with appropriate resolution of the damage areas typically requires careful alignment of the panel with respect to the ultrasonic transducer, each scan then takes more than 14 hours. To measure all the panels would require several weeks of work and that is the reason behind the development of the much faster optical based technique.
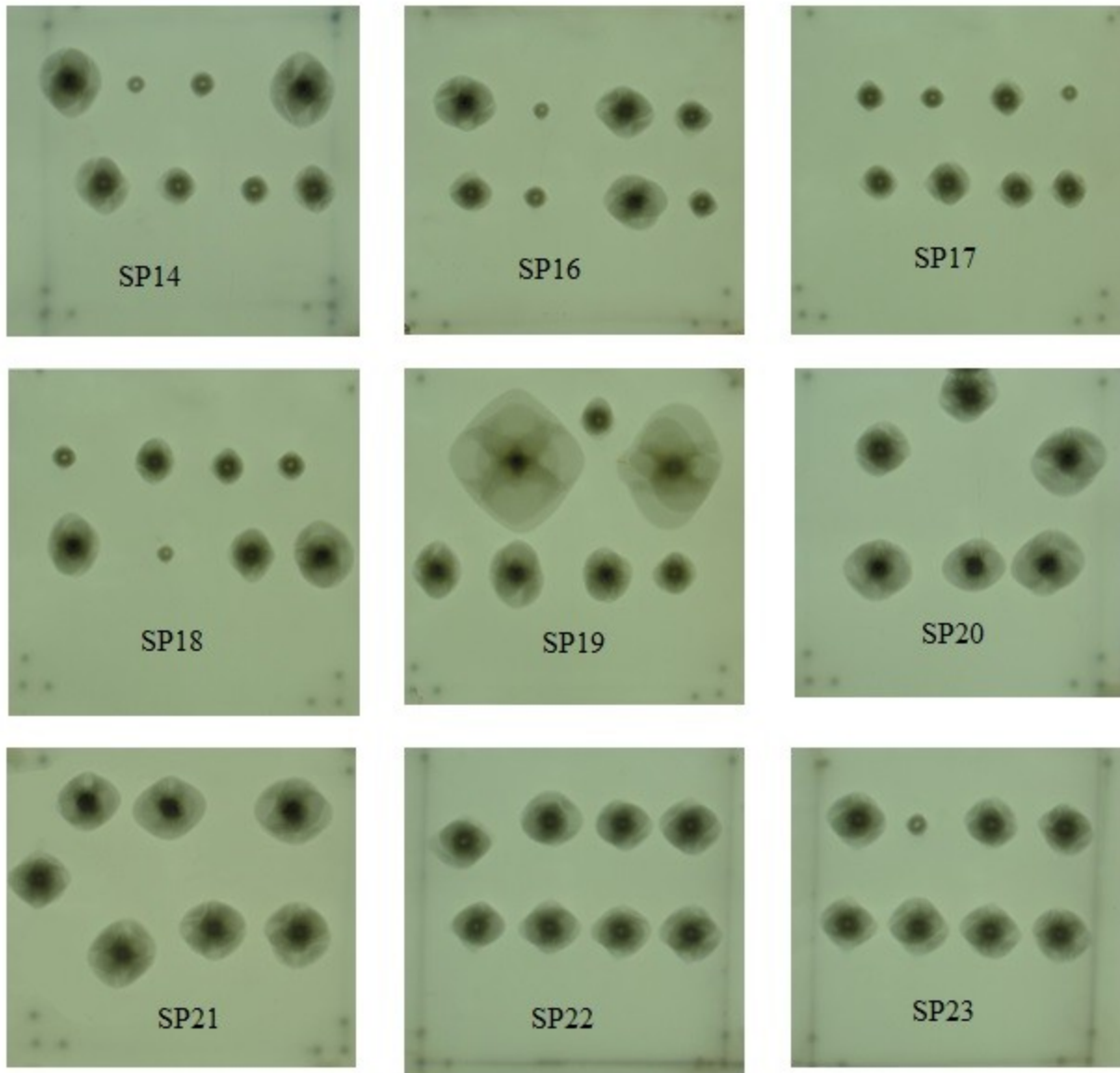
Figure 6.9 Photographic images of the translucent damaged panels using a diffusive light source.
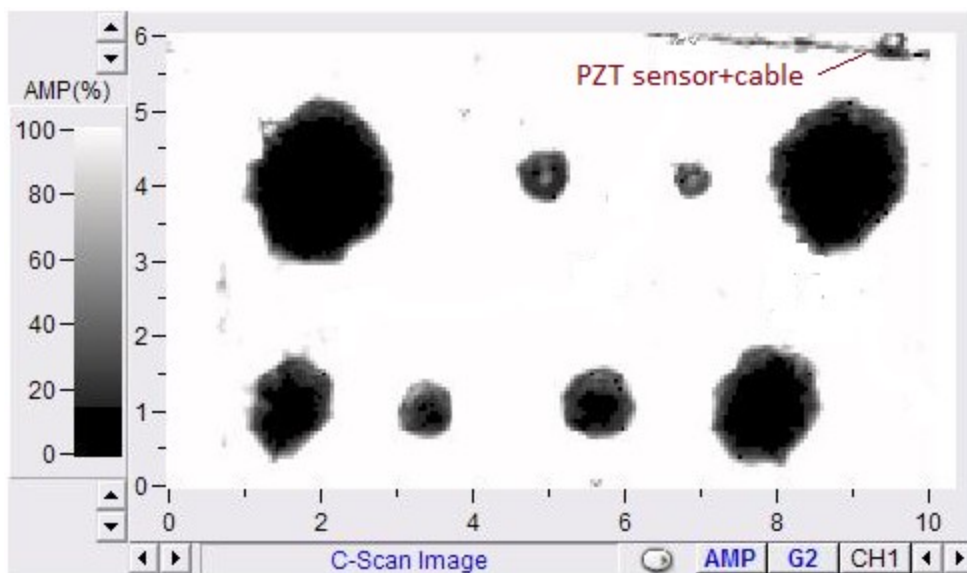
Figure 6.10 Ultrasonic C-Scan image of panel SP14 clearly showing multiple impact damage locations. One of the sensors can be seen in the top right of the figure. (Note that the horizontal axis is inverted compared with the corresponding image in Figure 6.9)
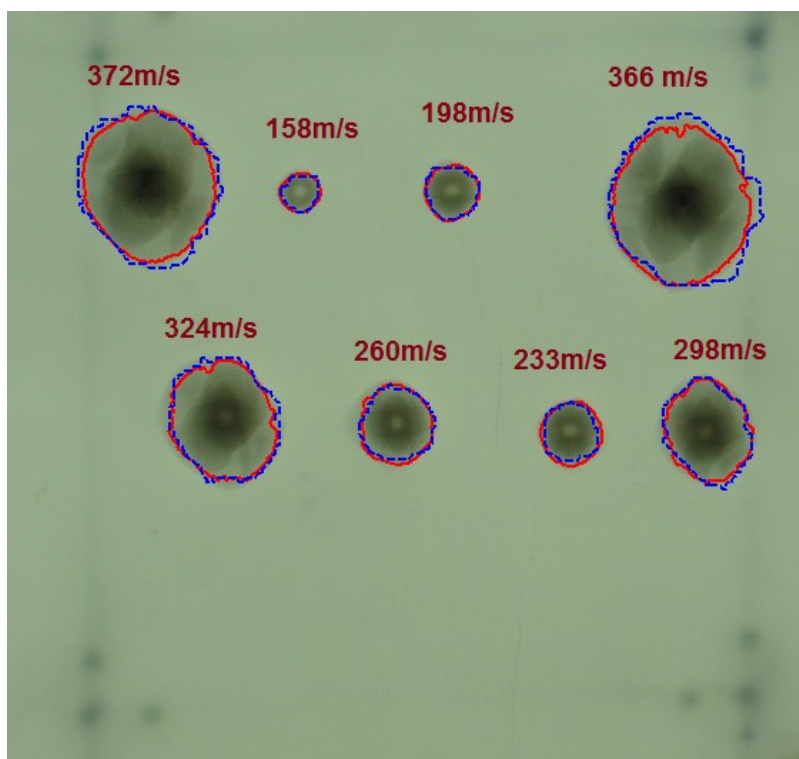
Figure 6.11 The boundaries of the damage areas calculated by the optical technique (solid red line) and for the ultrasonic technique (dashed blue line) for panel SP14.

The same MATLAB® code for area measurement was used for both the C-scan and optical method. The damage areas measured by the two techniques for panel SP14 as seen in Figure 6.11 shows a good agreement. The results from the optical method appear to show a slightly larger damage area than the ultrasonic method for an impact speed range below 300m/s while the opposite is true for impact speeds greater than 300m/s. Figure 6.12 further illustrates this point by directly comparing the damage areas calculated by the two methods. Since these two methods provide essentially the same results, for the purpose of this research the optical method was deemed to be accurate enough to estimate the delamination area.
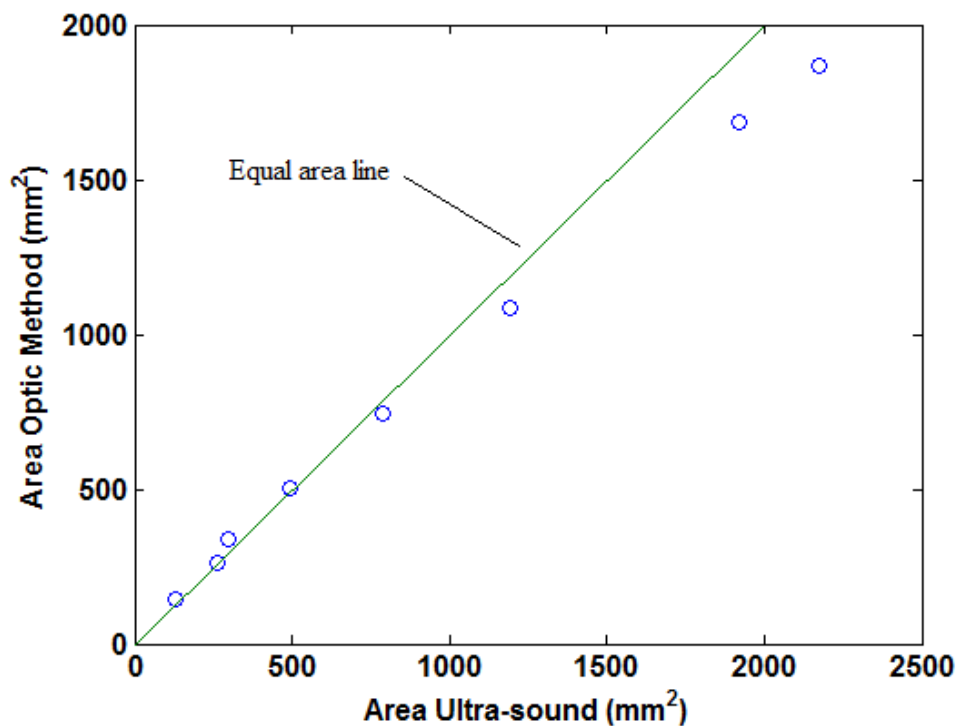
Figure 6.12 Comparison of the damage area of each impact calculated from the ultrasonic C-Scan and from the optical method.

6.4   Energy and Damage area Relationship

Previously Morye (2000), Naik (2004) and Mavivan (2010) have developed models to predict the absorbed energy associated with different damaged mechanism during high speed impact. The main damage mechanisms identified from their work are: (a) fiber fracture under tension, (b) delamination, and (c) shear plugging. In general the greater the energy absorbed by the material the larger the expected damage area. At speeds over the V50 of the material, a drop in absorbed impact energy is expected according to these models since the total length of strained fiber will be reduced (due to a smaller penetration cone which is created before fracture). The speed of the projectile before and after impact was used to calculate the absorbed energy:

$$E_A = \frac{1}{2}m(v_0^2 - v_R^2)$$

The results for absorbed energy for all the impacts is shown in Figure 6.13. Note that since there is no guaranty that the trajectory of the projectile after the impact is in the camera's focal plane, there could be an error in the measurement of the remnant speed intrinsic to the speed measuring technique. The error is relatively small in the case of a penetrating projectile since the witness plate located behind the panel allows for the measurements of the flight angle and to correct the speed. In this way, the angle error is only applicable to the non-penetrating impacts where most of the energy is absorbed by the panels. Note that for the non-penetrating impacts, the projectile bounces back with a relatively small velocity compared with initial speed and therefore the angle error is expected to be relatively small.
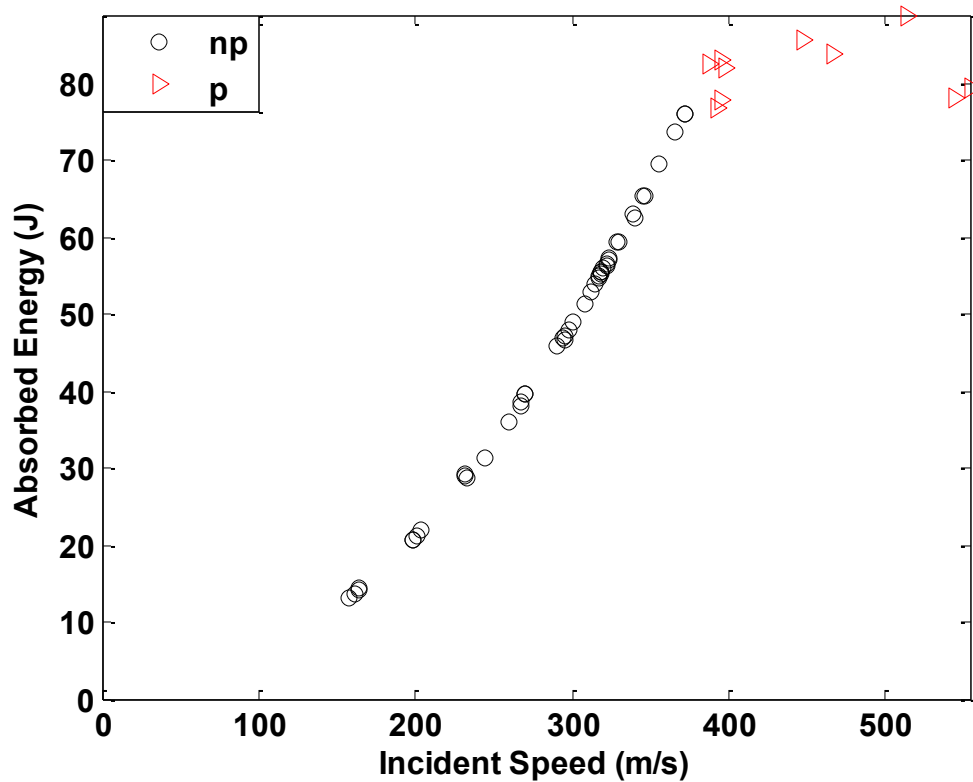
Figure 6.13 Relationship between the energy absorbed by the panel and the incident projectile speed. Here again **np** represent non penetrating impacts, while **p** are penetrating impacts.

Figure 6.14 shows the relation between absorbed energy and delamination area and initial speed against delamination area. It appears as if there was a small reduction in delamination area above the V50 speed. This effect however is relatively small compared with the experimental scatter at these speeds and more tests should be performed to properly address this effect. Since this effect is relatively minor in the context of the present research, extra test were not carried out.
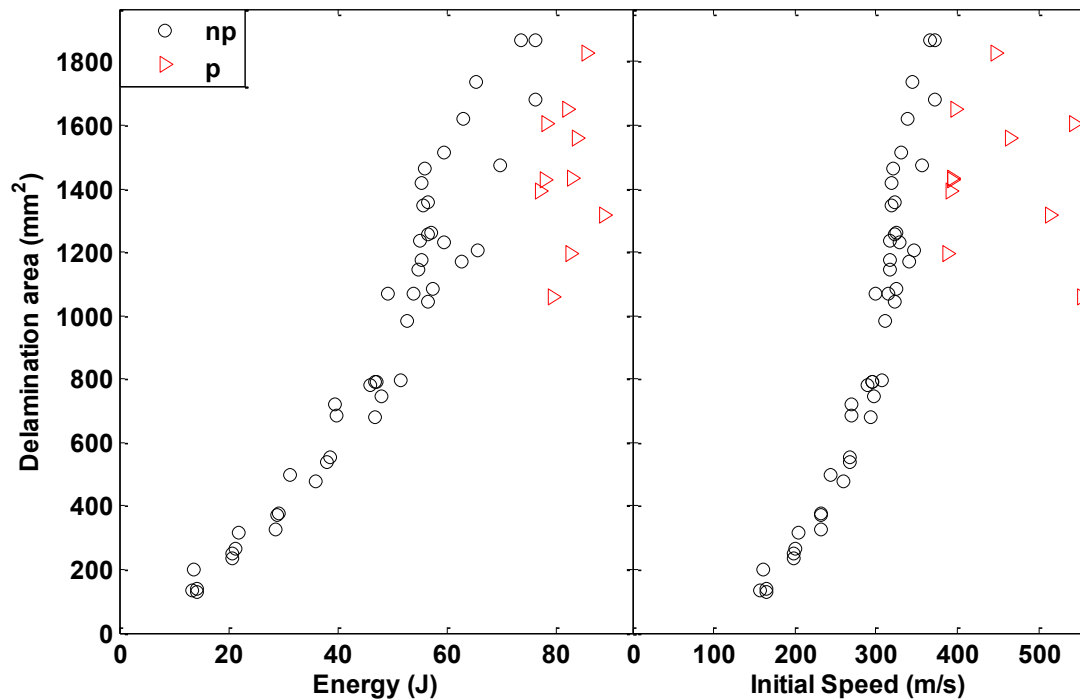
Figure 6.14 Delamination area plotted against both absorbed energy and initial speed. The **p** label indicates penetration of the panel by the projectile and **np** denotes that the projectile did not penetrate the panel.

The relationship between absorbed energy and initial projectile speed is shown in Figure 6.13. The energetic models mentioned above predict a small drop in the energy absorbed at speeds higher than V50. This effect is however not seen in Figure 6.13 where the absorbed energy increases rapidly up to V50 but does not seem to fall at speeds above V50. (Once again this effect could be due to experimental scatter but does not significantly affect the results in this chapter).

6.5 Damage parameter development

Due to the position of the sensors, the impact event can occur at different angles and distances from the sensors. This in turn will affect the amplitude of the measured waves at the sensor due to the absorption within the material. In this section we present methods to estimate the effect of wave absorption due to both distances and angles from the impact to the sensors.

6.5.1 Measurement of the wave absorption function

The panel shown in Figure 6.15 was manufactured to measure both the speed of sound with angle and to measure the effect of the angle on wave absorption. A wave pulse was sent from the PZT sensor in the left lower corner and was measured by the 13 PZT sensors located on the quarter circle at 6.9 degrees divisions. The magnitude of the measured signal normalized with the 0^0 angle orientation can be seen in Figure 6.16 for two transmission frequencies, i.e. 100KHz and 460KHz. The angular part of the wave absorption is higher at the center at higher frequencies as can be seen in Figure 6.16 the absorption approximately follows a quadratic relationship with propagation angle though the underlying physics is as yet not well understood. Wu and Chiu (1991) obtained a similar angle-absorption relationship for a unidirectional composite material. In the unidirectional case there is however only one plane of symmetry compared with the 2 perpendicular planes of symmetry on present case.

As previously mentioned, absorptions is in general frequency dependent. In the present study all the calculations have been performed assuming a wave frequency of 100KHz as was measured by a frequency decomposition of the sensor signals. In some impacts there were a number of other characteristic higer frequencies; However since these higher frequencies could be attenuated for various impact distances and angles, they were not used in the present study.
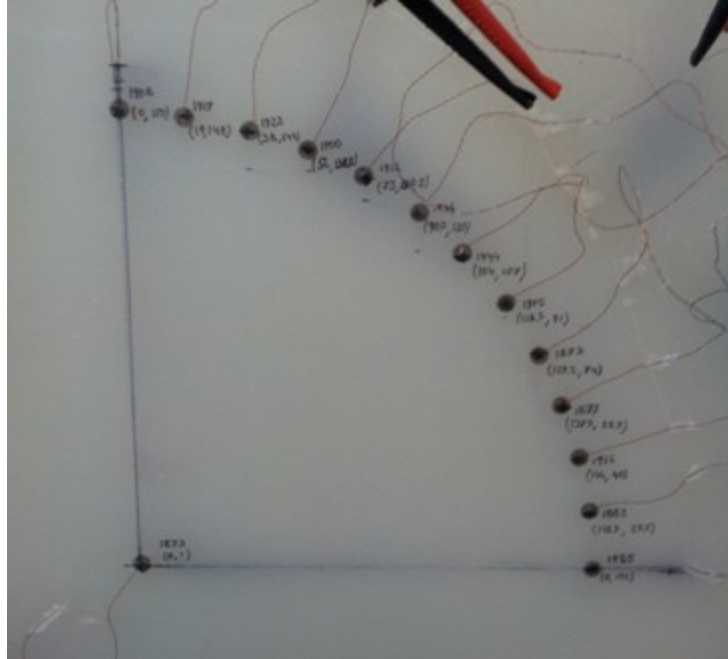
Figure 6.15 Panel with embedded sensors used to measure both the speed of sound and absorption as a function of propagation angle.

Once the angle component of Equation 6.1 is known, the contribution of the radial part can be calculated. In order to make this measurement another panel was manufactured, as can be seen on the right side of Figure 6.17. In this figure, ultrasonic pulses are sent from the center of the panel and measured in the sensors surrounding them. Relative amplitude can be then be calculated with respect to the closest sensor. Using Equation 6.1, the data was then fitted using a least square approach giving the exponent term as 0.0044mm^{-1} (radial distances given in mm) for the 100KHz signal and 0.01 for the 350KHz signal. This means that absorption grows with frequency. This was an expected result from bibliography since is a result obtained by all sources.
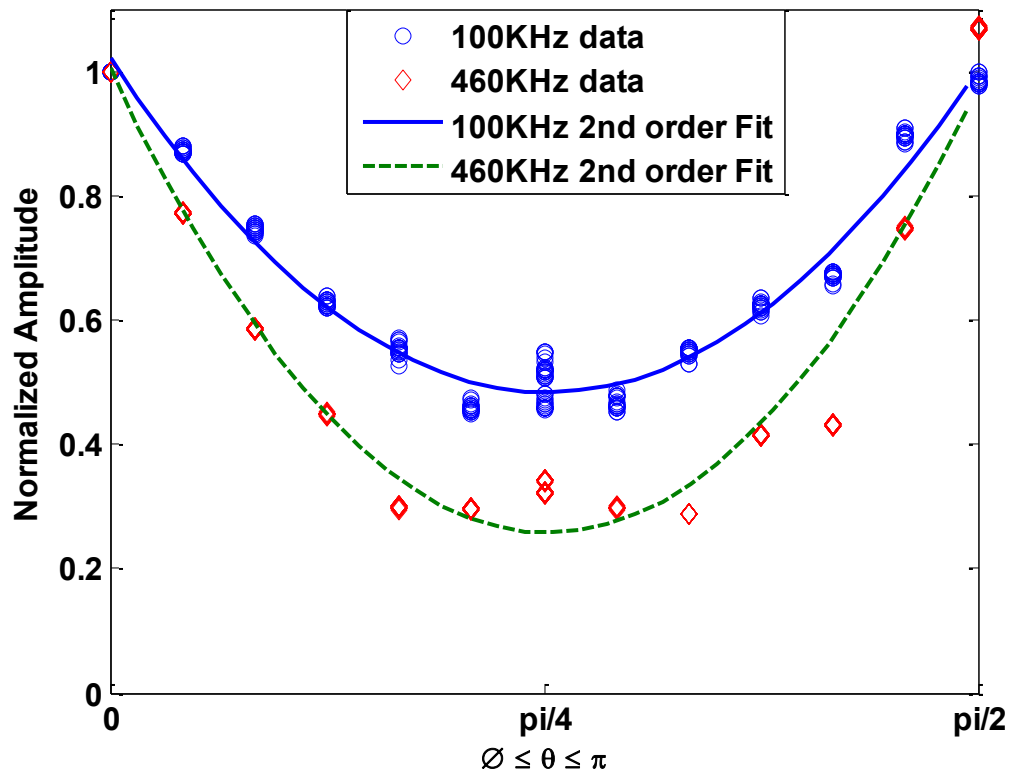
Figure 6.16 Attenuation of wave amplitude for different angles and frequencies.
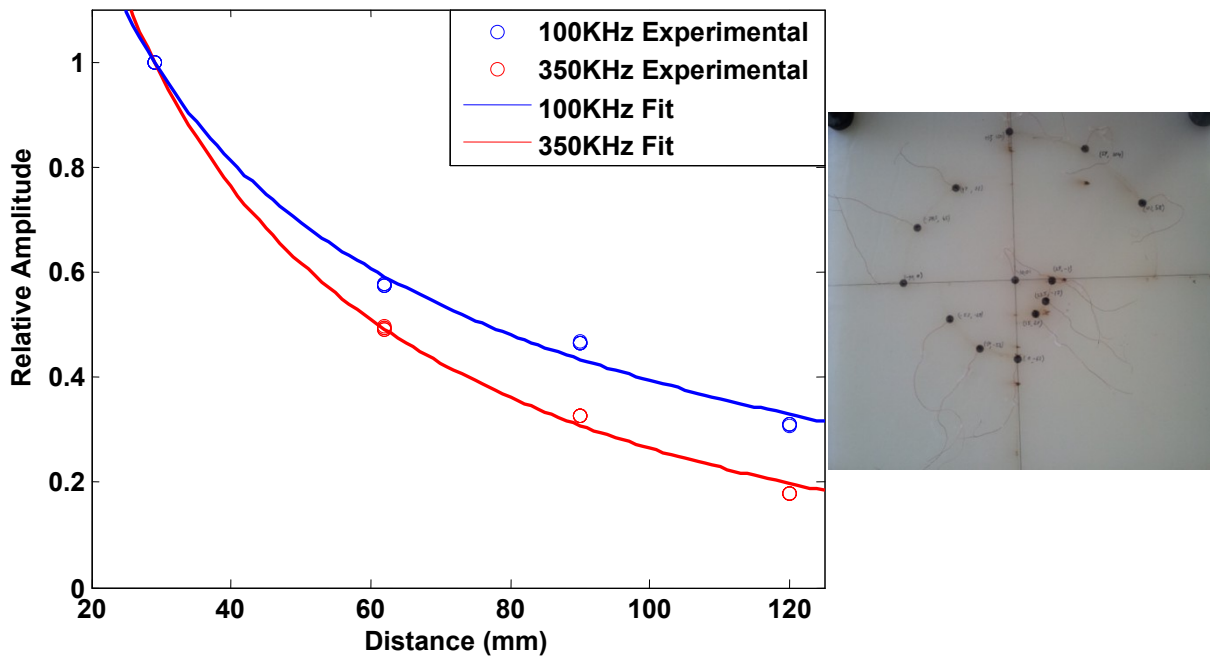
Figure 6.17 Plot of the absorption calculated for the 0 and 90 degrees direction in the panel shown on the right. The circles are the experimentally measurement results while the curves are the exponentially fitted curve given by Equation 6.1. There are 20 experimental results per distance. The exponential constant is 0.01 for the 350KHz and 0.0044 for 100KHz, therefore absorption grows with frequency.

6.5.2   Damage parameter definition

As the propagating wave arrives at the embedded PZT sensor, a voltage proportional to the strain in the PZT is generated. Measuring this voltage will provide information of the elastic energy stored on the composite due to the propagating wave. The following procedure to calculate the damage parameter is proposed. The Hilbert transformation of the measured signal is calculated and with it the analytic function. With the analytic functions the envelope of the incoming signal was first calculated (see for example Feldman 2011).

$$h_v(t) = \mathcal{H}\big(V(t)\big) = -1/\pi \lim_{\epsilon \to 0} \int_\epsilon^\infty \frac{V(t+\tau) - V(t-\tau)}{\tau} d\tau \qquad (6\text{-}2)$$

$$a_v(t) = V(t) + ih_v(t) \qquad (6\text{-}3)$$

$$E_{nv}(t) = |a_v(t)| \qquad (6\text{-}4)$$

Where $\mathcal{H}$ represents the Hilbert transform, $h_v(t)$ is the Hilbert transform of the voltage function $V(t)$, $a_v(t)$ is the analytic function of the signal and $E_{nv}(t)$ is the envelope of the function $V(t)$. A signal parameter is then defined as:

$$SP = \int_{t_0}^{t_1} E_{nv}(t)^2 dt \qquad (6\text{-}5)$$

For digital signals this integral can be expressed as:

$$SP = \sum_{k_0 = t_0 * rate}^{k_1 = t_1 * rate} \frac{E_{nv}(k)^2}{rate^2} \qquad (6\text{-}6)$$

Where *rate* is the sampling rate and $E_{nv}(k)$ is the value of the envelope at sample k. The integration time is a critical parameter and will be discussed in detail in the following section.

The signal parameter SP is then corrected for propagation distance and angle by Equation 6.1 to give the damage parameter (DP):

$$DP = \frac{SP}{\left(\frac{c}{\sqrt{r}} f(\theta) e^{-cr}\right)^2} = \left(\sum_{k_0 = t_0 * rate}^{k_1 = t_1 * rate} E_{nv}(k)^2\right) \frac{r \, e^{2cr}}{f(\theta)^2} \qquad (6\text{-}7)$$

Since the magnitude of DP is arbitrary, all constants (i.e. acquisition rate and the constant coefficient in Equation 6.7 have been set to unity. Note that this damage parameter has dimension of $V^2 t$ where V is the sensor voltage and t is time. For piezoelectric materials the

generated voltage is proportional to the average strain and thus the damage parameter *DP* is proportional to the strain energy between times t_0 and t_1. As previously mentioned this strain energy is in turn directly proportional to the impact energy.

6.5.3   Contact time estimation

As has been mentioned previously, high speed impact is wave dominated. As soon as the projectile first impacts the initially stationary panel's surface, a stress wave traveling through the thickness of the panel from the point if impact is generated. This process last approximately 2us (for the panel thickness and wave speed used in this thesis) after which the formation of the damage cone begins.

 The maximum impact force typically occurs before the impact cone has fully developed both for the case when the projectile has perforated the plate or it has been stopped by the plate as explained in Chapter 2. The formation of the impact cone can be considered to provide an initial displacement to the plate at the time of impact which in turn generates the structural waves within the plate. As previously mentioned, integrating the sensor signal over all time will then provide a measurement of the energy of the impact. Unfortunately this integrated measurement will also include reflected waves from the panel edges which in turn will be influenced by the boundary condition of the plate, absorption at the boundaries, sound radiation though air and transmission of the wave to the rest of the structure, not to mention any other sources of structural vibrations in the plate. Due to the boundary effects and in order to avoid long integration times, we propose to analyze only that part of the wave that arrives at the sensor before any boundary reflections. The major assumption in this work is that the integration of the initial stress wave arriving at the sensors is proportional to the impact energy and that the required integration time should be of the same order of magnitude or less than the time required

to reach the maximum impact force. Note that this first arriving wave amplitude will be small in comparison with the subsequent waves as predicted by the models of Morye (2000) Naik (2004) and Mavivan (2010). Knowledge of a characteristic time of contact is therefore needed in order to obtain an approximate integration time. Gower el al. (2008) measured back plate displacements against time for tests performed at lower speeds (<250m/s) and Kevlar composite panels. The maximum displacements in these tests was reached at approximately 300us, though the maximum force occurred approximately in half that time; thus approximately 150us can be considered as the upper limit for the wave integration. Another way of setting an upper limit can be determined from high speed camera measurements. Figure 6.18 shows cropped frames from the video showing the detail of the impact. It can be seen that the impact occurs between frames 3 and 4 and that the maximum displacement occurs between frames 4 and 6; this give an upper bound to the contact time of 60us. Following the same reasoning than found in Grower et al. (2008) a time of approximately 30us could be considered a reasonable upper limit to set for the integration time. Another important factor in order to choose a proper integration time is the maximum time occurs before the reflections from the sides of the panels arrive back to the sensors. Since the sensors are situated at least 25mm from the panel boundaries the time of flight of the structural waves should be greater than 12us. This calculation has been carried out using the maximum speed of sound measured in Chapter 4 that can be seen in Figure 4.2.
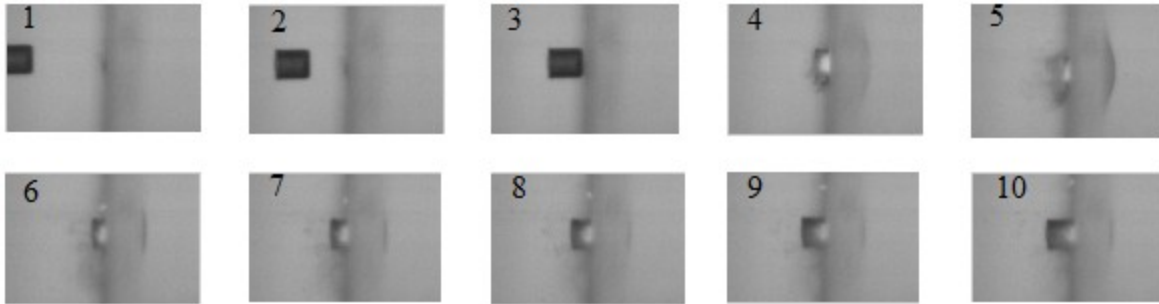
Figure 6.18 panel SP23 shot 8 example of time of contact measurement. The projectile in Frame 3 has not yet touched the panel. In frames 4 and 5 there is clear contact and in the frame 6 the projectile is bouncing back. From these images a time of contact off less than 60μs can be expected. Note the impact cone on the right side of the panel in frame 5. The frame rate is 49000 frames per second.

6.6   Data analysis

Once an upper integration time limit for the damage parameter calculation was established (see previous section) an empirical method was used to find an integration time that minimizes the dispersion of the DP as measured by each of the different sensors between all shots. After sweeping up to the upper limit (30us) an optimal value of 12.5us was selected. This time was also approximately the shortest possible reflection time. Note that the results of the calculations are not very sensitive to longer integration times (with the exception of impact positions and panels where the reflection can arrive within the longer integration window).   Shorter integrations times increase the dispersion between sensors from the same impact significantly. This can be understood looking at Figure 6.19. It shows the measurement of three of the 3 sensors in group 1 for the first four impacts on Panel SP14. Figure 6.19 clearly shows that that as the impact distances from the sensors increase, the signal arrives later and is smaller. This signal attenuation can be clearly seen when comparing impacts S1 to S4 where the impact speeds are approximately equivalent (~380m/s) but the distance for S4 is further and thus the signal

amplitude is significantly smaller. In all cases the waves arrive later to sensor 1 than for the other sensors due to its relative position to the impacts, and for the same reason the signal amplitude at sensor 1 is slightly smaller in amplitude. In every case the initial signal arriving at the sensors typically consists of a valley followed by a peak. After this initial time, the waves become more complicated and are not identical in all cases, but as seen in Figure 6.19 signal amplitude is smaller than the initial peak and therefore will not have a significant impact on the DP value. Again this justifies the use an integration time that includes these two features (i.e. minimum and maximum) but not to use the signal data after this initial time. Once more this implies the use of an integration window of approximately 10us.
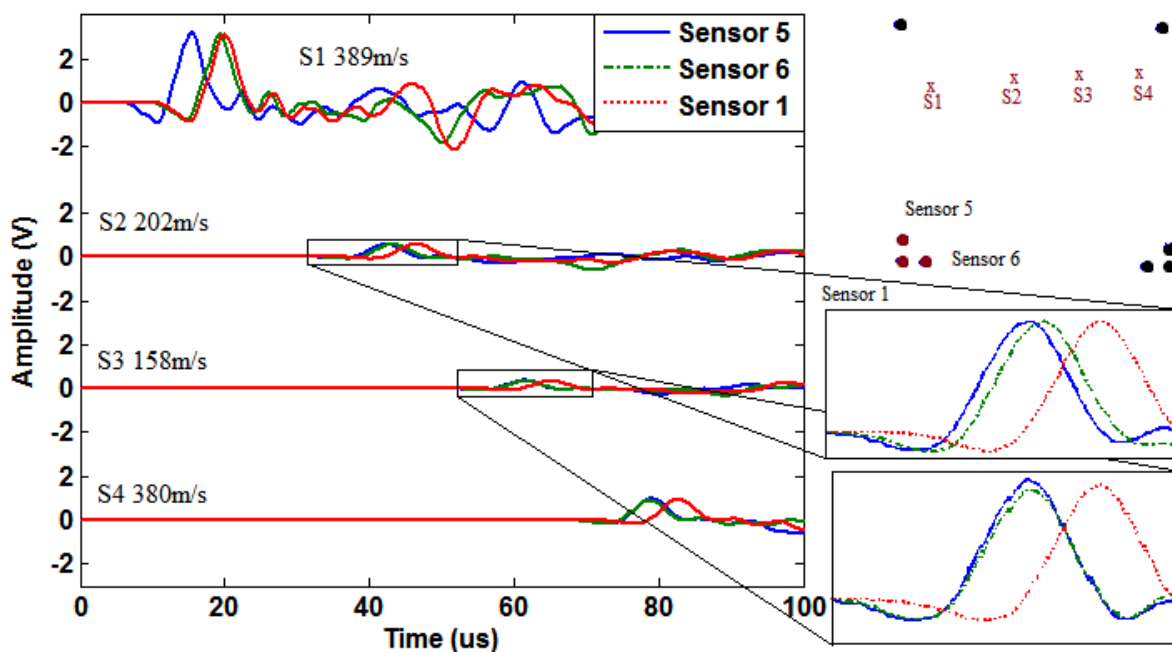
Figure 6.19 Waves measured at sensor group 1 for panel SP14. The signals in shots S2 and S3 have been magnify for detail conbinience.1.

Figure 6.20 show the same shots and sensors as in Figure 6.19 but corrected for both angle and distance attenuation. It can be immediately seen that the difference in amplitude from S2 and S3 has been reduced, and that the magnitude of the signal of impact S4 is approximately the same as for impact S1. Is interesting to mention that the signal of S1 has a faster rise time indicating the presence of higher frequency components which are no present in the other impact signal; again this could be explained by recalling that higher frequencies are absorbed over shorter distances than lower frequencies.
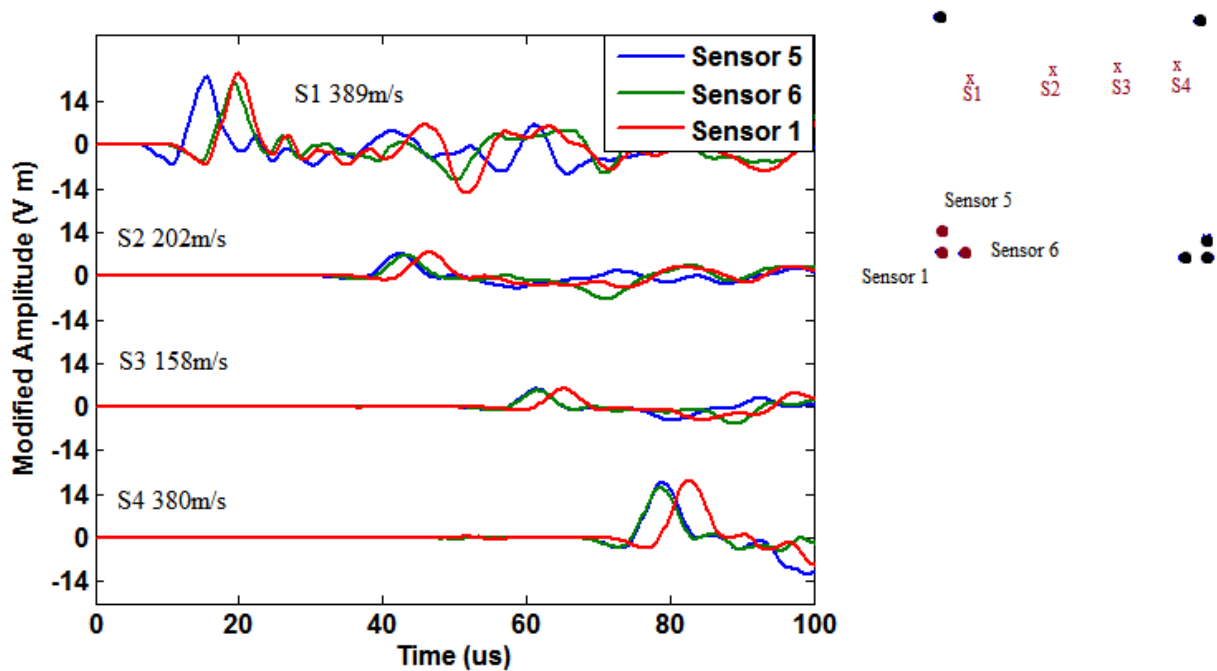
Figure 6.20 Signals measured on group 1 panel SP14 for shots 1 to 4. The signals have been corrected for angle and distance.

In Figure 6.23 the signals shown in Figure 6.21 are further corrected by dividing the magnitudes of the signals by the square root of the energy of each impact; (recall that the signals in Figure 6.22 have already been corrected for angle and distance). For comparison all amplitudes are

divided by the maximum amplitude of sensor 6 subjected to impact S1. It can be seen now that

all the values have the same approximate amplitude.
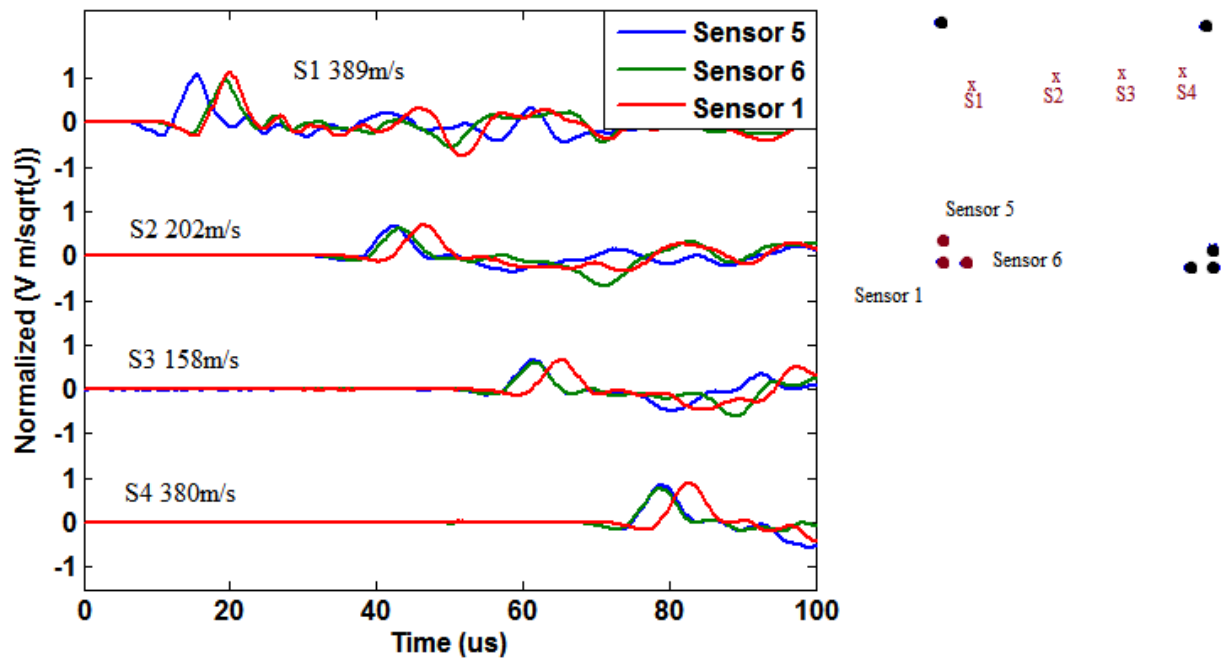
Figure 6.23 Signals of group 1 panel SP14, a correction for distance and angle has been applied and then divided by the square root of the energy absorbed in each impact (since the impact speed is low this is almost identical to the impact energy), the last step is a normalizing using the maximum value of the sensor 6 from impact S1.

Figure 6.24 shows a typical impact wave signal and the envelope of the signal in the same plot.

Three regions can be identified in this plot: (1) the arrival of the first wave of very small

amplitude and is likely the S0 Lamb wave, since it is faster than the A0 wave. The difference in

the time of arrival between the A0 and S0 Lamb waves also approximately corresponds to the

difference in wave speeds between these two waves; (the wave speed of the A0 mode, for this

angle, is approximately 3800m/s as shown on Figure 5-2 ,the 20µs show on Figure 6.24) will

require an approximate speed of 5000m/s that makes sense for a S0 wave on a panel with this

thickness. (2) 30us after the initial wave, the main A0 wave then arrives. (3) Approximately after 30us more another wave of opposite sign arrives at the sensor. This change of sign is characteristic of a reflection from the free boundary and is identified as such in Figure 6.24. The two vertical lines in this plot show the integration window for the damage parameter (DP). It can be seen that the window starts when the envelope reaches a certain small threshold value and stops close to the first minimum of the envelope signal. This is the case for almost all the signals and for all the impacts. The exceptions are for the low speed impacts were this end of the integration window clearly occurs before the first envelop minimum.
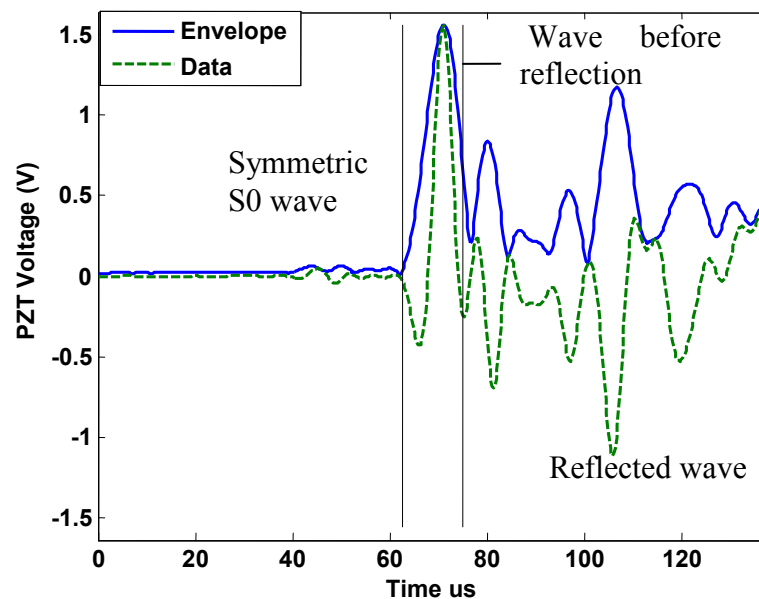
Figure 6.24 Signal measured by Sensor 1 shot 5 for panel SP20. Two Lamb waves can be seen, the symmetric S0 Lamb wave which arrives first, followed by a direct A0 (antisymmetric) wave. These waves are followed by the reflection of the panel boundary of the direct wave.

Once the signal envelope and integration window have been found, calculation of the signal parameter (SP) can be performed for all shots and all sensors. Recall that at this point the assumption of Equation 6.1 as to be validated. The challenge in finding the exponential correction is in isolating the effect of the shot amplitude due to impact velocity and wave propagation amplitude. To be able to eliminate this speed of impact and amplitude ratio effect, two panels (SP22 and SP23) were shot 8 times each at identical relative positions with approximately the same speeds (~320m/s). From the 16 impacts, 10 signals were valid. (Of the three impacts that could not be used for this validation, two impacts were not perpendicular to the plate and one impact failed to reach the required speed of 320m/s). Using this comparable data, the signal parameter (SP) was then calculated and corrected for angle, the $1/\sqrt{r}$ and exponential signal attenuation. There is a significant dispersion on the values of the DP for each shot, this dispersion increases with the impact speed. Since the dispersion grows with impact speed as well as the parameter itself both data could be used to calculate the incoming speed form the sensors measurements. Taking an average of the measurement between all the sensors in a panel produces a good correlation between speed and DP as will be shown on the following subsection.

6.7   Results

Figure 6.25 shows the damage parameter (DP) plotted against impact speed and absorbed energy. The correlation between DP and speed appears to be parabolic which as previously discussed indicated that DP is related to the impact energy. When DP is compared directly with energy though, it can be seen that there is a linear relationship up to penetration. At this point the panels do not absorb more energy but the parameter continues growing. Though not fully understood at this point, this relationship is beneficial from the point of view of structural health

monitoring since it allows one to measure the impact speed for both penetrating and non-penetrating impacts. Once the incident speed has been calculated and if the V50 of the panel has been previously characterized, whether the projectile has penetrated the panel can then be readily determined. From a SHM point of view, it is important to also correlate the DP to the damage area caused by the impact. This relationship can be seen in Figure 6.26 where the damage parameter is compared with the delamination area. As for the relationship between absorbed energy and the DP, there is a correlation between DP and delamination area until penetration but not after penetration. Note that the Damage parameter DP has dimensions of energy.
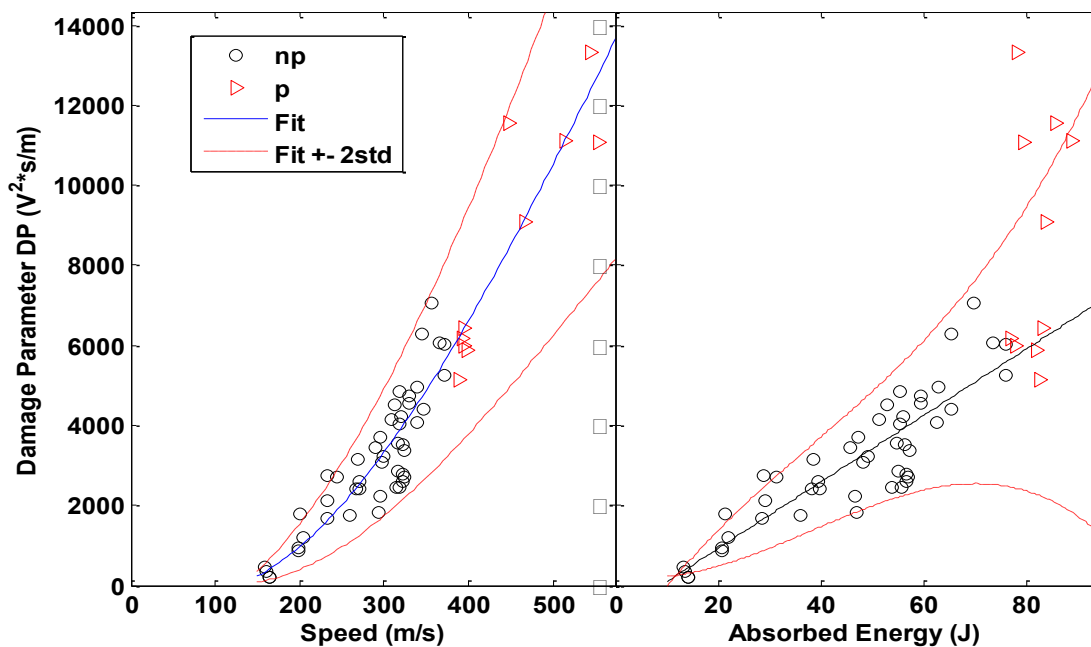
Figure 6.25 Average by shots of proposed parameter measurement compared with the speed and absorbed energy. The solid lines represent a parabolic fit for the speed to DP relationship (left) and a linear fit for the non- penetrating impacts to DP relationship (right). The dashed red represent the uncertainty in the fitted. Here again **np** represent non penetrating impacts, while **p** are penetrating impacts.

As previously discussed, at speeds greater than V50, the delamination area remains constant while the DP continues to increase. In Figure 6.27 DP is compared with the estimated radius of delamination assuming that the delamination area is circular. It is interesting to note that the curve fit of the damage radius to DP relationship predicts the smallest damage area to be approximately 2.5mm which corresponds to the radius of the projectile.
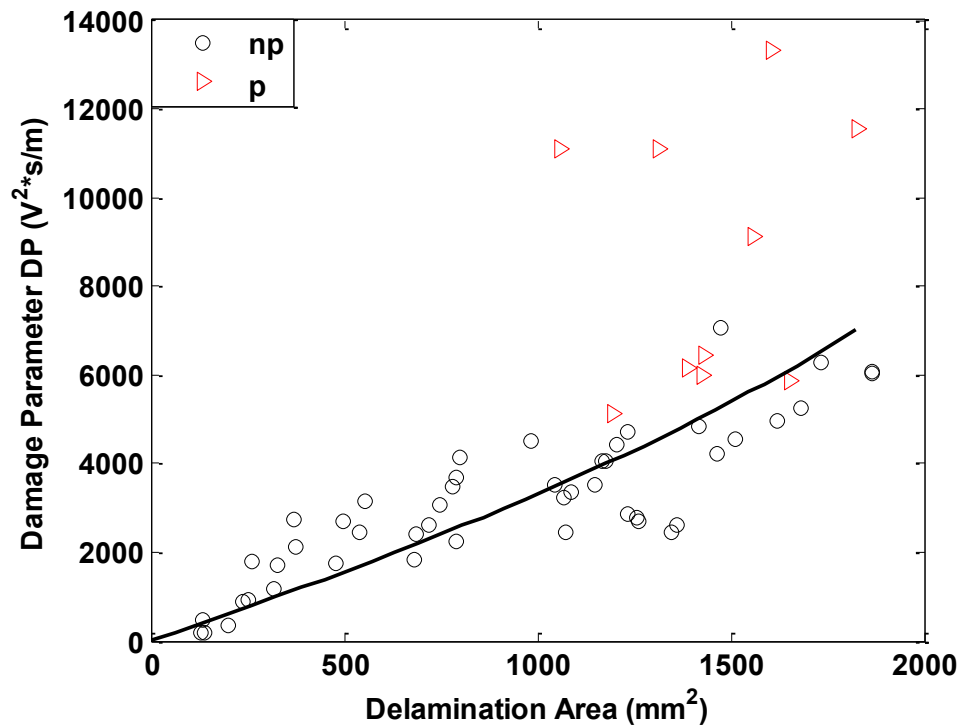
Figure 6.26 Damage Parameter as a function of Delamination area. A 2nd order polynomial fit is shown for the non-penetrating impacts (np).   Here again **np** represent non penetrating impacts, while **p** are penetrating impacts.
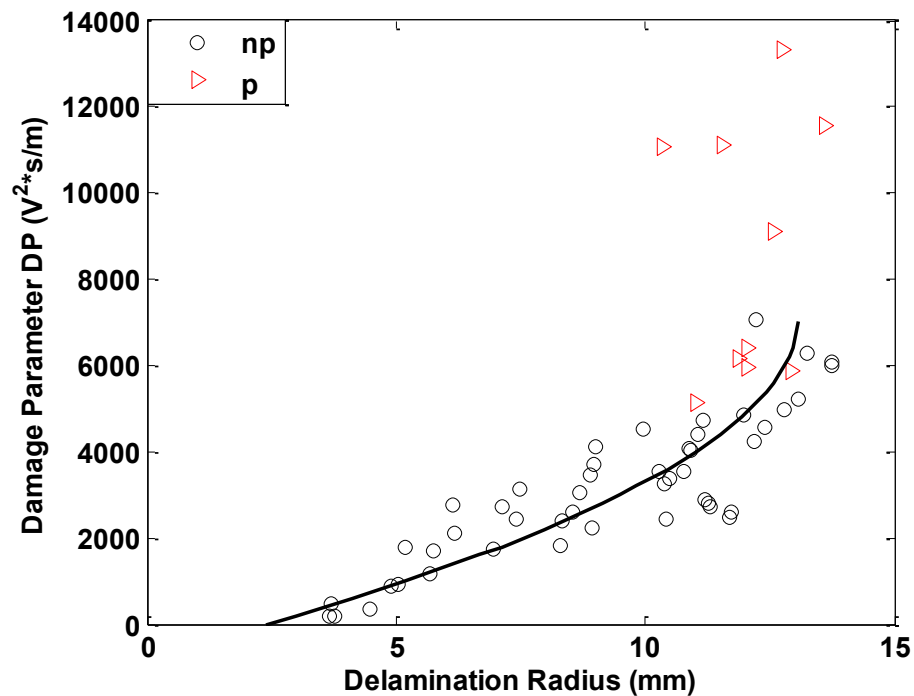
Figure 6.27 Damage Parameter as a function of equivalent delamination radius; **np** represent non- penetrating impacts, while **p** are penetrating impacts.

6.8   Conclusions

The major contribution of this work is the derivation of a new high speed impact damage parameter (DP) that is based on the energy of the first anti-symmetric (A0) Lamb wave as measured by a sensor network. This novel DP parameter can be used to predict the speed of the projectile, the absorbed impact energy and the delamination area caused by the impact for a fiber glass panel over a wide range of impact speeds (160 to 600m/s). One unexpected characteristic of the DP parameter is that it continues to increase with increasing speed even above the V50 of the material even though the delamination areas above this speed remain approximately constant.

The damage parameter also predicts a minimum equivalent damage radius that is approximately the same as the contact radius of the projectile.

Previously, several damage parameters have been proposed to assess the damage level of a structure or component in various systems, including techniques that use passive detection. An example of this is the bearing health monitoring using spectral analysis, for example Farrar (2007). To our knowledge the work presented in this thesis is the first successful use and definition of such a damage parameter for a composite material under high speed impact loads. One important limitation of the present work though is that only one material (fiber-glass epoxy) and one type of projectile (FSP) has been studied. At this point the validity of the novel technique for other material-projectile combinations is unclear and should be investigated further in future studies. In the case under study, projectile is very stiff and suffers not deformation during the impact. For example, the use of more deformable projectiles (or projectiles made from multiple materials) could divert some of the impact energy to material deformation, and therefore a change in the parameter definition might be required.

The proposed DP technique is relatively simple and can be readily implemented in an integrated circuit. After data acquisition, the only calculation that needs to be performed is the integration of the analytic function (Hilbert transform). This relatively easy calculation can be implemented in an ultra-low power analogical circuit or in a relatively simple digital circuit. This is an important conclusion since commercial use of this method would typically have a volume and energy consumption requirement.

Another interesting result of this work is that the relatively simple approximation of the absorption due to the point source propagation and absorption of the material (as proposed by

Equation 6.1) has proven to be an adequate simplification for wave attenuation over the range of distances and frequencies used in this work. As part of this work, an experimental technique was developed to measure the angular absorption of the material.

As part of the present research, an optical technique using digital photography was developed to calculate the delamination area in composite translucent panels and compared with a traditional ultrasonic C-scan technique. The novel optical method has been shown to accurately predict delamination when compared to the C-scan technique but has the advantage of being significantly faster. Unfortunately most of the fiber reinforced materials are not translucent limiting the applicability of this optical method.

7   Accomplishments and future work

A passive structural health monitoring system capable of locating and quantifying damage from high speed impacts has been developed and experimentally demonstrated in this thesis. This includes three major accomplishments: (1) manufacturing of composite panels with embedded sensors, (2) prediction of damage location, and (3) calculation of the extent of damage. These techniques have been developed with real-world applicability in mind. Though potentially less accurate than other proposed damage detection techniques, they have the advantages of easier manufacturability and computational efficiency (and thus a faster response time with less electrical power consumption).

7.1   Achievements

7.1.1   Panel manufacture

A vacuum infusion fiber glass/epoxy panel manufacturing technique has been developed, with the following characteristics:

- Compatible with embedded sensors, including brittle sensors such as PZT
- Allows for precise sensors placement
- Has a high signal to noise ratio
- Is relatively inexpensive to manufacture (compared to other multistep methods)
- Has improved sensors survivability
- Has simplified cable routing
- Is scalable to thick panels (up to 1.5" at the time of writing this document)
- Can be used for active damage detection

These developments make the technique a promising option for future applications. An important drawback is that the sensors manufacture requires skilled personnel.

7.1.2 Passive damage location detection

A novel high speed impact damage location detection technique has been developed as part of this research. The advantages of this new technique are:

- Reduced computational load and thus reduced electrical energy consumption
- Fast computation time
- Grouping of sensors which reduces manufacturing complexity and thus cost
- Compatibility with active techniques
- Ease of integration in analog or digital circuitry
- Relies on measuring high frequency wave propagation which allows filtering of ambient noise

The disadvantage of the technique is that that it appears to be less precise than the traditional triangulation technique. However, it is believed that the precision demonstrated in this research (< 30 mm error in impact location) is adequate for most real-world applications.

7.1.3 Passive detection of damage extent

A robust technique has been developed that allows for the estimation of impact speed, absorbed energy and delamination damage energy for high speed impacts. To the knowledge of the author this is the first such technique for high-speed impacts. Some of the technique highlights include:

- Uses the same group of sensors as for impact position detection
- Allows estimation of impact speed, absorbed energy and damage area
- Use groups of sensors with all the same manufacturing advantages as listed for impact position detection above
- Uses a relatively simple algorithm and has similar advantages in computational speed and low electrical power as for the novel impact location method above
- Compatible with active detection techniques

- Uses only high frequency signals arising from the impact event thus allowing for the filtering of ambient noise

The main drawback of this technique is that it has only been studied for one combination of projectile (i.e. fragmentation simulating) and one composite material (fiber glass – epoxy).

7.2   Future work

There are some aspects of this research that would benefit of further research; these include: deeper understanding of the mechanics of inelastic impact wave propagation and generation, (2) the effects of different combinations of projectiles and target materials and geometries, and (3) the effects on mechanical properties (such as strength and stiffness) of embedding sensors into composite panels.

It is believed that a better understanding of the mechanics of wave propagation caused by high speeds impact would greatly enhance the developed techniques in this thesis. The physics of the wave propagation during damage inducing impact is not well understood at this time. A deeper understanding of the underlying wave propagation physics could hopefully explain several phenomena observed in the present research such as the quadratic dependence wave absorption on propagation angle, and the selection of the appropriate integration time for calculating the novel damage parameter.

Another important extension of the present work would be to extend both detection techniques (i.e. impact location and damage extent) to various projectile materials and geometries and to various composite materials. This step is critical for any future commercial use.

The effect of the sensor embedding on panel performance such as strength and stiffness has to also be addressed in the future. This includes investigating the size and thickness of the sensors,

as well as the position of the sensor/s within the composite panel. These studies are needed both from a manufacturability standpoint and under testing from various mechanical loading. The dependence of sensor size is also critical in determining sensor survivability.

Further development in the sensor embedding technique can make it not only less expensive but also extend their applications to structures with more than one material (such as composite ceramic, composite steel, or multi fiber composite).

8   Bibliography

Betz, D. C. et al. 2007. "Structural Damage Location with Fiber Bragg Grating Rosettes and Lamb Waves," Structural Health Monitoring, 6. doi:10.1177/1475921707081974

Birt, R., Babcock, A., and A, E. (2000). "The use of 0-3 piezocomposite embedded Lamb wave sensors for detection of damage in advanced fibre composites". Smart Mater. Struct. , 9, 291–297.

Ciampa, F. and Meo, M. 2011. "Impact Detection in Anisotropic Materials Using a Time Reversal Approach," Structural Health Monitoring, 11(43). doi:10.1177/-1475921710395815

Ciampa F., Meo M., 2010."A new algorithm for acoustic emission localization and flexural group velocity determination in anisotropic structures", Composites Part A 41, 1777–1786.

Ciampa, F., Meo, M. and Barbieri, E. 2012. "Impact Localization in Composite Structures of Arbitrary Cross Section." Structural Health Monitoring, 11. doi:10.1177/-1475921712451951

Chang, C. and Sun, C. T.,1989 "Determining transverse impact on a composite laminate by signal deconvolution". Experimental Mechanics, 1989, 29, 414

Coleman, S. M. 1998. "Monotonic and fatigue loading behavior of quasi-isotropic graphite/epoxy laminate embedded with piezoelectric sensor". Smart Material and Structures. 7, 822–832.

Coverley, P. T. and Staszewski, J. W. 2003. "Impact Damage Location in Composite Structures Using Optimized Sensor Triangulation Procedure," Smart Materials and Structures, 12, 795–803.

De Marchi, L. et al. 2011. "A Passive Monitoring Technique Based on Dispersion Compensation to Locate Impacts in Plate Like Structures," Smart Materials and Structures, 20. doi:10.1088/0964-1726/20/3/035021

Dehghan Niri, E. and Salomone, S. 2012. "A Probabilistic Framework for Acoustic Emission Source Localization in Plate-Like Structures," Smart materials and structures, 21. doi:10.1088/0964-1726/21/3/035009

Farrar C. R. and Worden K. 2007 ,"An introduction to structural health monitoring". Phil. Trans. R. Soc. A (2007) 365, 303–315 doi:10.1098/rsta.2006.1928

Feldman M. 2011 "Hilbert Transform Applications in Mechanical Vibration" John Wiley & Sons, Ltd. ISBN: 978-0-470-97827-6

Ghezzo, F., Huangz, Y., & Nemat-Nasser, S. 2009. "Onset of Resin Micro-Cracks in Unidirectional Glass Fiber Laminates with Integrated SHM Sensors: Experimental Results". Structural Health Monitoring , 8, 477-491.

Giurgiutiu, V. 2002. "Lamb Wave Generation with Piezoelectric Wafer Active Sensors for Structural Health Monitoring". SPIE's 10th Annual International Symposium on Smart Structures and Materials and 8th Annual International.

Gover H.L. , Cronin D.S, Plumtree A. 2008 "High speed impact response of laminated composite panels" International Journal of Impact Engineering 35 (2008) 1000–1008

Graff, K. 1975. "Wave Motion In Elastic Solids," New York: Dover Publications, INC.

Hansen J. P. and Vizzini .A J. 1997 "Fatigue response of a host structure with interlaced embedded devices". 38th AIAA/ASME/ASCE/AHS/ASC Structures, Structural Dynamics and Materials Conf. AIAA-97-1346 (AIAA)

Mavivand M., Liaghat G.H. 2010 "A model for high speed impact on multi-layer fabric targets". Int J impact Eng 2010:37 806-812.

Maznev A.A. Lomonosov A. M., Hess P. and Kolomenskii A.A. 2003 "Anisotropic effects in surface acoustic wave propagation from a point source in a crystal" Eur. Phys. J. B **35**, 429–439 (2003) DOI: 10.1140/epjb/e2003-00295-y

Morrison C. 1984 "The mechanical response of an aramid textile yarn to high speed impact". Ph.D. Thesis, University of Surrey 1984.

Morye, S. S. et al 2000. "Modeling of the energy absorption by polymer composites upon high speed impact" Composites Sciences and Technology 60, 2631-2642 doi: 10.1016/S0266-3538(00)00139-1

Moulin, E., Assad, J., Delebarre, C., Kaczmarek, H., and Balageas, D. 1997. "Piezoelectric transducer embedded in a composite plate: Application to Lamb wave generation". Journal of Apllied Physics , 82, 2049-2055.

Naik N.K., Shrirao 2004 P. "Composite structures under high speed impact", Composite Structures 66 (2004) 579–590

Lamb, H. 1917 "On Waves in an Elastic Plate", Proceeding of the Royal Society of London, series A, doi: 10.1098/rspa.1917.0008

Lanza di Scalea, F. et al. 2011. "Location and Indentification of Impact Forces in Composite Aeroespace Panels," AIAS – Associazione Italiana per L'Analisi delle Sollecitazioni 40 Convegno Nationale.

LeClerc, J. et al. 2007. "Impact Detection in an Aircraft Composite Panel—A Neural-Network Approach," Journal of Sound and Vibration, 299, 672-682.

Lin, M. and Chang, F.-K. 2002. "The Manufacture of Composite Structures with a Built-in Network of Piezoceramics," Composites Science and Technology, 62, 919–939.

Kundu T., Nakatani H., Takeda N., 2012 "Acoustic source localization in anisotropic plates", Ultrasonics 52, 740-746.

Parga-Landa B, Hernandez-Olivares F. 1995 "Analytical model to predict behaviour ofsoft armors". Int J Impact Eng 1995;16:455–66.

Parga-Landa B.,Vlegels S., Hernandez-Olivares F. Clark S. D.1999 "Analytical simulation of stress wave propagation in composite materials". Composite Structures 45 (1999) 125±129

Prevorsek DC, Chin HB, Kwon YD. 1991 "Strain rate effects in ultrasonic polyethylene fibers and composites". Journal of Applied Polymers Science, Applied Polymers Symposium 1991;47:45–66.

Propst A, Peters K, Zikry M A. el all. Assessment of damage in composite laminates through dynamic, full-spectral interrogation of fiber Bragg grating sensors. Smart materials and Structures 19

Roylance D. 1973 "Wave propagation in a viscoelastic fiber subjected to transverse impact". ASME J Appl Mech 1973;40:143–8.

Saponara, V. L., Horsley, D. A. and Lestari, W. 2011. "Structural Health Monitoring of Glass/Epoxy Composite Plates Using PZT and PMN-PT Transducers," Journal of Engineering Materials and Technology, 133.

Salamone, S. et al. 2010. "High-Velocity Impact Location on Aircraft Panels Using Macro-fiber Composite Piezoelectric Rosettes," Journal of Intelligent Material Systems and Structures, 21. doi:10.1177/1045389X10368450

Schäfer, F. and Janovsky, R. 2007. "Impact Sensor Network for Detection of Hypervelocity Impacts on Spacecraft," Acta Astronautica 61, 901 – 911.

Sha, F.T.J. "Structural health monitoring of M1114 high mobility multipurpose wheeled vehicle armor system" AFIT/GEM/ENV/12-M19

Soh, V., Annamdas, G. M., & Kiong, C. 2007. "Three-Dimensional Electromechanical Impedance Model.II: Damage Analysis and PZT Characterization". (ASCE, Ed.) Journal of Aerospace Engineering , 63-71.

Staszewski, W. 2002. "Intelligent Signal Processing for Damage Detection in Composite Materials," Composites Science and Technology, 62, 941–950.

Su, Z., Ye, L., & Lu, Y. 2006. "Guided Lamb waves for identification of damage in composite structures: A review". Journal of Sound and Vibration 295 , 753–780.

Sung-ChoongWoo, & Goo, N. S. 2009. "The relationship between electromechanical cyclic loading and the performance degradation of a smart bending piezoelectric actuator". Smart Mater. Struct. , 18, 1-10.

Stotler C.L. 1981 "Development of advanced lightweight systems containment final report". Nasa CR-165212 R81AEG208

Taylor G.I. 1942 "The plastic wave in a wire extended by an impact load".. Mechanics of solids 1942. Paper 32. In: Batchelor GK, editor. The scientific papers of Sir G I. Taylor, vol. 1. Cambridge: Cambridge University Press; 1956.

Torres-Arredondo, M. A., Jung, H., & FRITZEN, C. P. 2011. "A Study of Attenuation and Acoustic Energy Anisotropy of Lamb Waves in Multilayered Anisotropic Media for NDT and SHM applications". In Proceedings of the 6th International Workshop NDT in Progress, Prague, Czech Republic.

Tressler J.F, Alkoy S., Dogan A., Newnham R.E.1999 "Functional composites for sensors, actuators and transducers" Composites: Part A 30 (1999) 477–482

Van der Velden C., Bil .C, Yu X. Smith A., 2007 "An inteligent system for automatic layout routing in aerospace desing". Innovations Syst Softw Eng (2007) 3:117–128, DOI 10.1007/s11334-007-0021-4

Vinson J.R, Zukas J.A.1975 "On the high speed impact of textile armor". ASME J Appl Mech 1975;42:263–8.

Wu T. T. and Chiu S. T. 1992 "On the propagation of horizontally polarized shear waves in a thin composite laminate plate". Ultrasonics 30 1, 60-64

Yan, G. and Zhou, L. 2009. "Impact Load Identification of Composite Structure Using Genetic Algothithms," Journal of Sound And Vibration, 319, 869-884. doi:10.1016/ j.jsv.2008.06.051

Yang, S.H. and Sun, C.T.,1981 "Indentation Law for Composite Laminates", NASA CR-165460, July 1981

Zhao, X., Gao, H. and Zhang, G. 2007. "Active Health Monitoring of an Aircraft Wing with Embedded Piezoelectric Sensor/Actuator Network: I. Defect Detection, Localization and Growth Monitoring," Smart Materiald and Structures, 16, 1208–1217. doi:10.1088/0964-1726/16/4/032

APPENDIX. A. List of materials for vacuum infusion multifunctional panel manufacture

The table bellow gives a complete list of the material needed for the vacuum infusion, when appropriate specific model and supplier is given. Common equipment as not been specified, since several brands and model has been used though this study.

Product	Reference	Supplier
PZT sensors	1/4" diameter by 0.0075" thickness PZT-5A	PIEZO
Wire	130-AWN Gauge 30 (0.254mm)	Vishay
Soldering Flux	#67 Liquid flux	PIEZO
Soldering Iron+solder		
5 min epoxy		
Fiber	S2-6187	HEXCEL
Epoxy resin	EPON 828	Momentive
Curing agent	EPICURE 3230	Momentive
Vacuum bag	SL800	Airtech
Flow media	GREENFLOW	Airtech
Peel of Ply	Release Ease 234 TFP	Airtech
Breather	Airwave A	Airtech
Sealant	AT200Y	Airtech
Masking tape		
Resin trap.	RB 451	Airtech
Vacuum pump		
Tubing		
Razor blades.		
Kevlar cutting scissors.		
Scissors.		

APPENDIX B List of Publications

Zamorano-Senderos B, Elvin N. 2013 "High-speed impact location detection on anisotropic composite panels using embedded piezoelectric sensors". Journal of Intelligent Material Systems and Structures. **doi:10.1177/1045389X13512188**

On preparation:

Zamorano-Senderos B, Elvin N. "High-speed impact damage stent detection on anisotropic composite panels using embedded piezoelectric sensors". Journal of Inteligent Material Systems and Structures.

UNCLASSIFIED